Department of Chemical and
Environmental Engineering

ENHANCED RECOVERY OF HEAVY OIL USING A CATALYTIC PROCESS

by

Muayad Mohammed Hasan

BSc., MSc.

Thesis submitted to the University of Nottingham for the degree of Doctor of Philosophy

May 2018

ABSTRACT

Oil is a major source of energy around the world. With the decline of light conventional oil, more attention is being paid to heavy oil and bitumen, as a good alternative to light oil for energy supplies. Heavy crude oils have a tendency to have a higher concentration of metals and several other elements such as sulfur and nitrogen, and extraction of these heavy oils requires more effort and cost. The Toe-to-heel Air Injection catalytic upgrading process In-situ (THAI-CAPRI) is an integrated process which includes recovery and upgrading of heavy oil and bitumen using an air injection process, and horizontal injector and producer wells. Since the process works through a short distance displacement technique, the produced oil flows easily toward the horizontal producer well. This direct mobilized oil production and short distance are the major properties of this method which lead to robust operational stability and high oil recovery. This technique gives the possibility of a higher recovery percentage and lowers environmental effects compared to other technologies like steam based techniques. A catalyst plays a crucial role in the THAI-CAPRI technique to be successfully conducted. However, heavy coke can be formed as a result of the thermal cracking of heavy oil occurring in the THAI-CAPRI process, and a catalyst resistant enough to use in CAPRI needs to be developed. Therefore, there is a need to understand the pore structure to achieve a high catalyst quality, to obtain a structure that directly affects the fluid behaviour within a disordered porous material.

In this study, novel experimental techniques were used to obtain greater accuracy results, for the information obtained from gas adsorption curves by using a combination of data obtained for two adsorptives, namely nitrogen and argon, both before and after mercury porosimetry. This new method allows studying the effect of pore-pore co-operative during an adsorption process, which significantly affects the accuracy of the pore size distributions, obtained for porous solids. A comparison, between the results obtained from the characterisation of a mixed silica-alumina pellet and those obtained from pure silica and alumina catalysts, were presented to study the effects of surface chemistry on the different wetting properties of adsorbates. The pore networks within pellets invaded by mercury following mercury porosimetry have been imaged by computerized X-ray tomography (CXT). It was noticed that the silica-alumina catalyst had a hierarchical internal structure, similar to that for blood vessels in the body. To validate the findings of the pore geometry characterisation obtained from the new method, several techniques, such as cryoporometry, gas sorption isotherms, and mercury intrusion experiments, were considered.

Further, a novel well design consisting of two horizontal injectors and two horizontal producers was used in different well configurations, to investigate the potential for improved efficiency of the THAI process on the heavy oil recovery. A 3D dimensional simulation model, employing the CMG-STARS simulator, was applied in this simulation. Two horizontal injectors and producers were designed in this project, instead of horizontal injector and producer were used in the Greaves model (the base case model), to investigate the effect of the extra injector and producer on the performance of the THAI process. It was found that the locations of the well injections and the well productions significantly affected the oil production.

For the study of the effectiveness of the catalysts in the oil upgrading process, the CAPRI technique has been simulated to investigate the effect of several parameters, such as catalyst packing porosity, the thickness of the catalyst layer and hydrogen to air ratio, on the performance of the CAPRI process. The TC3 model used by Rabiu

Ado (2017), which was the same model used in the experimental study of Greaves et al. (2012), was also used in this study. The Houdry catalyst characterised by the experimental work was placed around the horizontal producer in this simulation.

LIST OF PUBLICATIONS

Rigby, S.P., **Hasan**, M., Hitchcock, I. and Fletcher, R.S., 2017. Detection of the delayed condensation effect and determination of its impact on the accuracy of gas adsorption pore size distributions. *Colloids and Surfaces A: Physicochemical and Engineering Aspects*, *517*, pp.33-44.

Rigby, S.P., **Hasan**, M., Stevens, L., Williams, H.E. and Fletcher, R.S., 2017. Determination of pore network accessibility in hierarchical porous solids. *Industrial & Engineering Chemistry Research*, *56*(50), pp.14822-14831.

ACKNOWLEDGEMENTS

First and foremost, most importantly, I thank God Almighty for giving me the patience, strength and knowledge, and because of his blessing which has made this humble work of research possible.

My sincere gratitude is going to Iraqi cultural attache in London, Petroleum Technology Department, University of Technology and the Ministry of Higher Education and Scientific Research of Iraq to offer me this scholarship opportunity to complete my PhD degree in chemical engineering, and for all their financial support.

I appreciate my deep sense of great gratitude with sincere thanks to my supervisor, Professor Sean Rigby, for his motivation, guidance, advice, and consistent support throughout my degree program. Although, his busy work load, he always helps me answers my enquiries to make this project successful. I owe him so much for all the support and for what I have learnt. It's been a great honour and a privilege working under his supervision, I wish also to thank my co-supervisor, Dr Buddhika Hewakandamby, for his support, guidance, and advice during my PhD period.

I would like to especially acknowledge Dr Huw Williams and Dr Lee Stevens for their help in running NMR and gas adsorption experiments respectively. I am highly thankful to Dr Martin Corfield for performing the CXT imaging. My appreciation also extends to my colleagues, Dr Muhammad Rabiu Ado and Dr Paul Egwuonwu DIM for their help. I gratefully thank the technicians at the Wolfson Building, particularly Tom Buss, Jason Greaves, Max Mason, and the Chemical Engineering Department for their efforts, support and advice. It is my pleasure to thank Johnson Matthey Company to conduct the integrated sorption with mercury porosimetry experiments and provide me with all the data. I would genuinely like to thank the administrations of the faculty of Engineering and the Department of the Chemical and Environmental Engineering for all help and facilities provided to me to achieve my goal.

Finally, I would like to dedicate this effort to the soul of my father, God rest his soul in peace. My special gratitude goes to my mother for her continual prayers to make this expedition possible for me, which I could not have achieved without her. I am very grateful to my wonderful wife to support me and stand by me through all my entire life. Along with her, I would like to extend my warmest thanks to my sons.

TABLE OF CONTENTS

LIST OF FIGURES

LIST OF TABLES

NOMENCLATURE

Acronym	**Meaning**
3D	Three Dimensional
API	American Petroleum Institute
BET	Brunauer Emmet Teller
CAPRI	Catalytic Upgrading Process In-Situ
CP	Centipoise
CSI	Cyclic Steam Injection
CXT	Computerized X-ray Tomography
DSC	Differential Scanning Calorimetry
EOR	Enhanced Oil Recovery
HDN	Hydrodenitrogenation
HDS	Hydrodesulfurization
HI	Horizontal Injector
HP	Horizontal Producer
ISC	In-Situ Combustion
IUPAC	International Union of Pure and Applied Chemistry
MF-DFT	Mean-Field Density Functional Theory
MIP	Mercury Intrusion Porosimetry

NLDFT	Non-Local Density Functional Theory
NMR	Nuclear Magnetic Resonance
PSD	Pore Size Distribution
SAGD	Steam Assisted Gravity Drainage
SG	Steam Gasification
THAI	Toe-to-Heel Air Injection
WGS	Water-Gas Shift

CHAPTER 1

INTRODUCTION

1.1 Introduction

Crude oil is considered a vital part of the range of products which humans need in their daily life. In addition, crude oil is an essential resource for many countries, as well as the economy of those countries based on oil (Sivasankar and Kumar, 2014). Hence, oil remains a major source of the energy for the world. However, wide employment of oil has led to a decline in the reserves of light oil in the world. Thus, the need arises to look for economical methods to extract unused heavy oil which exists in huge amounts in many countries (Hart et al., 2013).

Heavy oil is a plentiful, and considered a widespread, alternative to conventional oil, with considerable reserves in a lot of countries like Canada and Venezuela. Most of the oil in the world is heavy oil and bitumen and which represents about nine to thirteen trillion barrels of the total oil resource as shown in Figure 1-1. One benefit is that this resource is already available and there is no requirement to discover it.

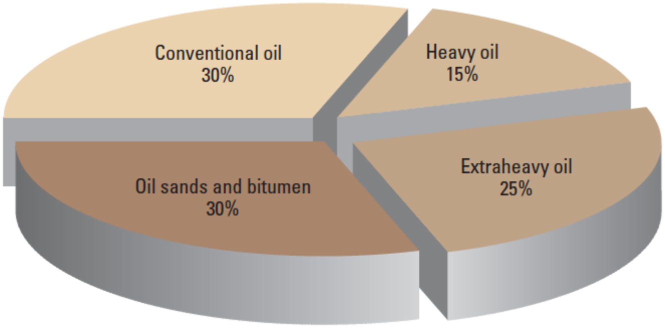

Figure 1-1: The total reserves of the World Oil (Felix et al., 2006).

These kinds of oil have a high content of asphaltenes and chemical elements like sodium, nitrogen, and others in addition to the higher viscosity and density. Therefore, it is quite essential to find convenient technical processes to improve their properties and increase production (Xia et al., 2002).

The American Petroleum Institute (API) (Bjørnseth, 2013) has characterized heavy oil as having low API, as a measure of the density of crude oil relative to water, which is between 10 and 20°. Oils that are immobile in the reservoir under normal conditions with less than API of 10° are classified as extra heavy oil or bitumen. Figure 1-2 displays a schematic clarification of this definition.

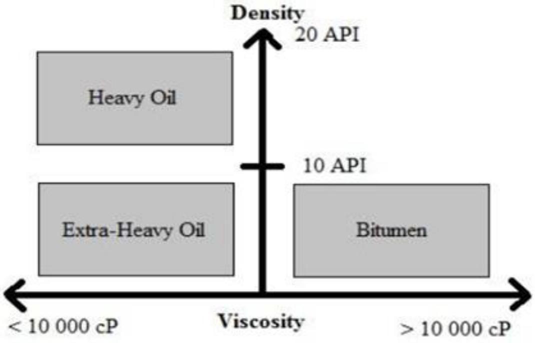

Figure 1-2: Schematic of the heavy oil classification (Bjørnseth, 2013).

Economically, the main factors that determine feasibility during heavy oil reservoir evaluation are density and viscosity. In general, light oil is bought at a higher price than heavier hydrocarbons because the latter needs first to go through promotion processes intensively to be ready for use. Furthermore, enhanced oil recovery (EOR) processes will have a high cost for enhancing and increasing the production of heavy oil because of its high density (Tzimas et al., 2005, Bjørnseth, 2013).

EOR techniques include many types of processes in which oil production will be increased dramatically compared to the amount of oil produced through classical methods. In the normal techniques of oil production, recovery can reach up to 35 to 45 % of the total amount of oil in the reservoir, whereas using of EOR techniques the produced oil may be increased by 5 to 15 percentage points. In the past, many different kinds EOR techniques have been tested to recover heavy and light hydrocarbons, as well as bitumen, but with many field attempts. Figure 1-3 illustrates a comprehensive categorization of these techniques. Thermal methods are the most method used in the process of enhancing oil extraction for heavy oils because other techniques have failed, particularly when they are employed in high-density crude oil (Aristizábal and Vargas, 2005).

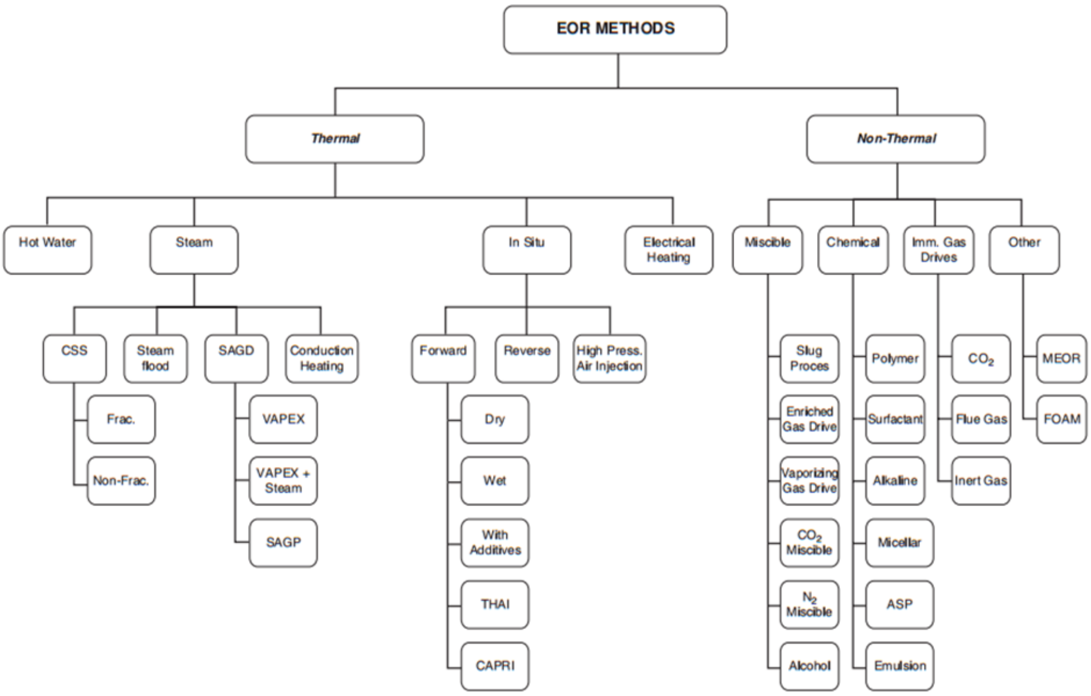

Figure 1-3: Classification of enhanced oil recovery (EOR) methods (Thomas, 2008).

Even though thermal methods are most appropriate for heavy oil and bitumen, they can also be used for light oil in particular cases. Normally, light oils could be extracted by non-thermal techniques. Heavy oils have been recovered by using many of these techniques, nevertheless, have not got a wide success in the recovery of the original oil in place (Greaves et al., 2005, Thomas, 2008). The thermal processes have included several examples of injection techniques in which steam can be injected into the reservoir in two ways. In one of them, steam is injected first, and the production of oil will then follow from the well itself; this is called cyclic steam injection (CSI). Second, steam is injected continuously via an injector well and oil will be produced by the producer well. Another technique, steam assisted gravity drainage (SAGD) in which an injector well is designed horizontally to be on top of the producer well, and heated water can be injected into the well. Another method uses air or oxygen for injection for In-situ combustion processes. Oxygen plays a significant role in this process where it will cause the oxidation of some of the oil in place. This oxidation process leads to a release of heat which in turn results in reduced viscosity of the oil remaining; oil with high molecular mass will be converted to small molecular weight and the heat generated can evaporate some of the hydrocarbons to help the immobile oil to move toward the producer (Alvarado and Manrique, 2010).

In-situ combustion processes, which have been applied to enhanced heavy oil recovery, have been used extensively for several decades. Although this method has gained wide fame at the time for the oil recovery processes, it also has many failed applications. In general, this process is difficult to control (Greaves et al., 2012). Therefore, toe-to-heel air injection (THAI) has been suggested as an alternative to the conventional ISC method (Alvarado and Manrique, 2010). Subsequently, this process has been developed further using a catalyst to upgrade heavy oil in addition to increasing the rate of oil production. Catalytic Process In-situ (CAPRI), which developed from the THAI process, is considered an excellent technique for upgrading, as well as to increase extraction of oil. In the catalytic process, the producer is horizontal and an annular ring catalyst has been placed around this producer. More upgrading reactions will happen on the surface of the catalyst when the heavy oil is flowing through this catalyst bed (Xia et al., 2002, Dim, 2015).

The catalyst plays a significant role in the THAI-CAPRI process for upgrading heavy oil and bitumen but, in addition, also decreases the contaminants, such as sulfur and nitrogen, present in the crude oil (Weissman and Kessler, 1996). Weissman and Kessler (1996) have used several different catalysts in their study, and, it was found that all the types of catalysts used caused an extensive removal of asphaltene, as well as sulfur, nitrogen and vanadium, compared to oil processed without any catalyst. An experimental study has been conducted by Shah et al. (2011) on upgrading heavy oil and bitumen, and, the results detected that a balance between catalyst lifetime and oil upgrading performance has to be taken into account. It was suggested that any catalyst used in the CAPRI technique in the field should be able to work effectively in the range from tens of hours to many days. However, coke deposition occurring during the process will minimize the availability of the catalyst active site. Therefore, coke deposition causes a major problem in plugging macro and micropores scales, and, thus with time these pores become deactivated. For this reason, improving catalyst geometry properties has to be taken into consideration when the catalyst is designed because the asphaltenes present in the oil have such a high molecular weight (Ancheyta et al., 2005).

In order to avoid such problems of coke formation, characterisation of catalysts needs to understand the behaviour of fluids within pores to determine desirable physical properties that can give good resistance to coking, as well as design more stable catalysts. Therefore, in this study, new methods have been employed to look at hierarchical structures that are used as the catalyst to increase cocking resistance. The designed catalyst has a porous network by nesting porosity of different sizes to improve the physical properties of the catalyst. Such internal structure can create wider surface areas to provide higher resistance to deactivation. Further, the interior big size of the transport pores would assist fluids in reaching the small pores with a high surface area to provide more effective catalytic reaction. Additionally, for heavy oil and bitumen, pore volume and pore size distribution (PSD) of catalyst are the main keys in determining the catalyst activity (Gopinathan, 2012). Therefore, a high accuracy of the PSD determination is required. The presence of certain effects, such as advanced condensation (Hitchcock et al., 2014b) and delayed filling (Esparza et al., 2004), can reduce this accuracy. Thus, these phenomena need to be taken into account in this work. Any pore within the disordered material in contact with a vapour phase can be filled with condensate. Once the externally applied pressure is increased, a phase transition of vapour-liquid occurs, and the void space is filled with capillary condensate. Where this pore is interconnected to its adjacent pores by pore necks, the filling of the pore body by condensate will be delayed to a vapour pressure higher than the pressure required to fill non-interconnected pore. This phenomenon is called delayed condensation. In contrast, an empty body, connected to a neighbouring neck that is being invaded by liquid, can be filled with condensate at a vapour pressure lower than the pressure needed for the isolated pore to be filled with condensate. This is called the advanced condensation. In order to detect these effects on PSD accuracy, the size of the pore will also be determined independently using differential scanning calorimetry (DSC) and NMR cryoporometry experiments.

Furthermore, reservoir rock systems are extremely complex because of heterogeneous and dissimilar rock properties, different types of fluids and the characteristics of the relative permeability. All these reasons make the prediction of fluid behaviour inside the reservoir during production difficult. Therefore, reservoir simulation is considered a suitable method to find out how the liquid behaves in the reservoir. A 3D numerical simulation of THAI has been carried out in this project to investigate the effect of different well configurations on the performance of the THAI technique, to find the best design for increasing the heavy oil production. Two horizontal injectors and two horizontal producers (2HI2HP) in different well configurations have been employed in this simulation. In each well configuration, the injectors and the producers have been put in different locations. Therefore the different designs of the injectors and the producers' positions are very important in this work.

In addition, heavy oil produced by different methods needs to be transformed to refineries to be processed and refined into beneficial products. Instead, the THAI-CAPRI technique can offer this facility to upgrade heavy oil in-situ, providing high quality and environmentally petroleum products. Therefore, one of the aims of this study **is** to carry out a simulation of the THAI-CAPRI process to demonstrate the effect of the presence catalyst on the produced oil. In the CAPRI process, the Houdry catalyst used in the experimental section has been employed in the simulation. Several important parameters, such as catalyst packing porosity, catalyst thickness and hydrogen to air ratio, have been tested to detect the effect of these parameters on the performance of the CAPRI method.

1.2 Aims and Objectives

The aims of the study are to further understanding and determine the performance of enhanced oil recovery through characterisation of disordered porous materials, using different experimental methods, and a simulation approach. The CAPRI upgrading process eliminates the difficulties which take place during the process of production and heavy oil transportation (Shah, 2011). Therefore, the aim of this study is to develop techniques to design a catalyst resistant enough to coking to use in CAPRI. Another aim is to improve and find the best conditions for the higher heavy oil recovery using THAI-CAPRI process, as well as applying the catalyst characterised by different methods to study the effect of several parameters, such as catalyst thickness, hydrogen to the air ration and catalyst packing porosity, on the technique performance. These aims can be achieved by the following objectives:

- To assess the impact of the delayed condensation effect on the prediction of vapour condensation pressure and pore size derivation.
- To determine pore sizes of model materials using a range of alternative techniques such as mercury porosimetry, mercury DSC thermoporometry and NMR cryoporometry.
- To compare pore size from other techniques with that obtained from gas adsorption using standard data analysis methods such as Cohan equation and NLDFT.
- To determine whether the discrepancy between gas sorption and other methods is due to delayed condensation using specially integrated mercury experiments with nitrogen and argon adsorption.
- To investigate new well configurations for THAI process to consider potential improvements on conventional approach.
- To simulate THAI-CAPRI process using ‘Houdry’ catalyst which is characterised by the experimental work.

1.3 Thesis Structure

Highlights

One of the most important discoveries in the thesis is a measurement of the size of the delayed condensation effect which arises in the gas adsorption experiment. It has been found that pore size distributions from adsorption isotherms are likely to be skewed towards bigger pores because of this delayed condensation effect. Another significant discovery was the difference in the wetting of solid mercury surfaces, relative to silica, for different adsorbates (namely nitrogen and argon). In addition, the 'Houdry' catalyst, characterised by various techniques, was employed in the simulation model to evaluate its effect on the performance of the THAI-CAPRI process to enhance heavy oil recovery.

Chapter One: Introduction

The first chapter will include the introduction of the thesis, a summarized description of crude oil, enhanced heavy oil recovery and characterisation of catalysts, and the gap that needs to be covered by this research. This chapter will also contain the aims and objectives as well as the thesis structure.

Chapter Two: Literature review

The second chapter represents literature review in which a comprehensive description of the heavy oil, oil reservoir rocks, oil recovery and its methods have been described. It is also included previous work conducted by various researchers.

Chapter Three: Characterisation of Porous Media

This chapter will provide comprehensive details of different methods that have been used to characterise pore properties for disordered materials with discussion of the theory of each technique. The methods used in this study were gas sorption (ASAP), mercury porosimetry (MIP), differential scanning calorimetry (DSC), computerised x-ray tomography (CXT) and NMR cryopoprometry.

Chapter Four: Characterisation Results of Silica Catalyst

The fourth chapter will show and discuss the significant experimental results obtained from the characterisation of a silica catalyst using different techniques such as gas sorption, mercury porosimetry, integrated gas sorption and mercury porosimetry, DSC and NMR cryoporometry. The Washburn equation and Kloubek correlations will also be used to study and understand the hysteresis phenomena that arise in mercury porosimetry.

Chapter Five: Characterisation Results of Silica-Alumina Catalyst

The fifth chapter will present and discusses the results of the characterisation techniques, which used in this research, on the silica-alumina catalyst using different techniques. These techniques were Computerised X-ray tomography (CXT), mercury porosimetry, integrated gas sorption and mercury porosimetry DSC and NMR cryoporometry.

Chapter Six: Characterisation Results of Alumina pellet

This chapter describes studies of the internal structure of the alumina pellet catalyst, using CXT image before and after mercury intrusion-extrusion porosimetry.

Chapter Seven: Simulation Results of the THAI Process

The seventh chapter shows the results of the THAI simulation process. Also, this chapter displays an effect of several parameters on the THAI technique performance.

Chapter Eight: Conclusion and Recommendations

This chapter concludes the findings obtained from the research as well as includes some suggestions on what future work could be done to acquire a deeper understanding of the oil transport in the porous media within disordered materials. It will also look at potential further developments in the THAI process and the CAPRI process in which catalyst is employed.

CHAPTER 2

LITERATURE REVIEW

2.1 Introduction

The first part of this chapter will introduce a brief description of petroleum reservoirs. A review of various types of oil rocks is discussed in Section 2.4. Also, distinctive features of oil rocks, such as wettability, porosity, absolute permeability, relative permeability, and pore size distribution, are stated in this section. The second part includes the review of oil recovery and its main phases during crude oil extraction. In addition, comprehensive information on the different thermal techniques, which have been applied to enhance heavy oil recovery (EOR), is discussed.

2.2 Heavy oil

Unlike conventional oil, which is typically represented by light oil, unconventional oil, mainly heavy oil and bitumen, has complex nature. Unconventional oil represents the largest proportion of the total oil reserves in the world. Heavy oils have high density and viscosity, with API gravity of 10 to 20^o according to the American Petroleum Institute. However, bitumen and oil sands have a higher density and viscosity (having API gravity less than 10^o) (Curtis et al., 2002, Shah et al., 2011). The main feature of unconventional oil is that oil cannot be extracted under natural conditions, and, in general, needs extra heat to mobilize the oil, which results in increased recovery expenses (Santos et al., 2014). Moreover, the heavy oil and bitumen have high asphaltenes and resins, as well as high sulfur and some metals such as nickel and vanadium. Generally, the type of the source rock, thermal maturation and alteration can determine the composition of the heavy oil and bitumen (Meyer, 2003).

2.3 Oil Reservoirs

In general, reservoirs hold oil in tiny spaces within rocks which have porosity and permeability allowing hydrocarbons to move freely. Migration of hydrocarbons, because of their relatively low density, starts through porous media as a leakage to find a convenient path toward the surface or to go upward until it finds non-permeable cap rocks where it is trapped before reaching the surface. These hydrocarbons were formed as a result of deposition of inorganic and organic materials after they become subject to a high temperature without oxygen. Many layers of sands bury the organic materials and get compressed together to form rocks that eventually may lie at depths of a thousand feet. These source rocks could be carbonate or sandstone rocks (Dandekar, 2013).

2.4 Oil Reservoir Rocks

Petroleum reservoir rocks are basically composed of about 99% of the global total of sandstones and/or carbonates. These are sedimentary rocks, which are formed by precipitated debris such as minerals, organic particles, and vegetables at the Earth's surface or by chemicals deposition (Dim, 2015). Rock properties within the geological formation can be different from **one** position to another.

2.4.1 Sandstone Reservoir Rock

Sandstone is the most widespread reservoir rock, which accounts for about 80% of all reservoirs and 60% of petroleum reservoir rocks. Sandstone rocks are a collection of sand-sized mineral particles and they are mostly formed from grains of quartz (silica

SiO_2) as seen in Figure 2-1(Bafarawa, 2015). Sandstone is often aligned in successive beds, or in a simply overlapped manner (Dim, 2015).

Figure 2-1: Outcrop of Sandstone Great Heck Quarry, Mansfield Nottinghamshire (Dim, 2015).

2.4.2 Carbonate Reservoir Rock

Carbonate rocks are composed of particular limestone ($CaCO_3$) and/or dolomite which consist of $CaCO_3$ and $MgCO_3$ as shown in Figure 2-2. The characteristic of the high heterogeneity in the carbonate reservoir rocks leads to create many challenges, such as defining the sort of porosity, the connectivity, and the behaviour of fluid flow inside the reservoir (Dim, 2015). Carbonates are created from chemical deposits and organic components. Physically, carbonate rocks can exist in many forms such as spongy, chalks and cavernous (Bafarawa, 2015). Shaly is a common kind of carbonate, but marls, containing 35 to 65% clay and 65 to 35% carbonate, do not have the ability to hold fluids because the shale represents a small ratio within the rock (Tanko, 2011).

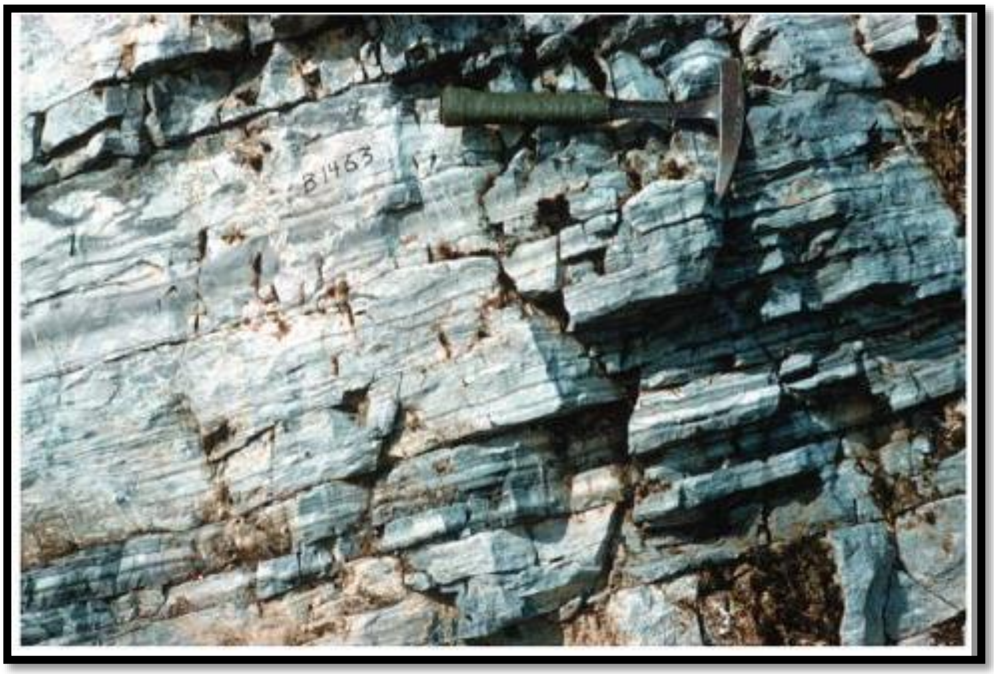

Figure 2-2: Photograph of Limestone, Black River, Alaska, United State (Dim, 2015).

2.5 Rock Properties

2.5.1 Wettability

Wettability is defined as the ability of a liquid to wet, and be in contact with, a solid surface. (Bafarawa, 2015). The wettability is considered one of the most significant characteristics of a formation of reservoir rock pores which plays a profound role in the determination of the oil production efficiency (Maitland, 2000). Wetting force is classified as a crucial factor that affects the behaviour of the hydrocarbon reservoir. A knowledge of formation wettability is important to account for the saturation degree, such as gas, oil and water distribution, within reservoir rock (Dandekar, 2013). For reservoir rock, wettability is categorised as either heterogeneous or homogeneous. Further, heterogeneous wettability is classified into groups. First, fractional wettability indicates non- uniform wettability in which the distribution of the oil/water wet surfaces, through the reservoir rock, are random. Second, mixed wettability depicts a particular state of fractional wettability in which the mobile oil phase, throughout the reservoir rock, remains in the large spaces, while the water-wet invades the smaller pores (Rezaei, 2010). The basic principle of wettability is clarified in Figure 2-3.

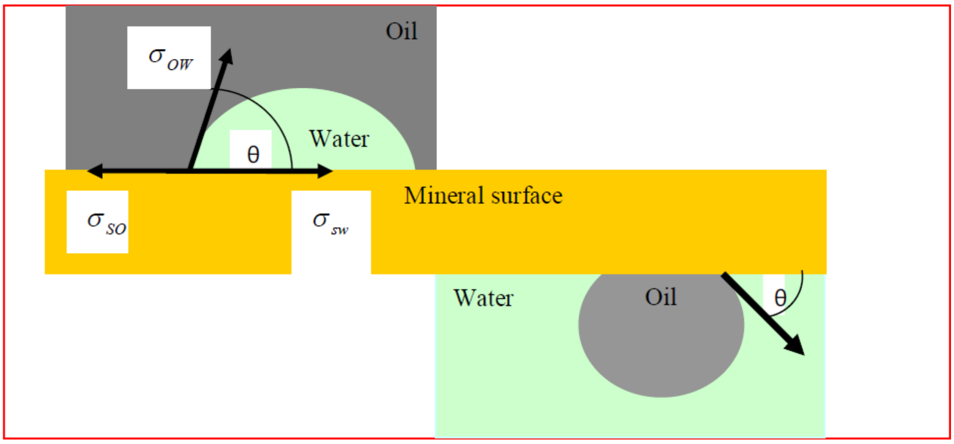

Figure 2-3: Graphical illustration of a two immiscible liquids system in contact with a solid surface (Dandekar, 2013).

From the schematic presented in Figure 2-3, the value of the adhesion tension can be computed by the following equation:

$$A_T = \sigma_{SO} - \sigma_{SW} \tag{2.1}$$

where σ_{so} is the interfacial tension between the surface and the oil (lighter phase) and σ_{sw} is the interfacial tension between the surface and the water (heavier phase). θ is the contact angle between the solid surface and the liquid, which is measured through the heavier fluid phase in the system, and this contact angle can range from 0 to 180°. The equation above can be written in terms of the angle cosine as follow:

$$\cos\theta_{OW} = \frac{\sigma_{SO} - \sigma_{SW}}{\sigma_{OW}} \tag{2.2}$$

Therefore:

$$A_T = \sigma_{OW} \cos \theta_{ow} \tag{2.3}$$

Based on the Equation 2.3, when the value of the adhesion tension is positive, it is an indication that the preferential liquid to wet the solid surface is the denser phase, whilst negative adhesion tension refers to that the wetting phase is the lighter liquid. In the case of adhesion tension is zero, indicating that the wettability of both phases toward the solid surface is equal (Dandekar, 2013)

2.5.2 Porosity

Porosity is the ability of the oil rocks to hold or store fluids within void spaces present in the rocks. These fluids maintained in porous materials inside the petroleum reservoir rocks could be a two-phase flow of gas-water and/or oil. The spaces created within the rocks have various shapes depending on the grain sizes, and on how they have been compressed when they were buried by a sedimentary process millions of years ago in the earth (Dandekar, 2013, Bafarawa, 2015). Porosity is given as the fraction of the volume of void spaces in the oil reservoir rocks divided by the total volume, and its value is expressed as a decimal in the range from 0 to 1, or as a percentage from 0 to 100%. Mathematically, porosity is expressed by:

$$\varphi = \frac{V_P}{V_B} = \frac{Pore\ volume}{bulk\ volume} \tag{2.4}$$

The void space represents the combination of volumes of all the pores within a specified reservoir rock. If the rocks in a given reservoir are similar everywhere, therefore for the whole reservoir the pore volume can be determined by Equation (2.4) using the estimated rock's porosity. The reservoir's bulk volume can be calculated mathematically from the area and the thickness of the reservoir (Brun et al., 1977). However, a value of the porosity is rarely uniform across the reservoir where it changes with the site and the depth. Therefore, average porosity can be computed using a simple weighted average formula:

$$\overline{\varphi} = \frac{(\sum \overline{\varphi}_i V_{bi})}{V_b} \tag{2.5}$$

Where:

$\overline{\varphi}$: Average porosity of entire reservoir

$\overline{\varphi}_i$: Average porosity of segment (i) in the reservoir

V_{bi}: Bulk volume of segment (i)

2.5.2.1 Types of Porosity

In general, as a result of precipitation of materials that were initially inhumed, spaces, depending on the grains size, arises from those materials which are called porosity. This porosity represents an original or primary porosity. On the other hand, the geological processes of the rocks, followed the deposition processes, have resulted in origination another type of porosity which is called a secondary porosity. The void spaces or pores which were formed within the reservoir rocks as a result of the precipitation of the materials have been classified into three various types. Some of the pores have developed to be in connection with other void spaces, thereby creating a network. On the other hand, some of the pores have not and thus will be perfectly separated or closed, from contact with other void spaces. The third type is that spaces were joined to other pores but with dead-end or cul-de-sac (Dandekar, 2013).

Practically every porous material or oil reservoir rock has three kinds of pores: closed pores, open pores, and dead-end pores. A schematic illustration of these pore spaces is shown in Figure 2-4.

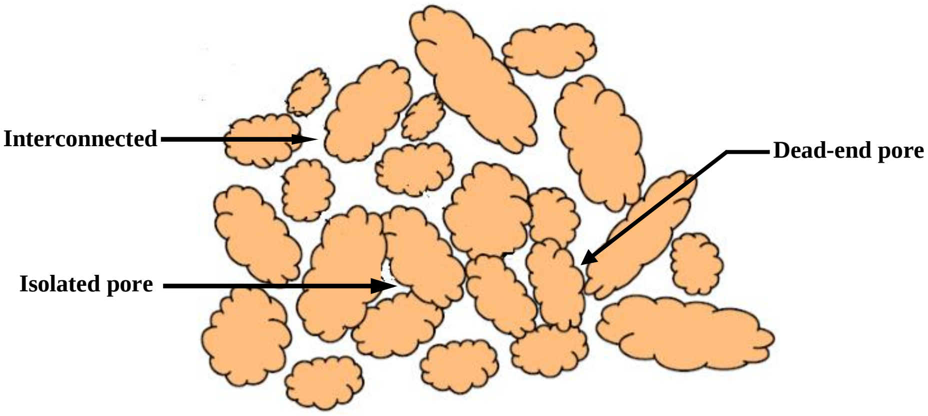

Figure 2-4: Schematic of different kinds of pores within pellet (Abu-Khamsin, 2004).

Geological, porous solids are often complex materials, with pores of different sizes and shapes connecting together to create a complex network. Pore sizes, according to the International Union of Pure and Applied Chemistry (IUPAC), have been classified into three groups: pores with size less than 2 nm which are called micropores, mesopores are between 2 and 50 nm, and macropores (> 50 nm). Furthermore, pores, based on their shape, can be categorized into three shapes such as a cylindrical shape which can be either open at two ends or open only at one end, ink-bottle formed, and funnel-shaped.

Based on these various types of pores, a porous medium can have an effective porosity, which is defined as the ratio of the fraction of pore volume where the fluids can circulate to the total volume, and ineffective porosity, which is known as the ratio of closed volume or entirely isolated pores to the bulk or total volume. The aggregate of effective and ineffective porosity of a reservoir rock represents the total porosity of the rock (Dandekar, 2013).

2.5.3 Absolute Permeability

Permeability is defined as the capacity of the porous medium in the rock to transfer fluids over a huge network of pores. When the rock is completely saturated with only one fluid then the permeability is called the absolute permeability. Relative permeability is when two or more fluids are flowing through the pores of the rock. Sweeping of fluids through the porous medium is proportional to the value of permeability **i.e.** when the permeability is large, more fluids can be produced from the reservoir rock for a specific set of conditions (Brun et al., 1977). By symmetry with electrical conductance, permeability is the facility with which fluids flow through the porous medium in the reservoir rock, or is the inverse of the resistance of the porous medium for transporting the fluids readily as shown in Figure 2-5 (Dandekar, 2013).

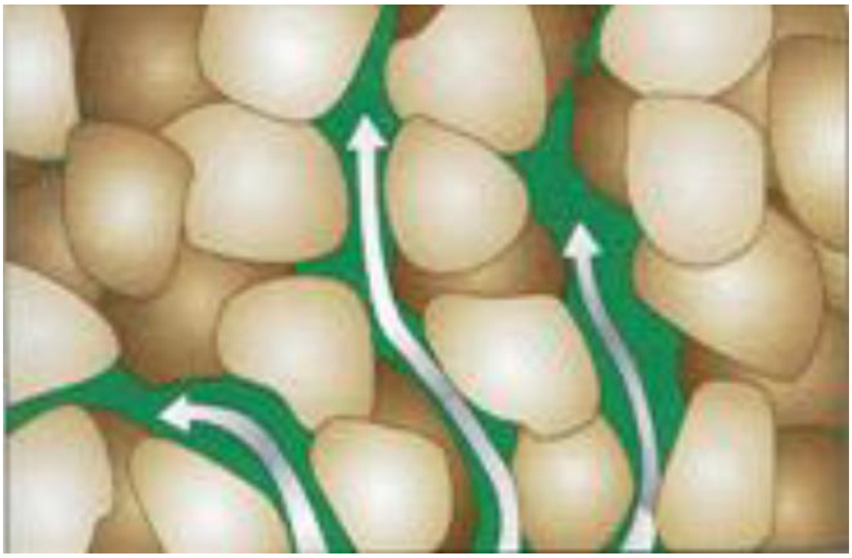

Figure 2-5: Illustration of permeability of a reservoir rock (MPG Petroleum, 2011).

The first attempt to figure out permeability was Darcy's experiments on a water purification plant in 1856. Mimicking Darcy's original investigation of water flow, many experiments have been conducted on packed beds of sand using different fluids. Permeability can be specified mathematically based on Darcy's law under the following assumptions:

- The fluid flow is at a steady state.
- The lateral sides of the rock are impervious to fluids.
- There is no reaction between fluids and porous medium.

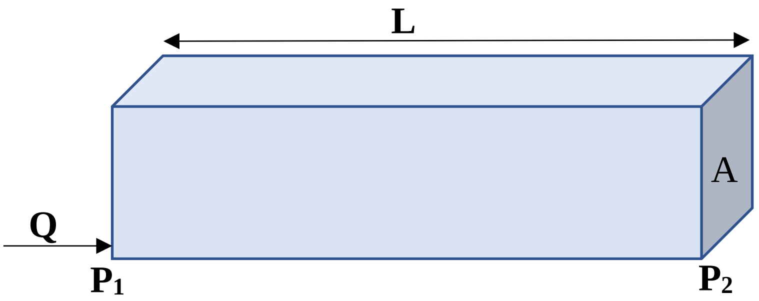

$$Q = \frac{kA}{\mu}\frac{\Delta P}{L} \tag{2.6}$$

Where: Q: Fluid flow rate ($m^3 . s^{-1}$).

K: Permeability (m^2).

A: Cross-sectional area (m^2).

μ: Fluid viscosity ($N.s.m^{-2}$).

ΔP: ($P_1 - P_2$) Pressure drop ($N.m^{-2}$).

L: Length (m).

2.5.4 Relative Permeability

Unlike absolute permeability which refers to the presence of just one phase in a porous medium, relative permeability measures the capacity of the rock that includes two or more fluids transferring through it. Oil reservoir rock is commonly filled by at least two phases, such as oil-gas, oil-water, or by oil-gas, and water. Therefore, estimation of flow in a multiphase system requires taking into consideration effective and relative permeability. The effective permeability is defined as a permeability of reservoir rock to an individual fluid, in the case of the presence of more than one fluid phase flows through a porous medium. The relative permeability quantifies the amount of the flow for each phase in a petroleum reservoir. Therefore, the relative permeability is very important in predicting the oil recovery and the production rate from the reservoir (Gawish and Al-Homadhi, 2008) The effective permeability has the same denote k for absolute permeability but with the addition the first letter of each fluid that is k_{eo}, k_{eg}, and k_{ew}, which represent the effective permeability of oil, gas, and water respectively. The relative permeability is expressed as the ratio of effective permeability of an individual fluid to the absolute permeability (Brun et al., 1977, Dandekar, 2013). It is mathematically computed by the following expression:

$$k_r = \frac{ke}{k} \tag{2.7}$$

where:

k_r: The relative permeability (dimensionless)

k_e: The effective permeability (m^2)

2.5.5 Pore Size Distribution

The typical pore size distribution (PSD) is widely used to characterise the structure of pore volume for disordered porous materials. It is used to improve structural models and understand the behaviour of heterogeneous catalysts like the activity and selectivity (Hitchcock et al., 2014a). Thus, good accuracy in computing the PSD is required. The PSD affects the distribution of fluid saturation in pores. The porous medium within oil reservoir rock is classified into three different size types: small, medium, and large. These porous solids are also called as micropores, mesopores, and macropores. Figure 2-6 clarifies these clusters of different pores according to a typical mercury intrusion capillary pressure curve. Many different methods can be applied to obtain the pore size distribution in the rock, but the more common techniques used are mercury porosimetry and differential scanning calorimetry (DSC) (Bafarawa, 2015).

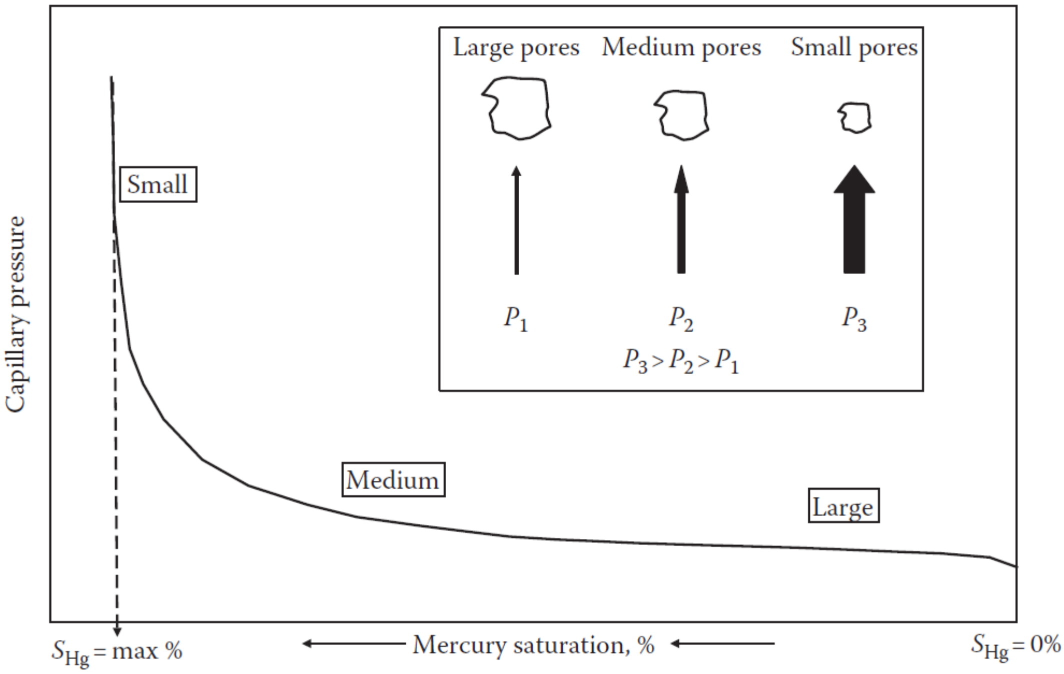

Figure 2-6: Plot represents the relation between mercury saturation and the imposed pressure. The unusual direction of the x-axis variable (mercury saturation) is a convention often adopted in the oil industry (Dandekar, 2006).

2.6 Oil Recovery

Oil usually is produced while the pressure of the reservoir is high enough to push the oil upward, this process called a primary or secondary recovery. When the pressure declines, other techniques are used to increase the oil production. This technique called enhanced oil recovery (EOR) which is utilized after the primary and secondary recovery. It includes using other fluids to swap the oil. The amount of the oil, extracted by the enhanced oil technique, is affected by several parameters such as the oil viscosity, the permeability of the rocks and the pressure surrounding the rocks. The kind of the rocks plays a significant role in the efficiency of the recovery process. When the rocks are a sandstone type, which is permeable rock, then the hydrocarbons can move freely, whereas, in the non- permeable rocks, such as shale type, they are not allowed to flow through. Generally, the amount of the heavy oil which, in the original place, can be extracted from the reservoir is about 10%. However, using some techniques to enhance the heavy oil recovery, such as In-Situ Combustion, could increase the recovery percentage by up to around 80-85%. For this reason, the recovery techniques are considered very important to compensate for the shortfall as a result of using the oil. There are three main methods of oil recovery namely, primary, secondary and tertiary (Dandekar, 2013, Defay et al., 1966).

2.6.1 Primary recovery

In this stage, the first stage of the recovery process, the underground pressures are the responsible for pushing the oil up to the surface. Therefore, the required pressure in the reservoir should be high enough to be able to force the oil toward the surface. Also, the required underground pressure can be supplied by the liquids present within oil, such as natural gas, gaseous fuels, and water. Usually, the amount of the oil which can be extracted from a reservoir by underground pressure is about 20% (Babusiaux, 2007).

2.6.2 Secondary recovery

When the underground pressure of the oil reservoir starts depleting, then it will be difficult to force the oil upward to the surface. Therefore, secondary recovery could be used as a convenient alternative to the primary recovery. In this method, different techniques can be applied to help in increasing the oil recovery from the reservoirs which are suffering declining pressure. Pumps, usually are utilized to push the oil out to the surface. Moreover, several techniques, involving injection of some fluid such as water, natural gas, air, carbon dioxide or any proper fluid to the reservoir, are used to provide the pressure required to bring the oil out of the reservoir. About 25 to 30% of the oil from the reservoir can be extracted using secondary recovery (Babusiaux, 2007).

2.6.3 Tertiary recovery

Enhanced oil recovery is used when the oil is no longer extracted by primary and secondary recovery. In this technique, the viscosity of the oil is reduced via using thermal methods in which oil is heated to be more mobility to recover. The most common method used in tertiary recovery is a steam injection. About 5 to 10% of oil can be extracted using tertiary recovery (Babusiaux, 2007).

2.7 Enhanced Oil Recovery

As mentioned above, production of oil goes through three main stages where several techniques are used to gain the highest extraction of crude oil. The purpose of these techniques is to drive oil into the reservoir well, by making it more mobile, so that it can be pumped via the producer well to the surface. The stages are applied to the oil reservoir sequentially based on the suitability of the reservoir for production. At the third phase, techniques applied are called Enhanced Oil Recovery (EOR). Employing these techniques can considerably increase extraction efficiency and raise the oil production to maximum levels (Lake, 1989). Generally, EOR techniques can be classified into two methods, which are namely thermal and non-thermal method. In this study, a thermal method will be considered.

2.7.1 Thermal Methods

Thermal methods are considered the most sophisticated amongst the techniques which are used to improve oil production, and they were used for the first time in 1950. These techniques have been successfully applied in many countries especially in Canada, Indonesia and Venezuela, and they are quite appropriate for heavy oil and bitumen which have API gravity between 10 to 20°, and tar sand with API gravity less than 10°. Technically, thermal methods provide heat to the oil reservoir, which causes vaporization of some of the oil. This process leads to a great reduction in the viscosity, thereby moving oil toward the producer will be easier (Thomas, 2008).

2.7.1.1 Cyclic Steam Stimulation (CSS)

Cyclic Steam Injection is an efficient method to increase the production of heavy oil. This technique is also named "Huff and Puff", which includes three stages, steam injection, steam soaking and finally producing oil. Figure 2-7 shows these stages and it is clear that the process, which used one well for both injector and producer, is repeated to improve the rate of oil production. In cyclic steam injection, oil originally in place is heated by injecting steam for a period of time and the steam is left to soak in for several weeks (Ali, 2003).

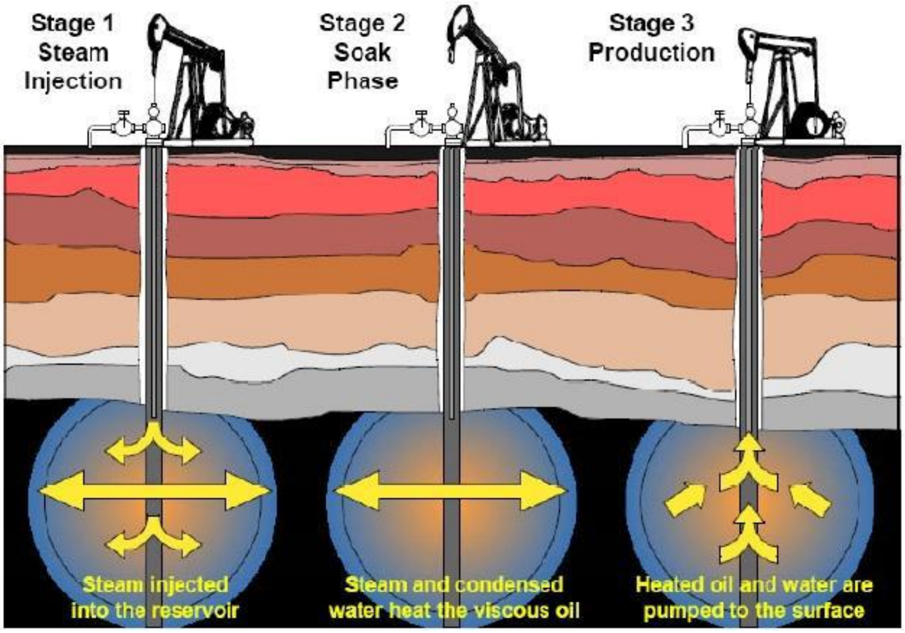

Figure 2-7: Cyclic Stem Injection (Bjørnseth, 2013).

The amount of injected steam must be sufficient for this process, and during this time the well should be closed. As a result of oil heating, the viscosity of oil will be reduced. After that, the reservoir is opened. Initially, the oil will be produced by normal flow, and then by pumps (Clark, Graves et al. 2007, Alvarez and Han 2013).

High production rates are reached quickly in the production process, and this rate can be kept constant for a short time, before gradually dropping over several months. Once the rate of the oil production becomes uneconomic, the steam injection is repeated and the process continues with increasing ratio of steam to oil from 3:1 to 4:1 during the process (Shah et al., 2010).

2.7.1.2 Steam Assisted Gravity Drainage (SAGD):

Steam-assisted gravity drainage (SAGD), which is a familiar form of steam flooding, is an effective method to enhance oil recovery with low API (Li, 2010). (Butler and Stephens, 1981) developed SAGD to improve bitumen recovery in the fields in Alberta. The typical SAGD configuration is presented in Figure 2-8. Two horizontal wells are used in parallel in this process; the separation of oil from the sand by steam utilising gravity force is the main principle of this technique. Steam is injected through the injector which is located towards the top of the reservoir, and the producer will be towards the bottom of the reservoir. A steam chamber will be created as a consequence of steam rising to the top of the reservoir. The produced temperature due to this steam causes a large reduction in the oil viscosity, making the heavy oil more mobile, and by gravity, the mobilized oil is drained to the producer well. A high value for vertical permeability represents the vital part needed for the success of the process. The rate of production is affected by many parameters like the pressure of steam, and oil properties such as density, viscosity, and heat combustion, in addition to the distance between injector and producer and other properties.

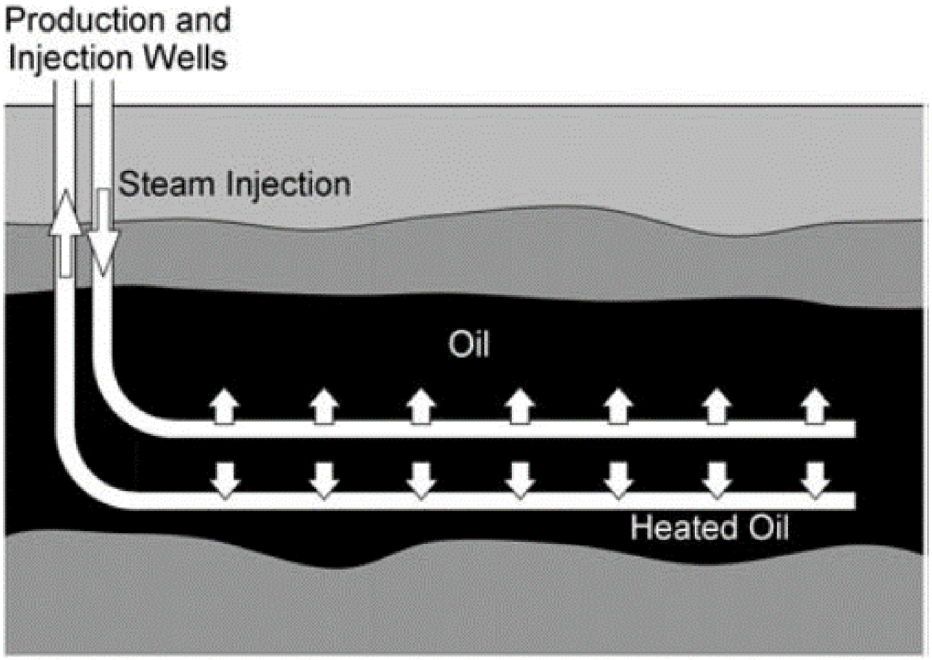

Figure 2-8: Steam Assisted Gravity Drainage (Shah et al., 2010).

A laboratory scale study has been conducted on the Athabasca oil sand. It was found that the total recovery of the oil was 50% of the original oil in place. The ratio of steam to oil ranged from 1 to 3 cm^3 steam per cm^3 oil at standard conditions (Turta and Singhal, 2004). However, the productivity of the SAGD process can be affected by the nature of the reservoir, and that is reflected in the efficiency of the method. Geologically, the recovery process in SAGD is extremely affected by reservoir heterogeneity through the change in permeability of the rocks within the layers of the reservoir. Also, the presence of barriers in the reservoir, such as shale or mudstone, would impede steam rise and mobility of oil toward the producer well (Gates and Larter, 2014). Hydraulic fracturing and mobility control methods are applied using foamed steam to investigate the effect of the reservoir heterogeneities on the performance of SAGD technique. Geologically, the Athabasca reservoir includes randomly-distributed shales. The triangular shape of the steam chamber is SAGD causes different distinctive lengths. The upper section of the chamber, the larger heated area, in which the steam flow is comparatively long, and the region of propagation of the heated oil surrounding the chamber is relatively wide. The distinctive length of the flows in this zone is relatively long. In contrast, in the lower part of the chamber, the shorter heated area, the steam, and oil flow only in a small area around the well. Therefore, the steam and oil in this region are of relatively short distinctive length (Chen 2009).

The Athabasca oil reservoirs have layers of water and gas zones at the top of the reservoir so that penetration of steam into these zones in SAGD process results in a great loss of heat, and that represents a big challenge to recover bitumen by this process for the Athabasca fields (Bao, 2012).

2.7.1.3 In-Situ Combustion (ISC)

Another thermal method is the in-situ combustion technique, in which gas, usually air or oxygen impregnated air, is injected through a vertical injector to the reservoir (Shah et al., 2010) as represented in Figure 2-9. This injected oxygen and the presence of a heater cause ignition inside the well, where part of hydrocarbons is burned, resulting in generation of the heat required to reduce the oil viscosity. However, the amount of the air injected into the reservoir controls the burn direction. Once the surrounding rock is heated, the heater is turned off, but keeping the injection of air, to sustain the propagation of the combustion front (Guerra Aristizábal, J., & Grosso Vargas, L., 2005). The cracking process for hydrocarbons will be occurring as a result of high temperatures, as well as evaporation of light oil and water in place, in addition to the coke formation as a solid phase. The created firefront will be in continuous movement forward which drives the component mixture of burning gas, steam and hot water ahead. Consequently, the oil viscosity will be reduced ahead of the front, and the component mixture displaces the oil in the direction of the producer (Olayiwola R. and Ayeni R., 2011).

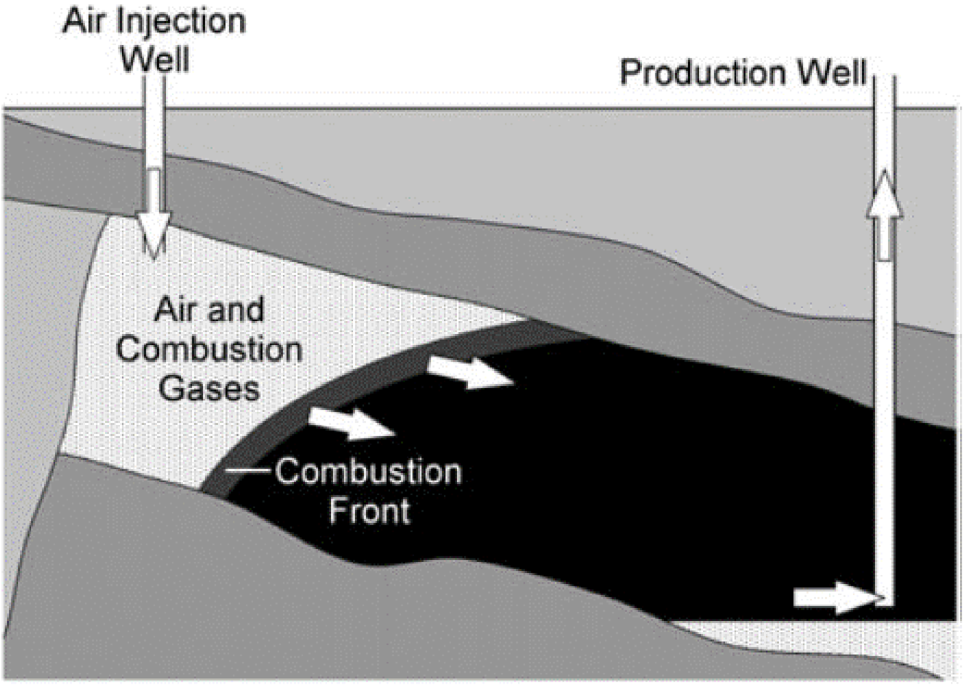

Figure 2-9: In-Situ Combustion Method (Shah et al., 2010).

The in-situ combustion method has been applied for more than eight decades. In the past, the process was mostly used in heavy oil with sandstone reservoirs. The in-situ combustion technique is appropriate to apply for a wide range of different oil properties. (Karimi G. and Samimi A., 2010). In this technique, also called fire flooding, the high temperature is created in a limited area and may reach to 600 ℃. There is no loss in the wellbore or surface heat, and a slight loss in the amount of heat to the overburden and underburden. Therefore, thermal efficiency is quite high in this process (Thomas, 2008). In some cases, water is injected with air to increase the steam formation which promotes heat recovery and also reduces the required air during the injection process (Guerra Aristizábal, J., & Grosso Vargas, L., 2005).

Although in-situ combustion is employed in a wide range of reservoirs, many problems may appear through the process. The main problems are intense corrosion, production of poisonous gas and gravity override (Thomas 2008). Overriding is a phenomenon in which the lighter vaporized hydrocarbons, steam and combustion gases rise up into the top of the reservoir to be above the oil zone. This phenomenon causes a decrease in the efficiency of the combustion process. Therefore, water injection with air could help the combustion process to maintain its performance well (Guerra Aristizábal, J., & Grosso Vargas, L., 2005).

High reduction of the oil viscosity takes place due to heat generated, the gas formed from the burning hydrocarbons and the created steam. These phases, collected together, push the displaced oil through a long distance across the thick cold oil region before reaching the producer (Turta and Singhal, 2004). During the forward burning front movement inside the reservoir, many types of zones (see below) will be created in the area which is located between the injection well and the production well due to the heat. Several important phenomena also happen through the process, including chemical reactions and mass transfer. Figure 2-10 explains the positions of the different zones and how temperature is changing from zone to zone.

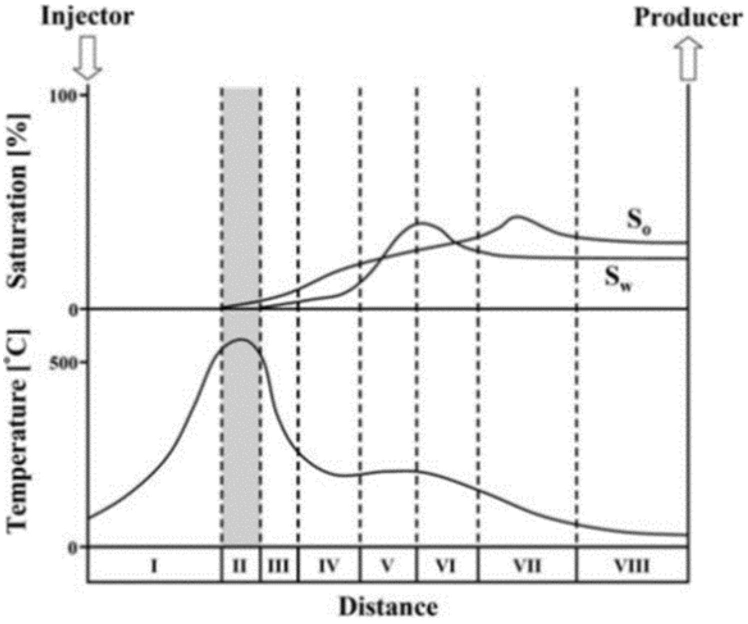

Figure 2-10: Block Diagram of Forwarding In-Situ Combustion (Shah et al., 2010).

Also, Figure 2-10 gives details about the distribution of oil and water saturations through their travels inside the reservoir. These zones can be described briefly as follows (Shah et al., 2010):

1- Oil is burned in the first zone by the air flowing from the injector in the direction of the combustion front. As a result of continuous air injection, the temperature increases in this zone but it is likely that small amounts of oil may remain unburned. This zone is called the burned zone.

2- This zone, which is called the combustion front, has the highest temperature among the zones. In this area, the oxidation process takes place for hydrocarbons via mixing them with a certain amount of oxygen. This amount of oxygen can be calculated from the fuel used in this process.

3- and 4- represent the thermal cracking/evaporation region. This zone includes cracking of the crude oil due to the high temperature which leads to upgrading of the oil and evaporation of the lighter hydrocarbons. Then vaporized oil comes back again to the original oil in place after its condensation.

5- In this section, the steam plateau is to come in downstream while most of the oil is travelled ahead of the steam. This feature causes a high reduction in the oil viscosity. Thermal cracking processes for the crude oil take place in varying degrees depending on the temperature; oil which cannot move easily goes through steam distillation and moderate cracking takes place for the remaining oil.

6- At the border of the steam hill, where the temperature is less than the temperature of steam saturation, water accumulates that reduces in temperature and saturation as one looks downstream, with a resulting rise in oil saturation.

7- Most of the oil light ends, which were a result of cracking processes of the heavy oil, reach this region by travelling with the oil moved from upstream.

8- Beyond lays the undisturbed original reservoir.

2.7.1.4 Toe-to-Heel Air Injection (THAI)

The reduction of the viscosity of the oil is the main aim for processes of enhanced heavy oil recovery. To help the immobile oil to be capable of motion easily inside the reservoir, air is the most commonly utilized material through In-Situ Combustion method for generating the heat which is the key factor in the process. Although the ISC technique has potential benefits, this process is facing significant challenges to its success in many cases because controls on combustion fronts are limited and there is difficulty in the travel of oil toward the production well. Stability under gravity is a vital part of a conventional ISC process. Thus, gravity segregation between the hot region, which represents burning gases, and the cold region, which represent cold oil, may lead to further decrease the effectiveness of the reservoir sweep (Greaves and Turta, 1997; Kulkarni1 and Rao, 2004).

Toe-To-Heel Air Injection (THAI) method is a relatively new process, which was invented to solve the problems that gave rise to the failure of classical ISC processes. In the THAI process, a horizontal producer is used instead of a vertical producer as in ISC process as shown in Figure 2-11. Unlike the conventional ISC process, in which the phenomenon of gas override occurs which is considered a negative feature, the arrangement of the injector and the producer in THAI process effectively reduces or prevents this phenomenon (Greaves et al., 2000).

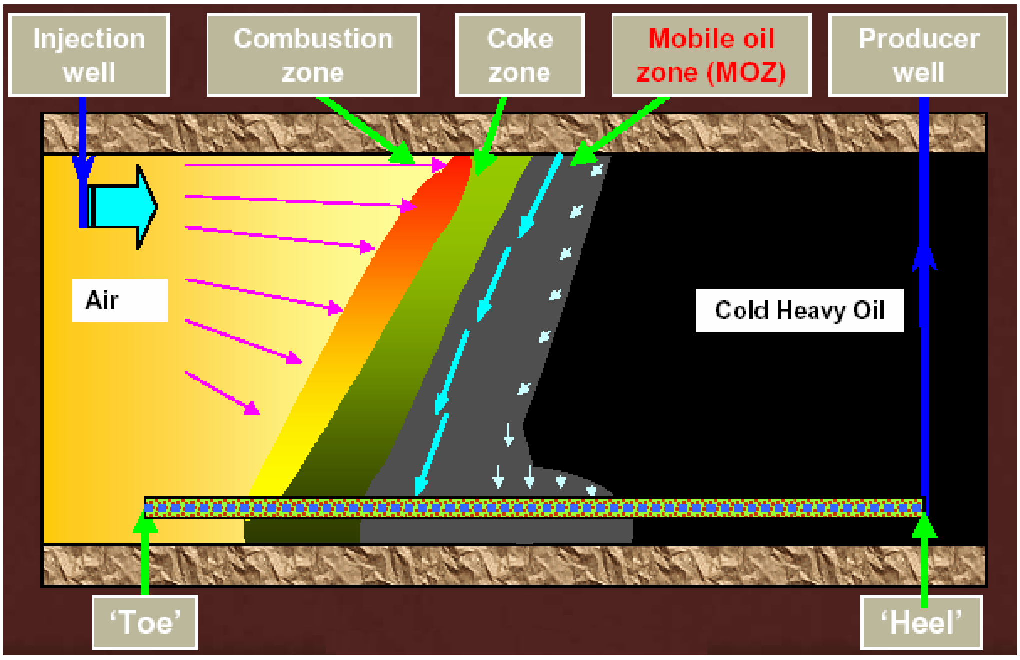

Figure 2-11: Schematic configuration in THAI (Kulkarni1 and Rao, 2004).

Furthermore, coke formation, as well as the fire front propagation through the horizontal well, effectively close the ‘‘toe’’ and preventing gas bypass. This property arises from the huge extension of the combustion front which covers all of the distance along the producer from toe to heel (Greaves and Turta, 1997; Kulkarni and Rao, 2004). Therefore, THAI is quite stable and robust compared to the conventional in situ combustion process.

In the THAI process, the region around the injection well is heated prior to air injection, to create communication between the injection and the production wells. This also results in generating some coke as a fuel for initiation the combustion front and to sustain its propagation along the reservoir (Rabiu Ado, 2017). The combustion front progresses forward inside the reservoir and generates a quite high temperature, which reaches over 600 °C. This rise in the temperature is accompanied by a reduction in the viscosity of the oil and then the immobile oil sweeps through a narrow zone, named a mobile oil zone (MOZ), toward the reservoir ahead. In addition to the MOZ, which is in contact with the cold oil region, combustion and coke zones are created upstream of the MOZ. Moreover, the hydrocarbons with high molecular weight, due to the high temperature created in the combustion zone, are subject to the thermal cracking producing lighter oil. The thermal reactions take place in the coke and the MOZ zone. Oil produced with other products proceed in a short distance through the MOZ toward the horizontal producer, resulting in higher levels of recovery in the THAI. On the other hand, oil produced in the conventional ISC needs to travel a long distance, passing in the cold oil region, resulting in low rate production control problems (Shah et al., 2010, Kulkarni and Rao). In this process, the amount of gas injected is maintained without loss, unlike in the classical ISC method where a considerable amount of air is lost. This is because the displaced oil is produced from the mobile oil zone immediately rather than having to go through the cold oil zone. In addition, because the oxidation process is taking place at high temperatures, the gas is completely prevented from getting to the cold oil zone (Weissman, & Kessler, 1996; Greaves and Xia, 2000).

The THAI process has been tested experimentally in the laboratory and it was found that the progress of the fire front was quite stable, as the fire front remained anchored along the horizontal production well. As a result, high productivity of oil recovery has been obtained. Moreover, unlike the traditional ISC technique, the oil produced in the THAI process needs a much shorter time to reach the producer well, and that increases the rate of oil production (Xia et al., 2003, Turta and Singhal, 2004). In addition, it was found that oil recovery in this technique is higher than others, where it is able to give recoveries reaching up to 80% of oil originally in place (OOIP) (Rabiu Ado, 2017). Furthermore, the appropriate method, for enhanced oil recovery, is chosen depending on the properties of the reservoir such as depth of the reservoir, thickness, pressure, fluid saturation, etc. The THAI process can be applied to large-scale reservoirs unlike other techniques, such as CSS and SAGD (Oskouei et al., 2011, Shah et al., 2010).

Sands white was the first experimental project in which Petrobank Energy and Resources Ltd applied THAI to enhance the oil production, and that was in 2006 in Alberta, Canada at Christina Lake. The project was conducted at a well which comprised of three divisions with three injectors and three horizontal producers. The process was run from March until July during 2006. At the beginning of the process, steam was injected alone into both the two vertical and horizontal wells. Then in July 2006 air was injected which caused automatic burning of the oil inside the reservoir. The temperature of combustion reached was up to 800 ℃ and the maximum rate of produced oil was 2000 barrels per day. In comparison with the original value of 7.9° API gravity of the bitumen, the API gravity of the produced oil increased about between 2.7 and 8.2 degrees. Further, because of the high reduction in the produced oil viscosity, the small sand amount associated with the production, which represents less than 1%, is simply separated. Therefore, the amount of the needed oil to transport via pipeline to the refineries is very small compared to the required amount of the oil produced from CSS and SAGD techniques (Shah, 2011). In this technique, the pressure gradually changed during the migration of the oil between the injector and the production well, leading to the horizontal producer acting as a pressure sink. Also, all fluids go in the direction of the producer ahead of the fire front without passing through the cold oil zone. Consequently, the THAI process determines the direction of its own path automatically (Hwessa, 2009).

Greaves et al. (2012b) have employed experimental results obtained from a 3D combustion cell on Athabasca heavy oil to validate a numerical simulation model of the THAI process. Several significant parameters, such as the difference of peak temperature, cumulative oil produced, the rate of produced oil, the concentration of oxygen in the producer, and API gravity of the upgraded oil, have been investigated and compared with the experimental results. Excellent matches of the predicted rate of oil produced and the cumulating oil production were obtained in the experiment. The results obtained for some dynamic parameters, such as peak temperature, API gravity of the oil production, and produced CO_2 concentration, were in, overall, good agreement with the results in the field pilot findings. The amount of coke formed, which is used as a fuel to sustain the combustion front propagation, occupied about a quarter of the sandpack volume.

Further, Fatemi and Kharrat (2008) have modified a 3D simulation model to study the effect of networked fractures in the reservoir on the performance of the THAI process. Different reservoir parameters have been tested to investigate the process effectiveness on fractured and conventional THAI models. It was found that the parameters, such as API gravity of the upgraded oil, oil recovery factor, and the sweep efficiency of oxygen, are the highest in the case of the conventional model. As a result, the performance of the THAI technique is reduced in the case of a fractured reservoir. Also, they found that the rate of injected air affects the activity of THAI. Therefore, optimisation of the injected air rates should be considered essential for use of THAI with a fractured reservoir.

Moreover, various well arrangements have been tested to investigate parameters that affect the THAI process achievement. The effect of variable configurations of injectors and producers, which can be positioned at different transverse distances, have been investigated. In addition, the influence of the depth of the vertical injector and the length of the production well has been investigated. The simulation results presented showed that the THAI process reached perfect ignition and very steady combustion front propagation irrespective of well arrangement. A comparison of the results revealed that the configurations in which the injector is vertical are the best design for THAI in the field. However, the horizontal injector was found to be feasible in the case of simulation models. Although, accelerated oxygen breakthrough and reduction in areal sweep efficiency were observed when the horizontal producer used is very long. In the case of that, the producer is very short, a high temperature is generated which may lead to decomposition of the carbonate rock, and this decomposition of the rock caused a reduction in the oil recovery factor.

2.7.1.5 The Catalytic Upgrading Process In-Situ (CAPRI)

A catalyst can be added to the THAI process to develop a new technology for enhanced oil recovery, which is called CAPRI, and shown schematically in Figure 2-12. The catalyst is placed in the form of an annular layer packed bed around the production well, to create a catalytic reactor at the bottom of the reservoir (Gates et al., 2008, Hart et al., 2013, Dim, 2015, Ado, 2017). This technique aims to improve heavy oil upgrading in addition to increasing the rate of oil recovery. The THAI process creates the appropriate conditions for the reaction, taking place ahead of the burning region, as reactants from the mobile oil zone come in contact with the catalyst.

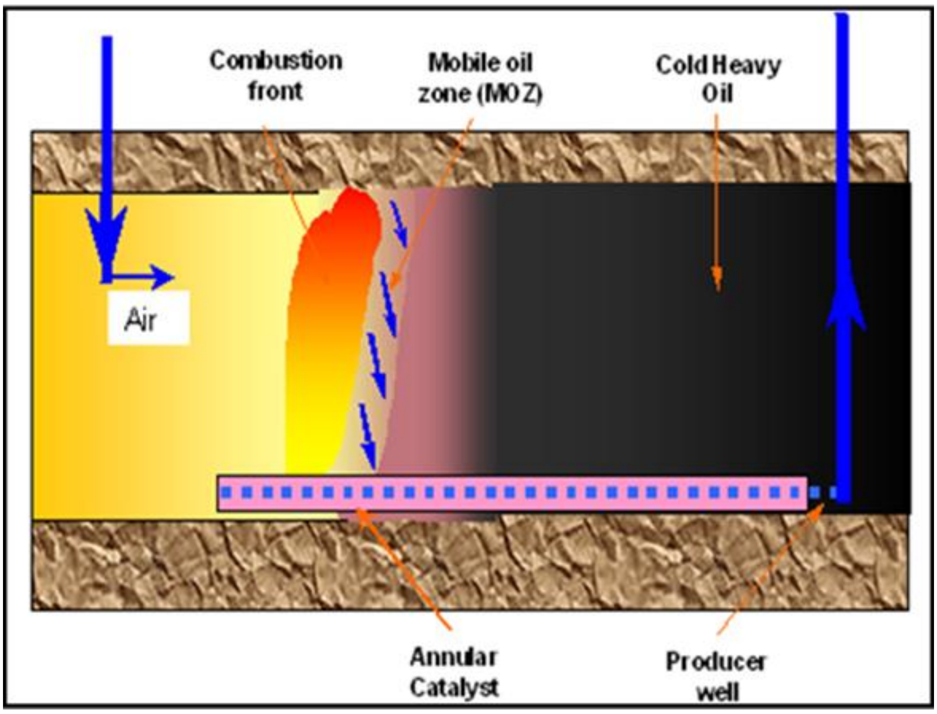

Figure 2-12: Schematic of the THAI-CAPRI process (Turta and Singhal, 2004).

As the displaced oil passes through the catalyst layer, further upgrading occurs for the produced oil by catalytic transformation (Greaves and Xia, 2004). The oil upgrading process is thought to take place via carbon-rejection, which occurs through thermal cracking of heavy oil, and the reactions of hydrogen addition at the surface of a hydroconversion (HCT) or hydrotreating (HDT) catalyst (Greaves and Xia, 2004). The temperature of the reaction that is required on the surface of the catalyst is at least 300 °C for effective downhole cracking (Weissman, 1997). Many impurities accompany the produced oil, through enhanced oil recovery processes, which include several inorganic elements like vanadium, nickel, etc., and amounts of asphaltenes and sulphur. THAI-CAPRI provides the benefit of reducing these contaminants by leaving them in the ground during extraction or simply removed during oil production through desulphurization, demetalization and deasphaltenization processes. This feature decreases the influence of these metals on the environment compared to the other techniques (Weissman, 1997).

Many researchers have studied the efficiency of THAI-CAPRI to improve the production of heavy crude oil under various operation conditions, several of those are discussed below. Six groups of catalytic experiments in two 3D combustion cells were studied by Xia and Greaves (2001), for the upgrading of the Wolf Lake oil with API gravity of 10.5°. The study was conducted using both methods: THAI process and THAI with catalytic upgrading. In these tests, the NiMo and CoMo type catalysts were used at temperatures between 500 and 600 ℃. It was demonstrated that the degree of oil upgrading, using the catalytic process, was around 7° API gravity higher than when using the THAI process alone, in which the API gravity of the produced oil was raised by 10°. Considerable viscosity reduction of the produced oil was observed, it reaches 1000 cp (at 20 ℃), with a high recovery of oil of about 85 % of original oil in place.

Xia et al. (2002) have conducted laboratory scale tests of the THAI-CAPRI process in which the feed was Lloydminster heavy crude oil, having 11.9° API, and CoMo loaded alumina ($CoMo/Al_2O_3$) was employed as a catalyst. It has been recorded that the recovery percentage of the heavy oil in original place was 79%, with improved the API gravity of the produced oil to be 23°, and reduced the oil viscosity by 20 to 30 cp.

Another laboratory experiment has been reported by Greaves and Xia (2004) in which two trials were carried out, where the CAPRI feed was a Heavy Wolf Lake oil with API of 10.5° and a NiMo hydrodesulfurization (HDS) pellet was used as a catalyst. They showed that there was a significant upgrade achieved in the produced oil. In addition, the recovery of the oil production had been improved by up to around 87%

of original oil in place. Also, it was noticed that, through the CAPRI stage, there is a high reduction in the asphaltenes content in the upgraded oil, and a substantial rise in the saturates levels. Moreover, removing the inorganic metals from the upgraded oil resulted in substantial environmental advantages.

Shah et al. (2011) have studied the optimisation conditions for the process by investigating many potential key factors such as the best catalyst, appropriate temperature, pressure, and the reaction conditions. Also, the study included the investigation of the upgrading process which occurred through the thermal cracking in the presence of a catalyst. The feed used in this study was provided by the Whitesands THAI-pilot, Alberta. Many types of catalysts, such as CoMo, NiMo and Zinc/Copper oxides loaded over alumina, were used in this experiment. The experiment was conducted at a temperature of 500 ℃ and at a pressure of 20 bar. It has been shown that the API gravity of the oil had risen from 6.1 to 18.9°, but the life of the catalyst was just 1.5 hr. Decreasing of temperature to 420 ℃ and 20 bar led to upgrading by API between 1.6 and 3°, but expanded the lifetime of the catalyst which reached 77.5 hr. Therefore, a balance between catalyst lifetime and upgrading performance should be taken into account via controlling the temperature.

Hart et al. (2013) have investigated the improvement of the oil and the activity of the catalyst in the CAPRI method. The process was accomplished in a microreactor at temperatures around 350 to 425℃ and at a pressure of 20 bar, with a 9.2 min residence time. They used a catalyst of $CoMo/Al_2O_3$ and two added gases of nitrogen and hydrogen. Whitesands heavy oil was applied in this process which was supplied by Petrobank Energy. They found that there was a rise in the value of API gravity between 2 and 7°, and a considerable reduction occurred in produced oil viscosity by 42 to 82 percentage points depending on the temperature of oil upgrading. It was also observed that there is a significant lowering of the coke deposited on the catalyst in the case of the hydrogen injection, compared to the coke formation in the nitrogen case.

Hart et al., (2014) have separately used three types of gases, namely hydrogen, nitrogen, methane, and a combined gas mixture to study their effect on the THAI-CAPRI process using heavy oil with 14 °API. This study was conducted at a pressure of 10 bar, a temperature of 425℃, and a ratio of gas to oil of 50 vol%, with $CoMo/\gamma Al_2O_3$ as the catalyst. They found that the API was increased by 4° with H_2, 3° with CH_4, 2.9° with blended gas and the least value of 2.7° occurred with N_2. Furthermore, they pointed that the main reason for the catalyst to be ineffective was coke formation over the surface of the catalyst, and the gas media played a vital role in determining the amount of coke formation. It was observed that using hydrogen gas leads to inhibition of coke deposition, promoting the reactions of hydro-cracking and hydrogenation giving more stability to the process. While, in the case of nitrogen, most of the oil upgrading happened by the rejection of carbon accompanied by a thick layer of coke formation over the catalyst.

Recently, a practical study has been conducted on dry combustion-tube to investigate the upgrading of Athabasca bitumen provided by Japan Canada Oil Sand Limited, using a commercial catalyst of NiMo supported by alumina (Abu et al., 2015). The experiment was tested under a pressure of 10.3 MPa, an initial temperature of 95℃, and 350℃ as the ignition temperature. The reactions occurring during this test involved the combustion process of the hydrocarbon, water-gas shift (WGS), steam gasification (SG), and hydrodesulfurization (HDS) reactions. It has been found that a high reduction in the sulphur and nitrogen in the produced oil was observed compared to the original feed. It is also noticed that the value of the API gravity was increased from 10.3^o of the used bitumen to a maximum of 18.8^o. Further, the produced carbon monoxide was efficiently converted via the water-gas shift reaction into hydrogen and carbon dioxide on the surface of the heated supported catalyst.

2.8 Catalyst pellets as a model of reservoir rock

As has been described earlier, reservoir rocks which produce oil and gas are typically sandstones and/or carbonates. These rocks were formed as a result of sedimentation from debris within the layers of the Earth or chemical deposition, and thus, the chemistry of the reservoir rocks is heterogeneous. In addition, natural reservoir rocks incorporate some metals as impurities, such cobalt, iron etc. (Dandeker, 2006), and, hence, it is difficult to evaluate the properties of the topology and structure of the reservoir rocks. Consequently, artificial pure rocks need to be a convenient alternative for the oil reservoir rocks.

Several different catalyst supports have been tested in this project, but, three catalysts in particular have been investigated in more detail, which are Q17/6 silica, Alumina and Houdry. All three of the chosen catalysts are typical supports for hydrocarbon reactions. Q17/16 (i.e. sol-gel silica), can be used as a standard support for precious metals (Pt, Pd, Ru, or Rh) during the hydrogenation of hydrocarbons. The alumina material is employed in the steam reforming of hydrocarbons. The silica-alumina (Houdry) is a hydrotreating or oil treating catalyst, since its surface involves different types of acidic site that are likely utilised for cracking reactions. The strength and the amount of acidic sites that are distributed over the surface of this catalyst have an effect on both the activity and selectivity of this particular catalyst and hence affecting the chemical reactions. The results for the mixed silica-alumina material were compared with data for pure silica and alumina materials to explore the impact of the surface chemistry on differential adsorbate wetting (Zhang et al., 2009, Sun et al., 2014).

Natural reservoir rocks are chemically and geometrically heterogeneous, and for many pore characterisation methods, it is difficult to deconvolve these two sorts of heterogeneity. Hence, model materials with only geometric heterogeneity were selected for this study. Reservoir rocks contain different minerals with different chemistry for instance, heavy metal ions such as Fe^{2+}/Fe^{3+}, Mg^{2+} etc. These are potentially high energy sites for nitrogen in gas adsorption, however, industrial silica materials do not have such impurities in their structure. However, these porous solids have similar geometrical and chemical properties to the silica in the petroleum reservoir rocks.

Silica gel is a form of silicon dioxide (SiO_2), which is synthetically prepared by dissolving of sodium silicate in acetic acid. When the gel is heated, water is thrown out leaving a hard, vitreous structure with voidage between the micro-particles (Richardson et al., 2002). The manufacturing process of disordered porous materials is based on hydrolysis of silicon tetrahalides under high-temperature flame in presence of oxygen and hydrogen (Eisenlauer and Killmann, 1980). These processing methods lead to a wide range of pore size distribution (PSD), and therefore, the geometry of the silica materials becomes heterogeneous. In addition, the high temperature used in the reaction determines the volume of the silica pore as well as the mean radius of the catalyst.

Moreover, heavy oil and bitumen cannot be refined in oil refineries unless convert them to light hydrocarbons. For these reasons, different types of catalysts have been tested in this study as a model of reservoir rock, and catalysts for upgrading heavy oil and bitumen to convert them to light oil prior to sending them to oil refineries.

Table 2.1 displays a list of various types of catalysts. Some have been used in previous studies, and also investigated in this project. Many researchers, such as (Rigby et al., 2003a, Rigby et al., 2008a, Rigby et al., 2008b, Gopinathan, 2012, Shiko et al., 2012, Hitchcock et al., 2014a), have investigated most of these materials in focusing on the properties of the materials surface and the mercury entrapment of the porous media. In this study, attention will be paid to measure pore diameter, pore size distribution, hysteresis generated between the plots, and emphases on doing a comparison between different methods. The materials have been provided by several commercial companies, namely: Micromeritics and Johnson Matthey. The pore sizes are lying between 3.5 and 30 nm.

Table 2.1: Several types of catalysts samples investigated in this project

Techniques / Samples	Gas sorption	Mercury porosimetry	DSC	NMR
Houdry H2-1	X	X	X	X
UOP FC-3P	X	X	X	X
LA 30-5P	X	X	X	X
E10823	X	X	X	X
E8547	X	X	X	X
RTK		X	X	
SA-S4		X	X	
Q17/6	X	X	X	X
CY 4F		X	X	X
NORTON SILICA		X	X	
LEONDRDS MK2		X	X	
CROSSFIELDS SI GEL		X	X	X
C30	X	X	X	
AL3984 T		X	X	X
AL3992		X	X	X
EKETJEN HA 3P	X	X	X	X

CHAPTER 3

CHARACTERISATION OF POROUS MEDIA

3.1 Introduction

This chapter describes the different experimental methods, which are used to characterise the pore structure within disordered materials. It will introduce the reader to the basic principles and the theoretical aspects of the techniques applied in this study. These techniques are gas sorption porosimetry, in which can be employed nitrogen and argon to probe porous system providing a wide range of information about the pore geometry, mercury intrusion/extrusion porosimetry, which provides valuable information that cannot be obtained from other techniques and mercury thermoporometry which uses entrapped mercury as a probe liquid. The CXT technique is also used immediately following mercury intrusion to image the materials intruded by mercury to identify the spatial distribution of entrapped mercury within void spaces of the porous system. Additionally, NMR cryoporometry is applied to investigate the effects of some phenomena on the accuracy of the pore sizes.

3.2 Gas adsorption porosimetry

In general, the adsorption process is the accumulation of molecules on a solid surface whenever it is soaked in or exposed to gas or liquid. In adsorption, a transfer process of molecules occurs from the fluid, which called the adsorbate, to the surface of the adsorbent (Coulson et al., 1991). Therefore, the adsorption can be defined as a rise in the material concentration, or in the fluid density, at the solid surface (Rouquerol et al., 2013). Different types of adsorbates, such as nitrogen, argon, helium, hydrocarbons and carbon dioxide can be employed to characterise disordered materials (Jennings and Parslow, 1988). However, nitrogen is the most common adsorbate used for adsorption porosimetry. This is because that nitrogen has accessibility to the pores of most disordered solids due to its small molecule size (Allen, 2013). It is also inexpensive and readily available.

3.2.1 Background and theory of adsorption

The basic principle of adsorption involves transferring the mass of molecules from the fluid onto the solid surface of another phase. Based on the forces existing between the adsorbent and adsorbate, the adsorption process can be divided into two types. These types are physical and chemical adsorption, which are also named physisorption and chemisorption properties. Unlike physical adsorption, in which the attraction forces present between the adsorbent and adsorbate are very weak and represented by Van Der Waals forces, in chemical adsorption, the attraction forces are strong because some specific interaction occurs on the solid surface with the adsorbate, leading to the creation of chemical bonds (Masel, 1996). Physisorption takes place in three stages as the concentration of the adsorbate rises. Firstly, while the molecules within the adsorbed phase diffuse to the surface of the solid materials, a thin layer of molecules is built upon the wall of the pore. Secondly, as the concentration of the molecules increases, several monolayers (multilayer) are formed by adsorption. Lastly, capillary condensation would occur in which the pore spaces become filled with condensate, as the partial pressure required is reached. However, because the conditions on the solid surface are not uniform, the different stages may occur simultaneously in different regions of the surface materials (Coulson and Richardson, 1998). The term capillary condensation represents the transition state of the vapour-liquid, where the gas is subjected to a certain pressure P, which is less than the saturation pressureP_0, which condenses it into a liquid-like phase within a pore (Thommes et al., 2015). However, unlike larger pores, which can be described by the capillary condensation phenomenon, micropore filling does not include a vapour-liquid phase transition. Capillary condensation in pores can be described by the Kelvin-Cohan equations (Rouquerol et al., 2013):

$$ln\left(\frac{P}{P_{\circ}}\right) = -\frac{k_{\gamma} V_m \cos\theta}{RT\ (r_P - t_i)} \tag{3.1}$$

where the subscript, i, is 1 for capillary condensation and for capillary evaporation is 2, P/P_0 is the relative pressure corresponding to condensation/ evaporation takes place in a cylindrical pore of radius r_P, k is a geometry parameter and its value depends on the pore type ($k = 1$ for a cylindrical through pore; and $k = 2$ when the pore is a dead-end type, or for desorption controlled by a hemispherical meniscus, γ and V_m are the surface tension and the molar volume of the condensate, respectively, θ is the contact angle between the liquid and the wall, t_i, is the thickness of the adsorption layer, and T and R are respectively the absolute temperature and gases constant.

Gas adsorption is used to describe the void space geometry of disordered porous materials and obtain the pore size distribution. Applying a wide range of relative pressure in gas adsorption results in producing sorption isotherms which can provide valuable information of a pore structure such as pore size, surface area, porosity, and pore size distribution. In addition, the isotherm shape can indicate the mechanism which dominates within the pores during the filling and emptying processes. Since the amount of molecules adsorbed on the solid surface is a function of the pore surface area in the porous system, the internal surface area of the pores is several times larger than the external surface area of the adsorbent. According to the International Union of Pure and Applied Chemistry (IUPAC), pores can be classified, based on their sizes, into three types (Sing, 1985). These types are micropores, which have a diameter less than 2 nm, mesopores, which have a diameter ranging from 2 to 50 nm, and pores with diameters greater than 50 nm represents macropores. It is also according to the IUPAC, adsorption isotherms have been classified into six types as shown in Figure 3-1.

- A type I adsorption isotherm has a concave shape toward the relative pressure P/P_0 axis. Most of the pores are filled at the lowest relative pressure before a horizontal plateau appeared for almost all of the ranging relative pressure. This class of porous materials are such as activated carbons, molecular sieve zeolites and certain porous oxides.
- A type II isotherm initiates with concave form relative to the relative pressure axis, and the curve then has a roughly linear-like shape, and the last section is convex to the P/P_0 axis until the maximum relative pressure approaches. This isotherm shape is an indication that adsorbate progressively condenses as layers on the wall of the pore. Although multilayers adsorbed could be built simultaneously, Brunauer et al. (1938) presumed that at the point B, which is the beginning of the linear section, all the solid surface is completely covered by the monolayer of the gas adsorbed, and multilayer gas adsorbed is about to commence. This isotherm type is typical of low-porosity adsorbents having macropores. Materials such as graphitized-carbon black and silica compact powders belong to this isotherm type.
- The type III isotherm is not common, but there are certain systems, like nitrogen on polyethylene where this isotherm type, can be observed. The convex shape in this isotherm covers the whole range of relative pressure P/P_0, and, hence, no point B can be observed. The isotherm is characteristic of non-porous or macroporous materials, and the interaction between adsorbate and adsorbent is not strong (Coulson and Richardson, 1998).

- Type IV isotherms are similar to type II isotherms but are distinguished by the hysteresis loop as a characteristic feature. The hysteresis loop is associated with capillary condensation occurring in mesopores, and restricted adsorption over the range of high relative pressure (Sing, 1985). The isotherm shows the point at which monolayer coverage is complete and multilayer adsorption is beginning as in type II. Many mesoporous industrial materials produce this type of adsorption isotherm (Sing, 1985).

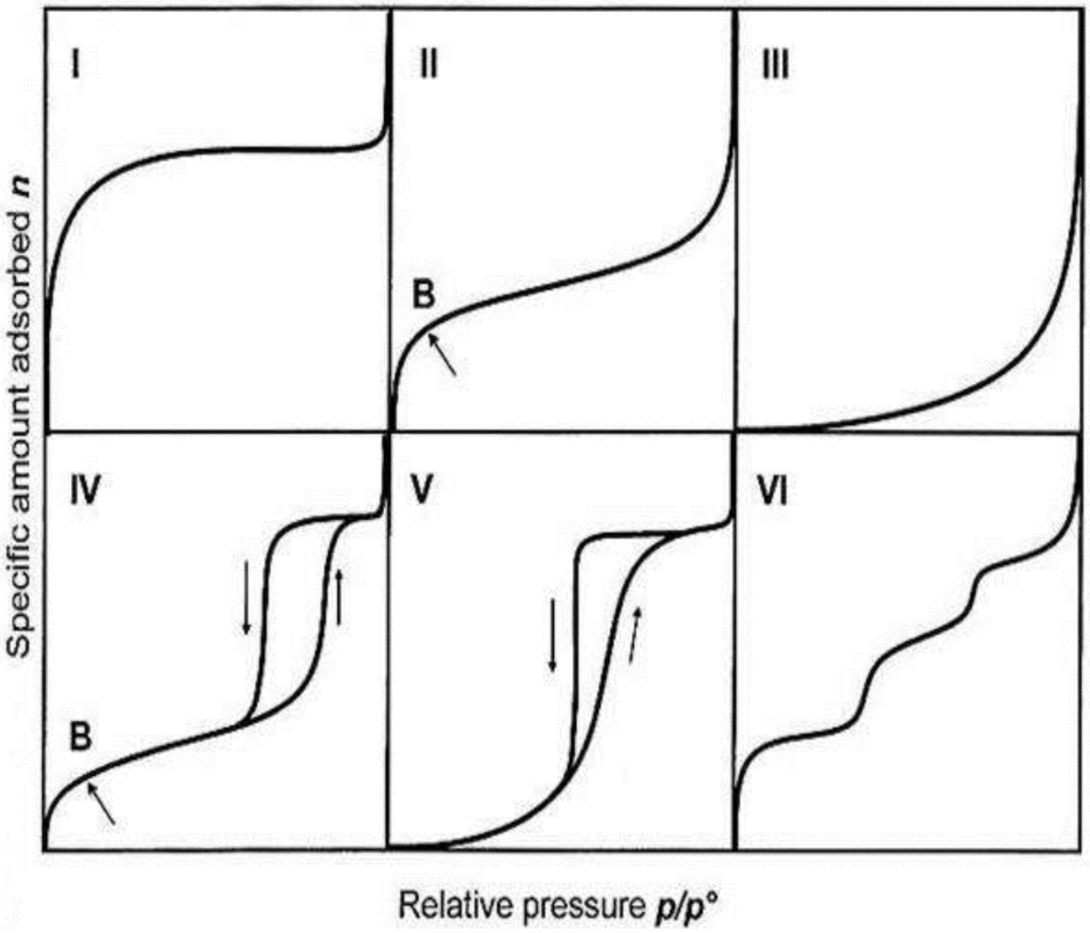

Figure 3-1: The types of adsorption isotherms, based on the IUPAC classification (Sing, 1985).

- Type V isotherms are similar to type III, it is convex to the P/P_0, but a hysteresis loop and capillary condensation are involved. It is also, the bonds connecting between the adsorbate and the solid surface are weak. Materials which have micropores or mesopores media exhibits this type of isotherm (Allen, 2013).
- A type VI adsorption isotherm comprises many steps of multilayer adsorption taking place on a uniform non-porous surface. At the end of each step, the monolayer covers all the solid surface and the beginning of a new layer to be built. This type of isotherm is typical of adsorbing argon or krypton on non- porous or macroporous materials such as graphitised-carbon black at a temperature of 77 K (liquid nitrogen temperature) (Sing, 1985).

3.2.2 Hysteresis in gas adsorption

A hysteresis phenomenon is often observed for gas adsorption, where the gas evaporation occurs at the relative pressure lower than that at which it originally condensed. In general, hysteresis loops arise during multilayer adsorption of physisorption isotherms and are associated with capillary condensation, and are widespread for most of the materials having mesopores. Many theories have been proposed to interpret the hysteresis phenomenon taking place in gas adsorption.

Foster (1932) has described the existence of hysteresis through experimental sorption isotherms of different type systems on disordered porous solid. It has been suggested that liquid condenses without delay in the system in which the pores get blocked at the narrowest points, while in those which have no dead-end pores, there is no meniscus formed until sufficient liquid is existent. During the desorption branch, the evaporation process occurs in a pore filled with liquid when the applied pressure is less than the corresponding pressure at which the condensation process occurred, and when the pore is in contact with the vapour phase. Based on the above theory, the liquid film layer held on the walls during the condensation process is in a metastable state and the capillary condensed liquid represents the true equilibrium state.

Cohan (1938) suggested that systems having through-pores must produce hysteresis even when perfect wetting has been achieved. Cohan (1938) suggested that liquid condenses in the cylindrical through pore via a cylindrical sleeve-shaped meniscus, while a hemispherical-shaped meniscus is the responsible for evaporating of the liquid on the desorption branch.

Saam and Cole (1975) offered an explanation of the hysteresis taking place in sorption isotherms that depended on the assumption that the film created along the wall of the pore is metastable. It has been suggested that the existence of different systems of stability and instability associated with metastability in a cylindrical pore leads to hysteresis. According to Saam and Cole (1975), Van der Waals forces contribute to the stability of the multilayer film created on the wall of the pore, and the gas condenses due to the capillary forces arising between the film curvature and vapour phase, as the relative pressure rises. The evaporation process of the adsorbate condensate takes place at a lower relative pressure and the film thickness will be smaller than that of the critical condensation thickness of the multilayer film, and hence, this difference in the film thickness between two cases leads to the hysteresis.

Morishige and Shikimi (1998) have investigated the temperature effect on adsorption isotherms on mesoporous materials using different pore sizes. It has been shown that as the temperature increased, the hysteresis loop became narrow, and, at the hysteresis critical temperature, it eventually disappeared. However, this temperature is affected by the average pore size, but it lies considerably beneath the pore critical temperature.

The results revealed that the adsorption hysteresis never takes place if the radius of the cylindrical pore is smaller than twice that of the molecular diameter.

Neimark et al. (2000) have studied capillary condensation hysteresis in a through pore using Monte Carlo (MC) simulations and non-local density functional theory (NLDFT). The MCM-41 model was employed for this experiment, with the assumption of neglect the pore blocking effects. It has been shown that in cylindrical pores, four regimes of sorption are recognised as the pore diameter increases, commencing from a pore-scale of 0.3-0.4 nm. The conditions these regimes work within depend on the temperature and pore diameter. It has been found that the hysteresis loop shrinks as the pore diameter reduces, and, at the critical pore size, it vanishes. It was also noticed that MC simulation and NLDFT revealed that, in the developed hysteresis regime for nitrogen sorption at 77 K, condensation takes place spontaneously at the vapour-like spinodal whereas desorption branch occurs at the equilibrium.

Thommes et al. (2006) have studied different networks of mesopores within disordered porous materials to investigate the hysteresis in pores of ink-bottle type. It has been found that the hysteresis loop is formed by different mechanisms, depending upon the geometry of the pores. The findings revealed that evaporation controlled by cavitation takes place in ink-bottle pores with a large ratio of the pore size to the neck size. In this case, the size of the neck has no effect on the evaporation pressure, and the desorption branch cannot provide information concerning the pore size distribution. While, in the smaller pore to neck size ratio, as observed in the porous Vycor glass, evaporation is controlled by percolation. In this case, the desorption branch can provide information to obtain the pore neck size.

Further experimental work has been conducted by Seaton (1991) using a model of a porous solid of different pore diameters, to investigate the effect of the pore connectivity on the sorption isotherms of disordered materials. The sorption hysteresis was analysed by employing percolation theory. The value of the pore connectivity, for porous materials giving hysteresis loops, depends on the type of the hysteresis as classified by the IUPAC. The connectivity of the pore network was obtained from the analysis of the nitrogen adsorption data. In his work Seaton (1991) has adopted a model of a small network which involves three pores in porous solid as presented in Figure 3-2. The pore sizes, starting from the smallest the pore, are in the order of A, B and C. Both pores A and C have no communication with the sample exterior while the pore B is in contact.

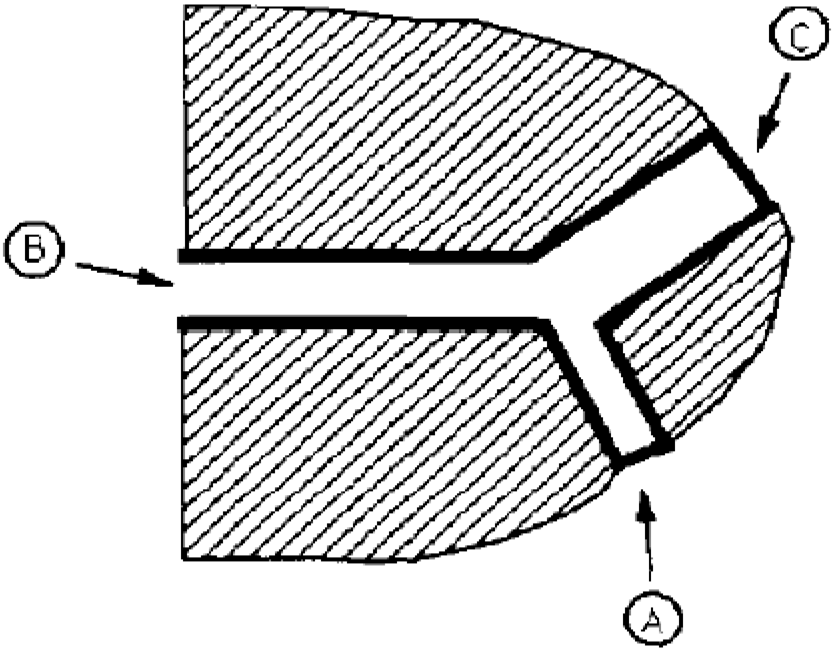

Figure 3-2: Simple model of small system pores in disordered materials (Seaton, 1991).

During the adsorption process, the nitrogen gas condenses within the smallest pore, and as the pressure increased the pores are filled with the condensed liquid in order of A, B and C. Following the adsorption stage, the desorption process should be started reversibly by evaporation of the condensed gas in the order of C, B and A. However, because there is not any connection between the liquid nitrogen in the pore C and the vapour phase, the nitrogen is incapable of evaporating at its condensation pressure. Hence, the pore B filled by liquid nitrogen, which is in contact with the vapour phase, will allow the nitrogen to vaporise, while the pore C traps the nitrogen as a metastable liquid below its condensation pressure until it obtains an access to the vapour phase. The condensed gas in pore A will then have access to the vapour phase and be able to evaporate at its condensation pressure. Therefore, the order of evaporation process starts with the pores B and C simultaneously, followed by A. The delay of evaporation occurring for the liquid nitrogen in the pore C brings about hysteresis in porous materials.

According to the IUPAC, hysteresis loops, which are obtained experimentally, have been classified into four different types, denoted H1, H2, H3 and H4 (Sing, 1985) but this scheme has been extended based on more recent results (Thommes et al., 2015). The hysteresis types have been shown schematically in Figure 3-3. Each of these different hysteresis types is formed based on a particular feature that exists in the pore structure within porous media (Thommes et al., 2015).

The hysteresis loop of type H1 is produced by materials in which the mesopores sizes are uniforms (cylindrical pores), such as in MCM-41, MCM-48 and SBA-15 materials. This type can also be observed in materials having pores of ink-bottle type where both neck and pore/cavity size, distributions have a similar width. Generally, the steep shape, which is one of the H1 features, and the narrow hysteresis loop, are an obvious indication of that the adsorption branch is dominated by delayed condensation.

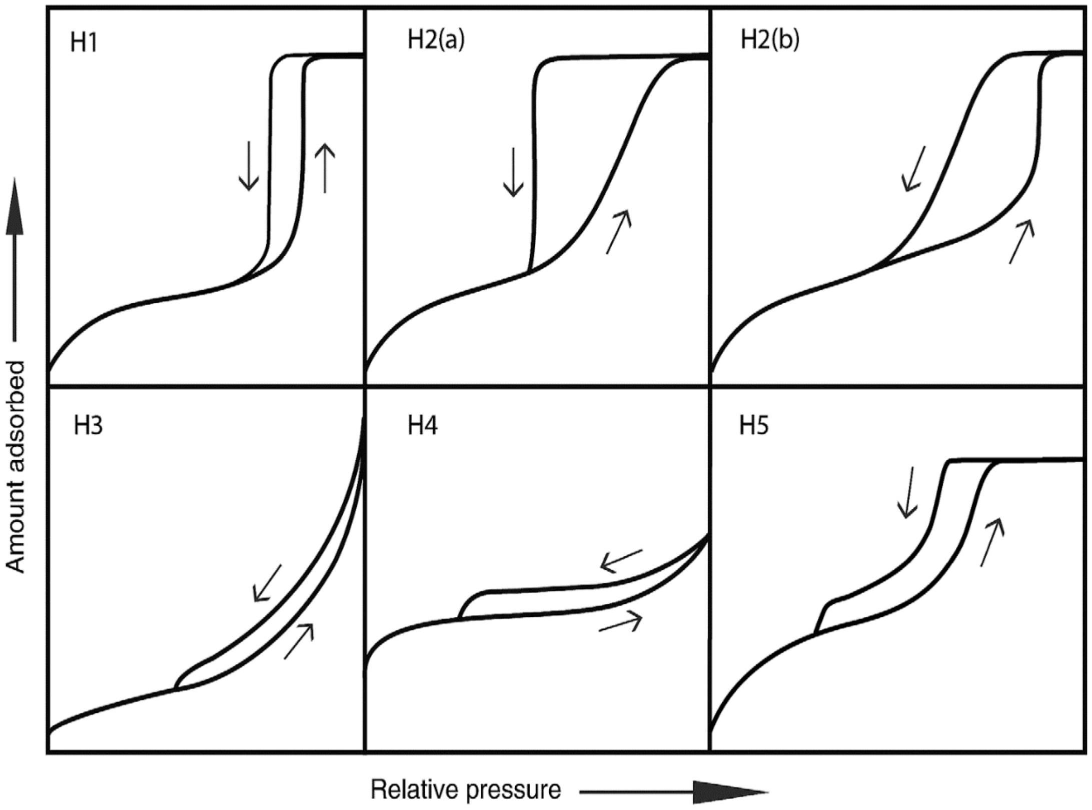

Figure 3-3: The classified types of hysteresis loops based on the IUPAC (Thommes et al., 2015).

Type H2 arises in materials having more complicated pore structure which consist of a wide range of pore sizes. The network effects have a significant role in the shape of the hysteresis (Thommes et al., 2015). The hysteresis H2a loops have a very steep desorption branch which is attributed to the dead-end pore/percolation in a narrow necks pore size distribution or the vaporisation caused by cavitation. Such materials which give this type of hysteresis are mainly silica gels, Vycor glass and some of the ordered pore structure materials such as SBA-16 and KIT-5 silica. The hysteresis loop of type H2 is also related to the pore blocking, but the width of the pore necks size distribution is much larger. This type of hysteresis can be observed in mesocellular silica foams and mesoporous silica modified by hydrothermal treatment. The types H3 and H4 are uncommon and both can arise in porous solid having slit-shaped pores. The type H5 loop has a characteristic form associated with a particular pore geometry having both open and partially blocked mesopores such as plugged hexagonal templated silica (PHTS) (Thommes et al., 2015).

3.2.3 Advanced condensation phenomenon

The advanced condensation or adsorption theory as proposed by Broekhoff and De Boer (1967) is for pore structure having pore type through-open such as in ink-bottle pore, if the pore neck diameter is less than half that of the adjacent body pore, the pores then will fill independently at different pressures as shown in Figure 3-4a.

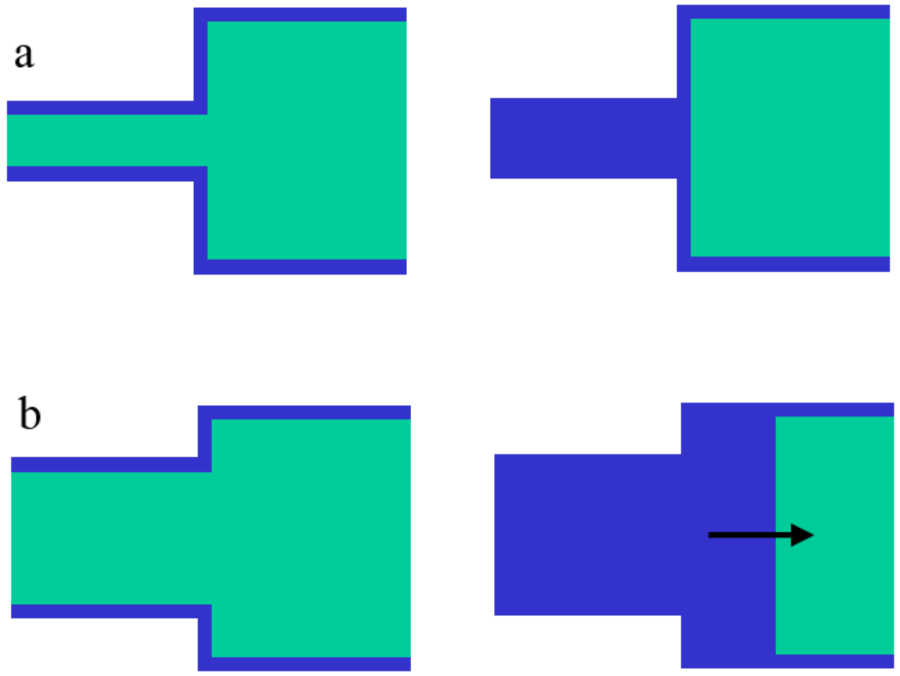

Figure 3-4: A schematic representation showing two types of the pore filling. (a) A neck diameter is less than the half of the body diameter in which the pore neck and the pore body is filled independently, (b) Where the neck diameter is higher the half of the body diameter in which the condensation within the pore body occurs following the pore neck at the pressure required exceeded by the pressure required for a cylindrical meniscus (Evbuomwan, 2009).

If the diameter of the pore neck is greater than half that of the pore body, filling the pore body will take place via a hemispherical meniscus at the pressure which will be overridden by the pressure required for condensation within the pore neck with a cylindrical-shaped meniscus (Rigby and Chigada, 2009) as stated in Figure 3-4b. Since the pore neck has been filled with condensate gas, a hemispherical-shaped meniscus is formed at the end of the pore neck at which filling of the neighbouring pore body occurs. The pressure, in this case, is identical to that proposed by the Cohan (1938) equation for a cylindrical sleeve-shaped meniscus in the pore neck. Therefore, the ratio of the pore neck to the pore body plays a crucial role in identifying the domain mechanism of the filling and emptying within the ink-bottle pore. Coke formation can occur in the pore neck or the pore body resulting in a change in this ratio. Thus, in the existence of the advanced condensation, the mechanism would be changed as the pore neck diameter reduced to less than half that of the non-coked pore body.

Experimental scanning curves can be obtained for disordered materials to derive more detail about the void space geometry (Hitchcock et al., 2014b). Hitchcock et al. (2014b) have utilised a novel integrated gas adsorption and mercury intrusion on ink-bottle pores, to determine which specific mechanism is taking place when scanning branches cross between the boundary curves. It has been shown that both the effects of advanced condensation and pore blocking can be found when scanning curves cross from and to the boundary curve during a desorption process. This process is clarified using the pore structural model as Presented in Figure 3-5.

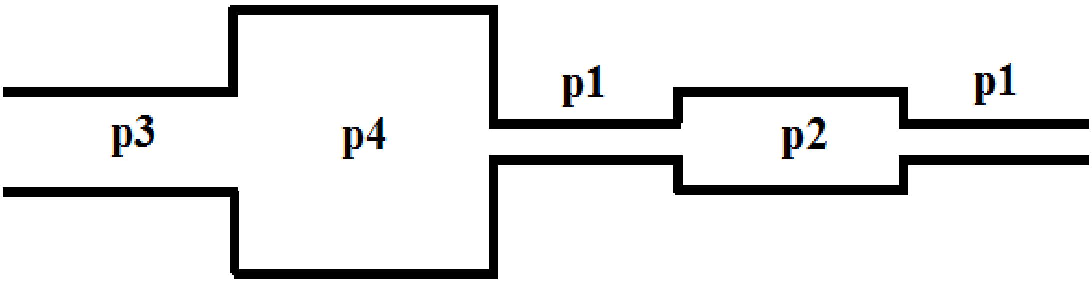

Figure 3-5: A structural model with different type of pore made up in the order of p4 > p3 > p2 > p1 (Hitchcock et al., 2014b).

The pore model consists of four various diameters which are arranged in the order of p4 > p3 > p2 > p1, while keeping the domains with the same void volume. It is assumed that a communication between the various pores is available, and the fluid acts in the pores in the following way. As the fluid condenses in pore p1, a hemispherical-shaped meniscus is then formed at the end of the neighbouring pore p2 allowing the pore to be filled with the fluid, following the mechanism of advanced condensation. Because of the relatively larger size variances of the nearest adjacent pores, the filling in the pores p3 and p4 occurs independently, and, thereby, the advanced condensation mechanism will not dominate. During the desorption process, p4 is influenced by the pore-blocking effect, and, hence, it empty only when p3 is empty of condensate, and the liquid in p2 can evaporate only if the liquid in p1 evaporates.

3.3 Mercury porosimetry

The characterisation of the internal geometry of the porous materials plays a crucial role in the development of the catalyst used in the different industrial processes such as that applied in the engineering operations and enhanced oil recovery, where the fluid transportation within the pore is directly affected by the properties of the void space structure. A wide range of various techniques employed to investigate the porous structures. Mercury porosimetry is commonly the most used technique to describe the pore geometry of macropores (pore sizes > 50 nm) and mesopores (pore sizes of 2-50 nm). In general, mercury intrusion can be applied to determine the particular surface area, porosity, pore connectivity, pore volume and the volume pore size distribution (Portsmouth and Gladden, 1992, Rigby et al., 2003a).

3.3.1 Theory and Background

The theory of mercury porosimetry is based on the basic physical principle that mercury acts as a non- wetting fluid toward most disordered materials, and, hence, an extremely hydrostatic pressure is required to allow mercury penetrating into the pores of the porous materials. As the pore size decreases, a higher pressure is required to force mercury into the pores. Typically, mercury porosimetry data is analysed using the modified Young-Laplace equation which is called Washburn (1921) equation. The Washburn equation assumes that the pore structure is composed of long, regular cylinders as standard (Rigby et al., 2011). The relationship between the applied pressure and the pore size is generally expressed by the Washburn equation:

$$P = -\frac{2\gamma \, cos\, \theta}{r}, \tag{3.2}$$

where: p = the applied pressure at which mercury penetrates the pore (MPa).

$\gamma =$ the mercury surface tension (0.485 Nm^{-1}).

$\theta =$ the mercury contact angle.

r = the pore radius (m).

The volume of mercury entrapped in the pore is obtained directly as a function of the imposed pressure. When raw data of mercury porosimetry is analysed by this equation, it is assumed that the factors γ and θ are kept constant. Several studies have been discussed by many authors in which it is found that the values of interfacial tension and the contact angle are affected by some parameters such as pore size (Kloubek, 1981, Allen, 2013), the solid surface nature (Van Brakel et al., 1981), or whether the mercury is intrusion or extrusion (Rigby et al., 2003a). Moreover, during the intrusion process, the pore diameter measured by the Washburn equation related to the entry size of the pore. In contrast, the diameter of the pore body, rather than the pore neck, can be determined from the information obtained from the extrusion process depending on their ratio. Mercury porosimetry suffers from what is known as the pore shadowing or shielding effect. This occurs when the void space has ink-bottle type pores where larger pore bodies are only accessed by smaller pore necks. Hence, mercury intrusion curves can only give the pore neck size since the intrusion pressure must be raised to that required to enter the neck before the body will also be filled. Therefore, all the pores look like they are of the neck size, and the distribution is skewed towards smaller pore sizes (Mathews et al., 1997). However, mercury porosimetry in ink-bottle pore systems is also usually characterised by entrapment where mercury gets stuck in the larger pore bodies because the meniscus breaks off at the boundary with the neck as the mercury tries to leave the neck. As a consequence, the larger pore size becomes skewed to smaller pore size. Further, the pore size distribution can be influenced by the equilibrium time, which is the delay time allowed before the mercury pressure is increased (Gopinathan, 2012). When the equilibrium time is short during mercury entrapment, the distribution will be skewed to size and volume of the pore lower than the real one because that the mercury menisci do not have enough time to detect the existence of pores. Therefore, the amount of the entrapped mercury increases as the provided time is not enough for the extrusion process.

Unlike, the ideal cylindrical pore, in the real pore, mercury will intrude at a pressure different from that at which the mercury will extrude. These differences in the pressure give rise to hysteresis phenomenon between the intrusion and extrusion branches.

From the shape of hysteresis, it can be obviously seen that a larger amount of mercury left within the void space than corresponding to that intruded amount at the same imposed pressure. Several various theories have been suggested to describe this phenomenon, including hysteresis caused by contact angle (Van Brakel et al., 1981), a pore potential effect, or the required energy to create a meniscus at the beginning of extrusion (Giesche, 2006). The first-time hysteresis was realised by Ritter and Drake and Ritter (1945) on the mercury porosimetry isotherms when the applied pressure is incremented following mercury intrusion. In general, the hysteresis can arise from either, or both of, contact angle and structural hysteresis (Van Brakel et al., 1981).

Contact angle hysteresis**:** The difference in the contact angle between the mercury and the solid surface in both the intrusion and the extrusion result in occurrence such this type of hysteresis, and, hence, the retraction branch acts different way from that what the advancing branch follows. Extensive work has been carried out on two samples to determine the hysteresis in mercury porosimetry using correct retraction wetting angles (Lowell and Shields, 1981b). It has been found that how the extrusion curve, for the tested samples, coincided with second or subsequent intrusion branches through the whole pore radius range, and suggested that the extrusion contact angle is different from the contact angle for the intrusion. As a result, the presence of the hysteresis is attributed to this difference in the contact angle between advancing (intrusion) and receding (extrusion) branches. Liabastre and Orr (1978) have employed controlled pore glasses (CPG) to study the structure of a porous model with regular pores of a uniform size using an electron microscopy and mercury intrusion experiment. These researchers obtained values for the glass pores diameters by direct observation from microscopy. They made a comparison between these values and those obtained from mercury experiment via Equation 3.2, assuming that contact angle and surface tension have constant values. Based on the data derived by Liabastre and Orr (1978), Kloubek (1981) has found a practical expression that obtains the variance of the factors $\gamma \cos\, \theta$ as a function of the pore size for both intrusion and extrusion branches. The expression

$$\gamma \cos\, \theta_A = -\, 302.533 + \frac{-\, 0.739}{r} \tag{3.3}$$

for the variation of the parameters $\gamma \cos\, \theta$ for an advancing meniscus, which can be valid for pore sizes in the range 6-99.75 nm, and the expression

$$\gamma \cos\, \theta_R = -\, 68.366 + \frac{-\, 235.561}{r} \tag{3.4}$$

for a retreating meniscus, which can be valid for pore sizes range from 4 to 68.5 nm. Rigby and Edler (2002) have derived a relationship to calculate the pore radius for mercury intrusion and extrusion, as a function of the imposed pressure via inserting Equation 3.3, or Equation 3.4 into the Washburn equation and solving for r. The pore radius for mercury intrusion is computed by

$$r = \frac{302.533+\sqrt{91526.216+1.478\, p}}{p} \tag{3.5}$$

while for mercury extrusion the relationship becomes

$$r = \frac{68.366+\sqrt{4673.91+471.122\, p}}{p} \tag{3.6}$$

These equations, in spite of their complexity compared to the Washburn equation commonly applied for this purpose, have an advantage that they, in addition, take into consideration the differences occurring between the contact angle and the surface tension as the curvature radius of the fluid at the meniscus is reduced (Rigby and Edler, 2002). Since the correlations for the product $\gamma \cos\theta$ are practical in origin, then the pore sizes obtained from different methods will not be accurate, hence, their use results in an experimental error in the measurement of the pore sizes which is approximated (Kloubek, 1981) to be ~ 4-5% (Rigby et al., 2008a). These expressions have been validated by Rigby et al. (2006a) using integrated gas adsorption and mercury intrusion.

Rigby and Edler (2002) have been employed the semi-empirical forms of equation 3.2 to analyse the data raw obtained from the mercury intrusion/retraction experiment for many different types of mesoporous materials, such as sol-gel silica spheres to obtain pore sizes as absolute values instead of relative values. They have compared the analysis findings with the results of the pore sizes measured by Small Angle X-ray Scattering (SAXS), and a Barrett-Joyner-Halenda (BJH) experiment of the nitrogen sorption isotherms. The results of the analysis have suggested that mercury entrapment is obtained by the pore with macroscopic, and not microscopic structures.

***Structural hysteresis*:** This type of hysteresis can be observed in most disordered materials, and, the nature of the pore geometry can cause this form of hysteresis (Van Brakel et al., 1981, Levitz, 2002). The extrusion behaviour is strongly influenced by the pore structure, where a cylindrical-shaped pore with one-end closed does not have a real effect on the behaviour of the data intrusion. However, extrusion would occur at a lower pressure in this type of pore, compared to a cylindrical through-pore (Levitz, 2002). The Ink-bottle theory provides a sensible explanation for this hysteresis, which refers to narrow connections void spaces between large cavities of neighbouring pores (Van Brakel et al., 1981, Lowell and Shields, 1981a). The system of ink-bottle consists of small pores connected to larger neighbouring void spaces as shown in Figure 3-6, where a structure of ink-bottle is formed via adjoining pores.

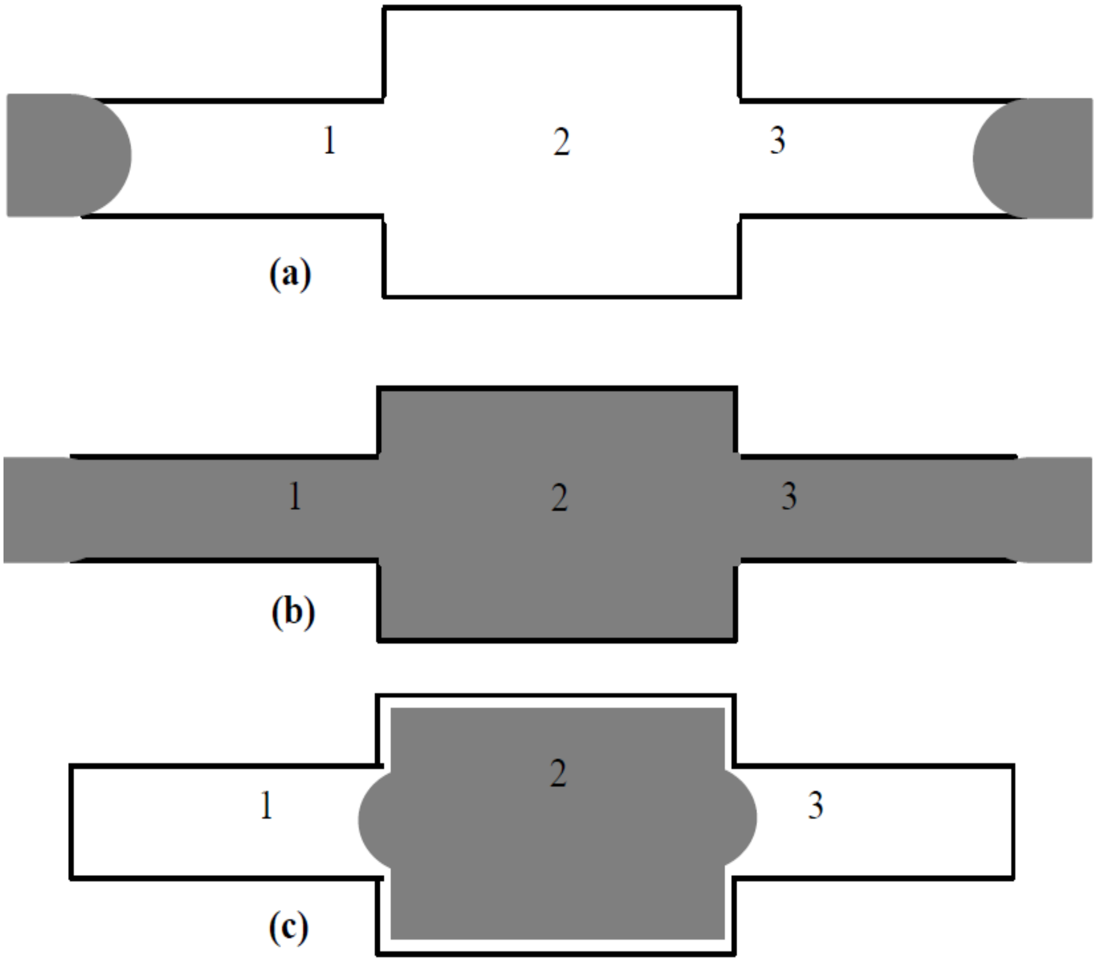

Figure 3-6: Ink-bottle system with different pore sizes intruded by mercury (Dim, 2015).

The size of the pore entrance determines the pressure required for mercury to be entrapped into the pores within disordered solids. Once the imposed pressure increases, the mercury will be allowed to intrude pores 1, 2 and 3. As the pressure is subsequently reduced, mercury withdrew initially from pores 1 and 3 resulting in disconnecting the mercury by the snap-off effect. Hence, an extensive residual mercury is retained in the larger adjacent pore as shown in Figure 3-6c. The dark areas refer to the pores filled with mercury, and, as the pressure declined mercury extruded partially by confined to disconnect blobs.

Furthermore, Rigby and Chigada (2009) have combined MF-DFT simulations with experimental work to demonstrate the cause of the hysteresis width in silica materials. The study was performed on silica samples with different degrees of surface roughness. It has been found that the width of the hysteresis for silica materials depends on the roughness degree of the surface, where the width of the hysteresis decreased when the surface roughness factor increased.

Mercury intrusion simulation has been carried out by Matthews et al. (1995), to test random network structures and correlation structures in which different body pore and throat pore sizes were employed. The findings revealed that the shape of hysteresis can be affected by the nature of the pore geometry but cannot predict solely the properties of the correlation levels. It was found that clusters of small pores surrounded by larger clusters of pores produced more gradual mercury intrusion isotherms, compared to that for random networks. However, the mercury intrusion curves were very steep for a system having clusters of large pores surrounded by small pore clusters.

Moreover, Wardlaw and McKellar (1981) have performed mercury intrusion porosimetry on microscale models involving different sizes of pores etched in glass. Two micromodels have been employed in this study as presented in Figure 3-7. In the first model, the pore network was arranged in a regular system, where isolated clusters of smaller pores occur in a continuous network of isolated larger elements. Once the applied pressure is increased, the larger elements preferentially filled with mercury.

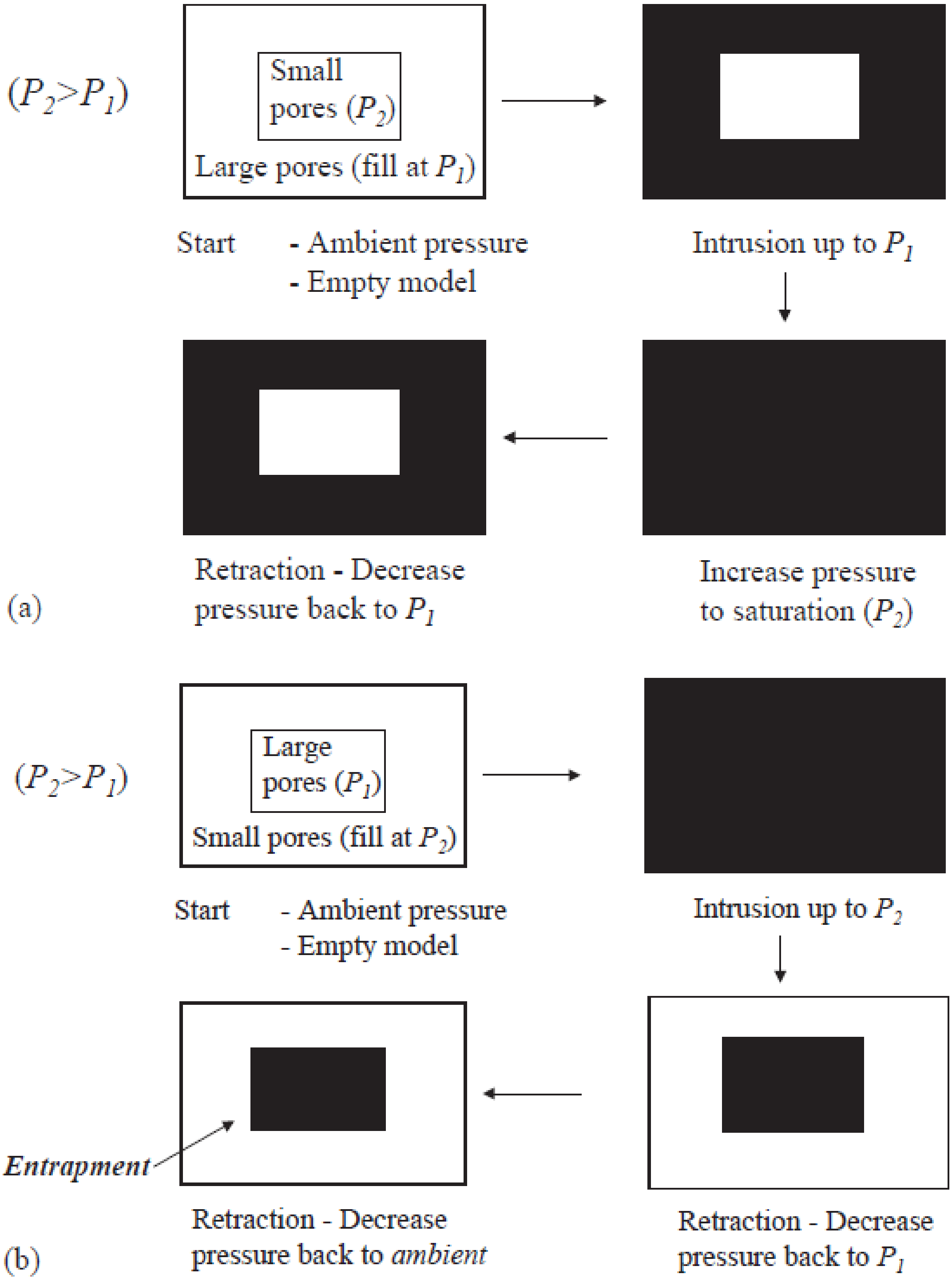

Figure 3-7: A graphical scheme showing the residual mercury after mercury porosimetry obtained by Wardlaw and McKellar (1981) (Rigby et al., 2004b).

As the pressure further increases, mercury intrudes all the empty model to be saturated with it. When the pressure is then subsequently decreased, mercury first extrudes from the smaller clusters. With a further decrease in the imposed pressure, the mercury withdrawal from the rest of the system then occurs. In the second micromodel, in which clusters of large pore elements surrounded by smaller pores network, the imposed pressure needs to be increased to the value at which the mercury is allowed to enter the smaller pores. As the mercury entraps the structure it becomes saturated. Once the mercury pressure is then reduced, the mercury first retracts from only the smaller pore clusters. However, at the point where pressure has been declined below the threshold for the emptying of the larger pore clusters, these have already become disconnected by snap-off and extensive remaining mercury is intruded. Wardlaw and McKellar (1981) have concluded that the amount of the residual mercury during extrusion from a pore network is generally affected by four aspects as follows:

- ***Pore to throat size ratio*:** The amount of the mercury entrapped in pores increases when the ratio of the body pore to the throat size increases. Therefore, in the system having large pore to pore neck ratio within porous media extensive residual of mercury will be entrapped.
- ***Throat to pore coordination number*:** The average number of the throats which have a connection with each other represents the coordination number of a pore system. Based on the results obtained from their work, the amount of the residual non-wetting phase reduces once the coordination number of the pore system increases.
- ***Random and non-random heterogeneity*:** As described above, the amount of the mercury entrapment within these types of micromodels is sensitive to the existence of non-random heterogeneity.
- ***Surface roughness*:** Rock pores in the reservoir have a wide range of a surface roughness which defers extremely from the smooth crystal surfaces such as in some dolomites to the generally pitted or clay coated surfaces of many sandstones. The

surface roughness of the materials affects the contact angles of the mercury through intrusion and extrusion processes.

3.4 Differential scanning calorimetry (DSC)

Thermoporometry, also named thermoporosimetry, is a characterisation technique that measures pore size based on the depression of the melting or freezing point of the liquid entrapped in a pore (Brun et al., 1977). In general, the phase transition point for pore freezing, with respect to the bulk, changes inversely with crystal diameter (Mitchell et al., 2008). This technique is simple and uncomplicated to use, and this feature is considered the main advantage for DSC. In addition, preparation of the sample in the thermoporometry experiment does not need special requirements (Bafarawa, 2015).

3.4.1 Theory and Background

The basic principle of the method is based on the detection of the temperature shift in the phase transition for a liquid confined in pores within disordered solids. Significant information, regarding the pore structure, can be obtained from this difference in the phase transition to determine pore size and its distribution. The size of the blob that makes the transition is proportional to the heat dissipated at the corresponding temperature. This means that the peaks observed during the melting or the freezing of the entrapped fluid are typically related to the size of the pore, and, thereby the pore structure (Beurroies et al., 2004). Defay et al. (1966) have developed a thermodynamic characterisation to measure the depression of the equilibrium temperature between all component phases in a porous network with curved interfaces. Further, an experimental work has been conducted by Brun et al. (1977) to study thermodynamically the liquid-solid phase transitions in porous disordered materials.

This study carried out based on the relations between the size of the pores in which a frozen process occurs and the triple point temperature, to determine the pore size distribution of the frozen liquid inside the pores of a porous solid. Therefore, allowing the solidification and melting of material entrapped on the pores to be observed as a function of temperature. When a frozen liquid is melting within a cylindrical pore, and, according to the Gibbs-Thompson equation, the value of the melting point depression ΔT_m is expressed by the form (Dim, 2015):

$$\Delta T_m = T_o - T_m = -\frac{2\gamma_{ls}\,\nu\,T_o}{\Delta H_f\,d} \tag{3.7}$$

where T_o is the melting temperature of the bulk, T_m is the melting point in a pore of diameter d, γ_{ls} is the interface tension of the liquid-solid surface of the probe fluid, ν is the molar volume, ΔH_f is the bulk enthalpy of melting. This equation is often written in a simplified form:

$$\Delta T_m = k/\,d, \tag{3.8}$$

where k represents the Gibbs-Thompson constant. Bafarawa et al. (2014) have conducted a thermoporometry experiment on entrapped mercury to obtain the pore size for sol-gel silica. The findings have shown that the value of the Gibbs–Thomson parameter k is 90 nm K for freezing/thawing via a hemispherical meniscus. Hence, pore sizes can be measured by the temperature at which a solid crystal melts, and, from the heat flow on melting, the volume of such pores can be obtained.

The thermoporosimetry technique has been applied, by many researchers, to the characterisation of several different disordered porous materials such as silica gel (Ishikiriyama et al., 1995, Bafarawa et al., 2014), ordered mesoporous solids

(Kloetstra et al., 1995, Schreiber et al., 2001, Yamamoto et al., 2005), porous silicon (PS) (Faivre et al., 1999), polymer gels (Baba et al., 1999, Baba et al., 2003), cellulose (Luukkonen et al., 2001), controlled pore glass (CPG) (Landry, 2005, Bafarawa et al., 2014), mortar (Sun and Scherer, 2010) and catalysts (Dim et al., 2015). Furthermore, in the thermoporometry technique, several different materials can be used as a probe liquid to investigate porous properties. These materials include such as alkanes (Ehrburger-Dolle et al., 1990, Baba et al., 2003), acetone (Iza et al., 2000, Nedelec et al., 2006), benzene (Brun et al., 1977, Yamamoto et al., 2005), water (Hay and Laity, 2000, Landry, 2005, Dim et al., 2015) and mercury (Bafarawa et al., 2014, Dim, 2015). However, the most common probe fluid used among these materials is water, which is considered non-risky, easy to use and readily accessible. Water is also characterised by a high melting enthalpy of fusion ΔH_f = 334 J/g. This feature could make the DSC technique more sensitive to small volumes of adsorbed probe liquid (Landry, 2005). Moreover, water can get readily stuck on the pore surface of the hydrophilic materials and does not lead to any of contamination (Riikonen et al., 2011).

The thermoporometry technique has the main advantage that it is simple to use and its determinations are unambiguously and quickly performed, plus its calculations are uncomplicated. Additionally, no complicated procedure is needed for the sample to be prepared and a small amount of sample is required. Furthermore, this method gives the real size of the pores, instead of giving the pore neck size or the size of the cavity. It can be conducted on non-rigid porous materials and it can be employed to determine the porous of different resins within disordered materials (Quinson et al., 1987).

Although many advantages have been noticed, this technique involves several drawbacks, the major disadvantages in using DSC related to the phase transition that the tested sample needs to be heated or cooled to measuring a dynamic process of solidification or thawing, and, thereby the temperature resolution is reduced. Therefore, the equilibrium state in the sample will not be achieved during a typical measurement. It is also considering a non-conventional method, and it is unlike the gas sorption and mercury porosimetry, which is limited use (Landry, 2005).

In general, the pore size distributions obtained from mercury porosimetry technique is inaccurate due to the phenomenon known as ‘‘shielding’’ effect. This effect appears in materials having a large pore size through due to the percolation phenomenon of this method (Rigby and Gladden, 2000). Therefore, in this study, the entrapped mercury obtained from the mercury intrusion experiment was used as a probe liquid in the DSC experiment to investigate the size of the large body pore in the ink-bottle model. The DSC provides the measurement of the blob size of the liquid, and that is typically the size of the large pore body of the ink bottle pore. Hence, the DSC has the capability to see if the pore shielding effect is causing skewing of the porosimetry pore size to smaller sizes, and if so what is the size of the bodies have been missed.

3.5 Computerised X-ray tomography (CXT)

Computer X-ray tomography (CXT) is an imaging technique by which a three-dimensional (3D) description could be obtained that can characterise microstructure, flaws and damage in the interior geometry of ambiguous porous solids with microscale resolution (Connolly et al., 2006, Ruiz de Argandoña et al., 2009). The pore spaces imaged by CXT, using synchrotron radiation, can attain ~50-100 nm resolution (Rigby et al., 2011). This technique is a non-destructive method, and it is commonly applied in Materials Science as the relation between the properties of the macroscale structure and the microscopic structure of a material is very regularly required (Salvo et al., 2003). CXT has been employed for the characterisation of Al-alloys for ~40 years. The main application of CXT was the detection of the void spaces and cracks in light materials to prove the validity of industrialization operations like die casting (Kastner et al., 2011). The CXT is commonly used in different industrial branches (Salvo et al., 2003), particularly in the automotive industry where light materials are employed. Another application of CXT is used to characterise 3 dimension image of cellular materials. This image allows a perfect description of the internal structure of these cellular materials (Kastner et al., 2011).

3.5.1 Theory and Background

In general, computerised X-ray tomography is often used to describe internal geometry and fluid behaviour through reservoir material systems. In recent years, more interest has been paid to gaining high-resolution 3D images of rock geometry and characterisation at void space level to obtain a description of multiphase transport within the reservoir (Coles et al., 1998), uses a combination of micro X-ray and tomographical algorithms which are based on the measuring of the reduction in the intensity of the X-ray light transmitted through the material (Mousavi et al., 2005). This reduction is characterised by Beer’s law, also known as Beer-Lambert law, in which the decline in the density is described as a function of the X-ray energy, length of the light track, and the linear attenuation coefficient of the material (Dim, 2015). Figure 3-8 illustrates the principle of computerised X-ray tomography, which consists mainly of the X-ray source, sample holder and detector. The sample is attached to the sample holder using a type of epoxy to fix it, and it is then centred to be between the light source and the detector. The X-ray beams are transmitted through a specimen which is rotated in many different orientations to obtain images at various angles between 0 and 360°, in which differences in intensity would be presented at thousands of points in the multiple 2D slices produced (Rigby et al., 2011). Burch (2002) has used X-ray computed tomography to describe the quantities non-destructive measurement of intensity differences in materials. It was found that the cross-sectional images obtained from the CXT are true, and the imaged component geometry was accurately shown in the cross-section plane.

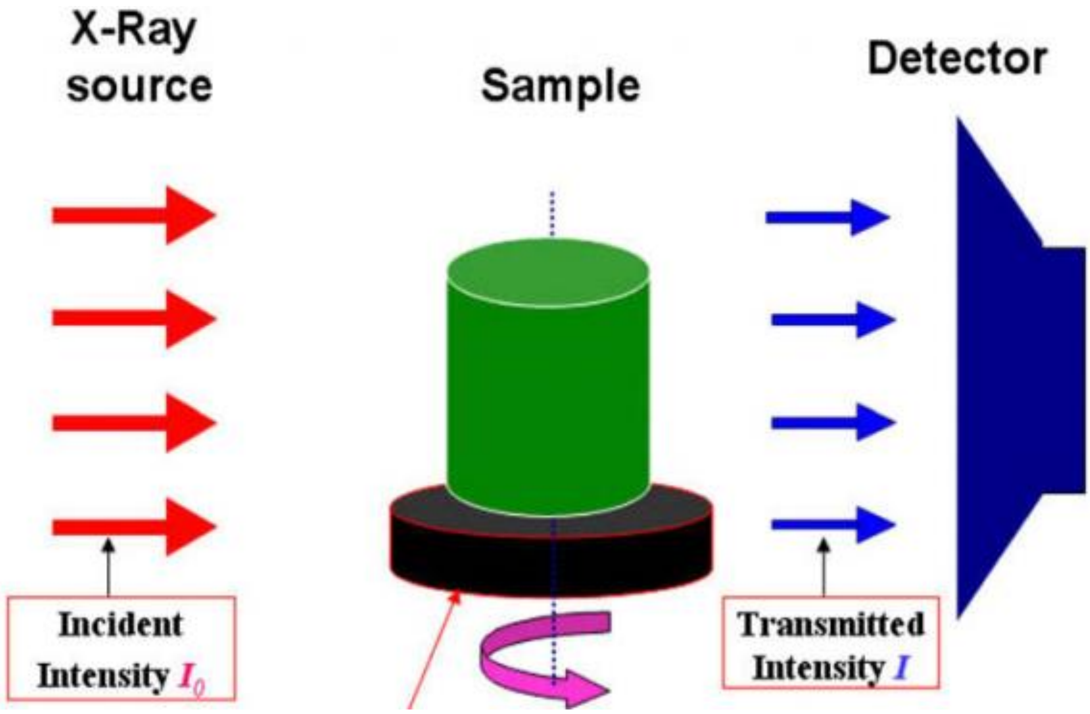

Figure 3-8: A schematic diagram showing the basic principle of CXT (Miguélez-Morán et al., 2009).

Once the specimen is subjected to the X-ray beam, the material itself will be a source of secondary X-radiations and electrons. As a result of these secondary sources, some of the primary X-ray photons are absorbed or transmitted through the sample. A linear imaging apparatus allows the transmitted densities to be detected along this beam, which is related to the integral attenuation of the difference materials performed inside the examined object (Douarche et al., 2001). For each individual sensitive pixel of the detector, the Beer-Lambert law is used to compute the intensity as follow:

$$I= I_o \times \exp\left(- \int_{x_o}^{x_1} \mu_a(x)dx \right) \tag{3.9}$$

Where I is the beam intensity during a material absorber of thickness x, I_o is the scattered intensity of the X-ray beam and $\mu_a(x)$ is attenuation coefficient of the scanned materials as a function of x-axis along the X-ray beam.

The coefficient value of the linear attenuation μ_a, is affected by the coefficient value of the mass attenuation and mass density (Rigby et al., 2011). The linear attenuation coefficient is also dependent on the photon energy (Videla et al., 2007). Moreover, the heterogeneity of the scanned material, and the use of various materials within a system, has an effect on the ultimate value of μ_a. Therefore, the linear attenuation coefficient μ_a can be obtained from the following relationship (Rigby et al., 2011).

$$\mu_a = \rho \frac{Z}{A} N_{AV} \left(a + b\frac{Z^{3.8}}{E^{3.2}}\right) \tag{3.10}$$

Where ρ is the density of the material, Z is the effective atomic number, A is the atomic weight, N_{AV} is the Avogadro's number, a and b are constant and E is the energy of the photon.

Several researchers have employed X-ray tomography to study and analyse the fluid behaviour and the transportation properties in porous media within disordered materials. Oil reservoir rocks have a great variety of pore spaces, which represent the internal geometry of the rocks, as discussed earlier in section 2.5. The X-ray tomography can provide a clear picture of the internal structure of the porous system.

Rigby et al. (2006) have integrated computerised X-ray tomography with magnetic resonance imaging (MRI) to investigate the entrapment of non-wetting fluid in nanoscale porous media in the material type of sol-gel silica. It has been revealed that the interaction occurring between the macroporous structure of the material and the microscopic mechanism of mercury snap-off leads to arising the spatial distribution of entrapped mercury in this particular material type.

Fusi and Martinez-Martinez (2013) have studied the architectural and the textural characteristics of low porosity enormous carbonate rocks using mercury porosimetry integrated with X-ray tomography. Many various carbonate lithologies have been investigated in their study. Following mercury intrusion porosimetry, the porous system entrapped by mercury has been imaged by micro CT. The high difference in the densities of the mercury and the rock makes the micro-CT scanning following the mercury entrapment very effective to detect the structural and the textural characteristics in low porosity enormous carbonate rocks.

In this project, computerised X-ray tomography, associated with mercury intrusion porosimetry, will be applied to detect the internal structure of a silica-alumina catalyst. The mercury intrusion/retraction experiment followed by X-ray imaging could provide obvious insights into the geometry of the catalyst void spaces. Furthermore, the CXT images can show in which porous scale the mercury has stuck, and, also any damage in the pellet structure caused by entrapped mercury can be observed.

3.6 NMR cryoporometry

Cryoporometry is a technique predominantly used to determine the size of the pore and its distribution for disordered porous materials. It is also known as thermoporometry, which is based on the depression of the solidification/melting points of a liquid confined within pore spaces in porous solid (Shiko et al., 2012). A liquid adsorbed in very small pore can act different from its behaviour in the bulk structure

(Awschalom and Warnock, 1987), where it melts at a temperature lower than that of the bulk solid, and the amount of this depression in the temperature is inversely proportional to the pore size. In particular, NMR is appropriate to detecting freezing phenomena. The high difference in the value of the relaxation time of water when it becomes crystal leads to only the signal of the non-frozen confined water within pores can be observed. Through gradual cooling of the sample, this signal can reveal how much of the adsorbed water within pores is frozen at a corresponding temperature (Overloop and Vangerven, 1993). Benzene, cyclohexane and water fluids are commonly used in cryoporometry to probe the size of the pore (Perkins et al., 2008).

3.6.1 Theory and background

Generally, the basic principle of NMR cryoporometry is the same basis of DSC thermoporometry (Mitchell et al., 2008). However, in NMR cryoporometry, the reduction in the signal intensity of NMR detects the volume of liquid which partially melts within pores corresponding to a wholly molten sample (Perkins et al., 2008). In a NMR technique, the large differences in the relaxation time, produced by the NMR spin-spin, can recognize the solid and liquid phases.

Like gas adsorption and mercury intrusion experiments, NMR cryoporometry is also involved hysteresis effects (Perkins et al., 2008). In general, the freezing and the melting curves in NMR cryoporometry do not overlap each other. Two different mechanisms have been suggested to interpret how freezing process occurs (Alexey et al., 2007). The first mechanism is that when the confined liquid within the pore is in contact with the bulk liquid which is already frozen, freezing may occur through advancing of the crystallization front from the pore through-open across the centre of the pore. If the cylindrical pore is empty of any obstacles, such as ink-bottle or pore throats, the system will then be stable and the temperature at which the freezing occurs will be equal to the equilibrium temperature. On the other hand, when the propagation front is prevented by obstacles, the system will be then entrapped in a metastable state until the temperature is reached below a critical value of the freezing temperature (Petrov and Furó, 2009). The second case of metastability is performed if the imbibed probe liquid in the pores is not frozen. In this case, the probe fluid requires to lowering the temperature below the equilibrium temperature to initiate freezing by nucleation. This nucleation could be homogeneous or heterogeneous, and in both cases, the value of the freezing temperature depends on any effect that can be associated with the confinement process initiated by nucleation in the pores whether this nucleation is homogeneous or heterogeneous (Petrov and Furó, 2009).

Several previous studies have tested NMR cryoporometry scanning loops. In an early study, NMR cryoporometry technique has been employed by Allen et al. (1998) using water and cyclohexane as probe fluids in disordered porous silica to characterise pore size of 6 nm. A high spin echo T_2 was utilised in this technique with filling fractional saturation in the range of 0.1 to 1.0. The findings showed how the surface properties affect the behaviours of the fluids within pores. It has been found that in the case of cyclohexane (a non-wetting fluid), no puddles have been formed within pores at low filling fractions but pores were entirely filled with condensate in the order of the smallest pore to the largest one. On the other hand, the curves of the puddle size distribution for water (a fluid which wets the solid surface) detected small sizes of puddles were formed at low filling fractions, which are much smaller than the size of the smallest pores. The finding of the pore size distribution obtained from water is more accurate than that obtained from cyclohexane.

Hitchcock et al. (2011) have investigated freezing-melting hysteresis in NMR cryoporometry for mesoporous materials using scanning curves experiments together with the data obtained from NMR diffusometry and relaxometry. They claimed that melting curves of NMR cryoporometry are extremely affected by pore-pore cooperative corresponding to the effect of the advanced condensation presented in gas adsorption. Melting, for a cylindrical pore, is commenced from the thin unfrozen liquid layer that present at the wall in a radial direction towards the interior of the pore. It is also found that pore size distributions, obtained from cryoporometry melting curves conducted for mesoporous silica material, is suffering from a dramatic deviation towards smaller pores due to the effect of the advanced melting.

By integrated NMR cryoporometry and gas adsorption, Shiko et al. (2012) have demonstrated the effect of the advanced melting in a mesoporous silica that has different condensate volumes with various fractional saturation. It has been illustrated that NMR cryoporometry has successfully distinguished that the commencement of the advanced melting is related to the increase of the volumes of condensate. It is also that the results have detected the pore in which the process of a significantly advanced melting can be noticed, where the condensate fluid has filled large pores before smaller pores.

In the present research, the NMR cryoporometry technique is employed to shaly disordered porous materials using water as a probe fluid. Scanning loop experiments to investigate the freezing-melting process in silica and silica-alumina catalysts. The NMR cryoporometry technique can determine the effect of the delayed condensation on the accuracy of the pore size distribution, and then make a comparison the results with that obtained from the other techniques.

CHAPTER 4

SILICA CATALYST

4.1 Introduction

Gas Sorption is still a very common experimental method used to obtain pore size distributions (PSD) for porous materials. The PSD is the most important parameter to describe the void space structure for porous solids, that is used to develop heterogeneous catalyst pellets, and understand their properties such as activity and selectivity. Hence, the accuracy of the PSD measurement is essential. The gas sorption and mercury intrusion experiments are indirect methods. Therefore, gas adsorption can be integrated with mercury porosimetry to obtain more accurate pore-size distributions for some materials.

Many studies have recently investigated using different tomographic methods, such as dual beam scanning electron microscopy (SEM) and electron tomography, to more directly obtain a void space for disordered porous solids (Tariq et al., 2011, Babu et al., 2014). These methods can provide high-resolution images of the pore structure of nanoporous materials, and thence image the nanoporous solids that can also be investigated by gas adsorption. However, samples bigger than ~500 nm at nanometer resolution cannot be imaged by the imaging techniques, and hence, it cannot be assumed that the volume sampled is representative of the pellet as a whole. Whilst it is sometimes found that the particular size of the specific volume of sample imaged overrides the correlation length of the individual void space, porosimetry followed by computerised X-ray tomography studies (Nepryahin et al., 2016) have also shown that many disordered solids are macroscopically and microscopically heterogeneous.

Integrated CXT and mercury intrusion allowed the spatial variation over macroscopic length-scales of the penetration of nanopores by mercury under a specific pressure to be monitored. In many porous materials, though similar-pore structures may exist within local regions of length-scales up to 100 μm, at the most, however, other similarly-sized regions, present elsewhere within the pellet, may possess completely different characteristic properties. Hence, for sufficient information to gain a full description of the whole pellet network of (typically) ~10^{14} pores, the whole macroscopic pellet (pore-sized $>$ mm) must be imaged. However, the available imaging techniques and the computer technology cannot provide such images now. On the other hand, representative information about the properties of a whole pellet can be deduced from a gas adsorption isotherm. Moreover, gas sorption isotherms can obtain PSDs more quickly and cheaply than the imaging techniques, and hence it is still popularly used in Industry. Thence, improvements to the accuracy of gas adsorption data are still needed.

However, research on the fundamental physical processes involved in gas adsorption in complex pore geometries has revealedthe existence of certain effects that reduce the accuracy of PSDs thus obtained. These effects are recognised as advanced and delayed condensation (Esparza et al., 2004, Hitchcock et al., 2014b). These typical effects are pore-pore cooperative in nature, and therefore the size of the effect is related to the pores of diverse size connected irregularly within porous materials, and, thus, studies of templated materials that have more regular pore structures do not assist in clarifying the real extent of these troubles in a disordered material. A model of ink- bottle pores geometries can offer the best understanding of the basic principle of advanced filling. If the adsorbate condenses in the empty ink bottle-necks, via a cylindrical sleeve-shaped meniscus, at a pressure higher than that needed for condensation via a hemispherical-shaped meniscus in the body, thence all pores will fill at the same time because that the condensation process occurring in the necks produces hemispherical menisci at the ends of the body. Delayed condensation takes place when the potential in a certain pore is lower than a void space that has the similar geometry but totally solid walls, because of the holes that exist at the side-arm branches.

Matadamas et al. (2016) have elucidated the potential influence of the pore-pore co-operative effect on the accuracy of PSDs in pore network systems using computer simulation. They have employed different pore connectivities, and levels of superposition between pore body distributions and distributions of throat size, to investigate how the advanced and delayed absorption impacts on a system of a range pore-neck interconnections. They have made a comparison between the properties of the real void space of the underlying models and those obtained from the simulated isotherms using standard analysis techniques. It was observed there is a significant error in the accuracy of the PSD obtained due to the delayed condensation. Boundary and scanning curves in gas adsorption experiments have been obtained for disordered materials in order to study the impacts of pore-pore cooperative, but the data obtained was a combined signal from the entire sample which makes the interpretation of the finding for porous materials unclear, unlike the more regular pore structure in which the signal is unambiguous (Esparza et al., 2004). On the other hand, the combined gas adsorption and mercury intrusion techniques, which include performing a series of nitrogen-mercury-nitrogen experiments on the same sample, can study the impacts of the pore-pore cooperative phenomenon in given pores within porous solids by deconvolving-out the signal from certain pores. More recently, Hitchcock et al. (2014a) have utilised the integrated technique of the gas adsorption and mercury intrusion porosimetry on a specific sub-set of pores, located within the porous network of a silica sample to investigate the differences in the adsorption behaviour of two popular adsorbates, namely nitrogen and argon, within these pores. It has been observed that nitrogen is readily wetting of solid mercury surfaces, whilst argon, on the other hand, does not wet very much. In this chapter, this recently found effect will be applied to elucidate the existence of delayed condensation for the gas sorption technique for a sol-gel silica sphere denoted Q1. Also, the integrated experiment can provide the data from mercury intrusion to allow alternative interpretations of the gas sorption data to be discounted, and a final interpretation to be gained. Furthermore, mercury thermoporometry and NMR cryoporometry are separately used to measure the sizes, to investigate the delayed condensation effects on the accuracy of PSDs.

4.2 Experimental methods and materials

The first catalyst used in this work is a commercial sol-gel silica sphere Q17/6, denoted Q1. The specific surface area is 240± 20 m^2g^{-1}. The specific pore volume is 0.5 ml g^{-1}. The sample was characterised in whole and powdered form.

4.2.1 Gas adsorption porosimetry

Nitrogen adsorption experiments were conducted at 77 K using a Micromeretics Accelerated Surface Area and Porosimetry (ASAP 2020) apparatus. The weight of the catalyst had been taken before and after the degas process as part of the requirements of the sample preparation. Prior to the experiment, the sample tube, including a seal frit and filler rod, was cleaned with distilled water and rinsed with acetone. The filler rod was used to get a lower surface area for the apparatus to allow more accuracy for the sample. Then, the cleaned tube set was dried in an oven overnight. The sample and the filler rod were placed into a gas adsorption tube and the tube was closed by a seal frit, then the tube with the sample was weighed. The tube set weight was obtained by subtracting the catalyst weight from the total weight. Heat treatment was performed on the sample under vacuum, by attaching the sample tube (containing the sample) to the degassing port, to remove any physisorbed gas. Firstly, the sample was heated under a practical vacuum (1×10^{-3} mmHg) and the temperature was set at 90 ℃ for four hours. The temperature was then increased to 150 ℃ and the sample was kept at this temperature for 12 hours, which ensured all the moisture present in the sample was removed. After this time, the heating process was stopped to allow the tube to cool to room temperature. This was followed by unloading the sample tube, keeping the seal frit attached, and weighing the sample tube to obtain the dry sample mass. Prior to the next step of the analysis process, liquid nitrogen was added into the analysis dewar to a distance of 5 cm (2 inches) from the top, using a dewar depth gauge. A Micromeretics patented isothermal jacket was then placed around the sample tube and attached to the analysis port to start the analysis. A personal computer was connected to the instrument to set the operation conditions. The relative pressures used in this work were between 0.004 and 0.995 and the process was entirely automated. The equilibration time applied in these studies was examined and found to be 5 sec.

Figure 4-1 shows the nitrogen gas sorption isotherms data, which has been obtained by Johnson Matthey (Integrated gas sorption and mercury porosimetry experiments were carried out at Johnson Matthey due to concerns about mercury contaminations of gas sorption rigs at University of Nottingham), for an experiment on a whole pellet sample from batch Q1. From the Figure 4-1, it can be seen that the nitrogen rapidly invaded the sample at low relative pressures and then extended steadily creating multilayer adsorption and capillary condensation regions. It can also be noticed clearly that a horizontal plateau appeared at the highest relative pressure suggesting that all the mesopores are filled. It can also be noticed that the amount of the adsorbed nitrogen reduces, as the pressure decreases. It is found that for open cylindrical pores, the Cohan (1938) equation suggests the corresponding model pore radius would be 7.8 nm, while the Broekhoff and de Boer (1967) method would suggest the pore radius was 12.3 nm. NLDFT (2001) suggests that spinodal condensation in open cylinders would occur at a relative pressure of 0.927 if the pore radius was 10 nm. This difference in the interpretation models belongs to the different concept of each of these methods. The Cohan equation is basically the Kelvin equation that assumes the contact angle is zero for nitrogen. It assumes perfect wetting of mercury relative to the solid surface, and the t-layer thickness of the liquid condensed on the pore wall is the same irrespective of the pore size. In contrast, the Broekhoff and de Boer Method, takes account the fact that the t-layer thickness is not the same. That means, this method determines the t-layer thickness as a variable parameter with the pore size. While the DFT is for small pores where the pore wall gets so close together i.e. very small pore. However, these methods are correct for a single pore hysteresis, but they fail to account for a network of pore, and thus, pore sizes were measured independently, using mercury thermoporometry and NMR cryoporometry, to amend them.

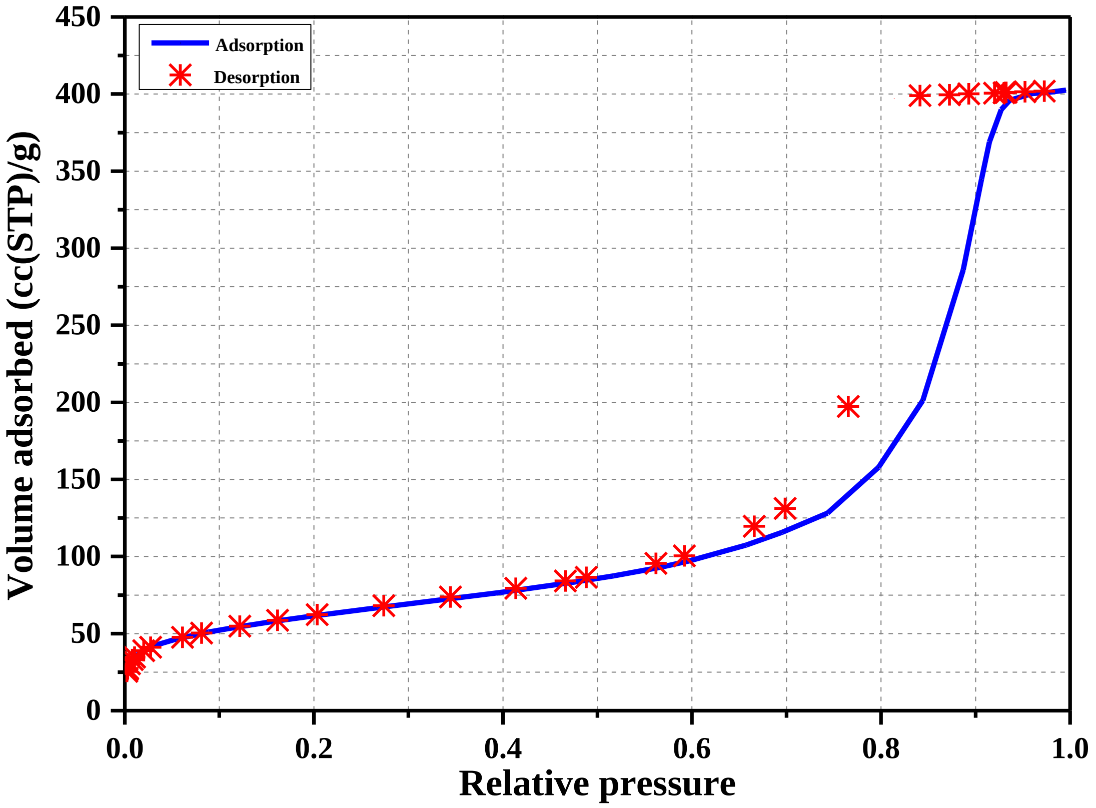

Figure 4-1: Nitrogen sorption isotherms for a sample from batch Q17/6 obtained at 77 K.

4.2.2 Mercury Porosimetry

The experiment was carried out on a Micromeritics Autopore IV 9500 mercury porosimeter (using 99.99% Hg), including a pressure range from 0.01 to 414 Mpa. The apparatus had two ports for low pressure and one for high pressure, which allows analysis for more than one sample at the same time. The instrument measured the volume intruded by mercury over each increment in the imposed pressure. The mercury experiment data were analysed according to the standard Washburn equation, and the value of mercury surface tension and the contact angle were 0.485 Nm^{-1} and 130° (Van Brakel et al., 1981, Giesche, 2006) respectively for both the advancing and receding menisci to obtain the intrusion and extrusion curves. In previous work conducted by Dim (2015), the standard equilibration time used was 10 and 30 sec, and it was found that time had no any effect on the shape of mercury intrusion/extrusion curves. Therefore, the applied standard equilibration time used here for every pressure step was 15 sec. The penetrometer used to perform the experiment was calibrated by running it blank to minimise baseline error, caused due to compressibility and heating through the analysis. The appearance of any intrusion during the blank run can be attributed to the baseline error and was subtracted from the subsequent sample run. The sample, before any experiment, was first dried under vacuum to a temperature of 140 ^{o}C (Kinney et al., 1993) for six hours to drive any physisorbed water out the sample pores. The dried sample was loaded and sealed in a penetrometer using a thin layer of vacuum grease over the top edge of the penetrometer. Thereafter, as a first step, the sample was attached to the low-pressure port using a light coating of silicone grease around the external surface of the penetrometer. The process was controlled and monitored by a computer attaching to the instrument. All the process conditions and sample information were described in a created file on this computer.

In the first stage, the sample was evacuated to a pressure of 6.7 Pa to remove any traces of water content on the porous sample. The sample pores, during the evacuation process, was intruded by mercury. The evacuation stage must be perfectly processed to avoid the uncertainty in results from contamination troubles. The pressure then increased up to ambient. After that, an assembly weight (penetrometer, mercury and sample) was taken prior to transfer it to the high-pressure step. In the high-pressure process, the pressure was raised incrementally up to a maximum of 60,000 psi (414 Mpa). At the end of the high-pressure process, the pressure was gradually reduced allowing the mercury to extrude from the disordered material stepwise, creating an extrusion curve.

Figure 4-2 shows mercury porosimetry data for a typical sample from batch Q1, with an ultimate intrusion pressure of 414 MPa. Figure 4-2a illustrates the relationship between the volume of mercury that intrudes the catalyst pores and the imposed pressure. Once the pressure is incrementally increased, mercury starts to invade the inter-particle space of the sample at low pressures, creating a long horizontal intrusion curve until all gaps between the particles are filled. When the pressure reached around 100 MPa, this allowed the intra-particle space to be intruded before it filled all of the pores at the maximum pressure point of 414 MPa generating a flat plateau at the top. This horizontal plateau suggests that the mercury penetrated all the pores at the highest pressure. An estimation of the total volume of the sample mesopores penetrated by mercury can be obtained from the mercury intrusion curve. The volume of the intruded mercury, located between the end of the low long horizontal plateau and the top plateau, represents the total mesopore volume. As the pressure was reduced, a flat plateau curve appeared and continued at the same mercury volume before mercury left the sample at a pressure of around 115 MPa.

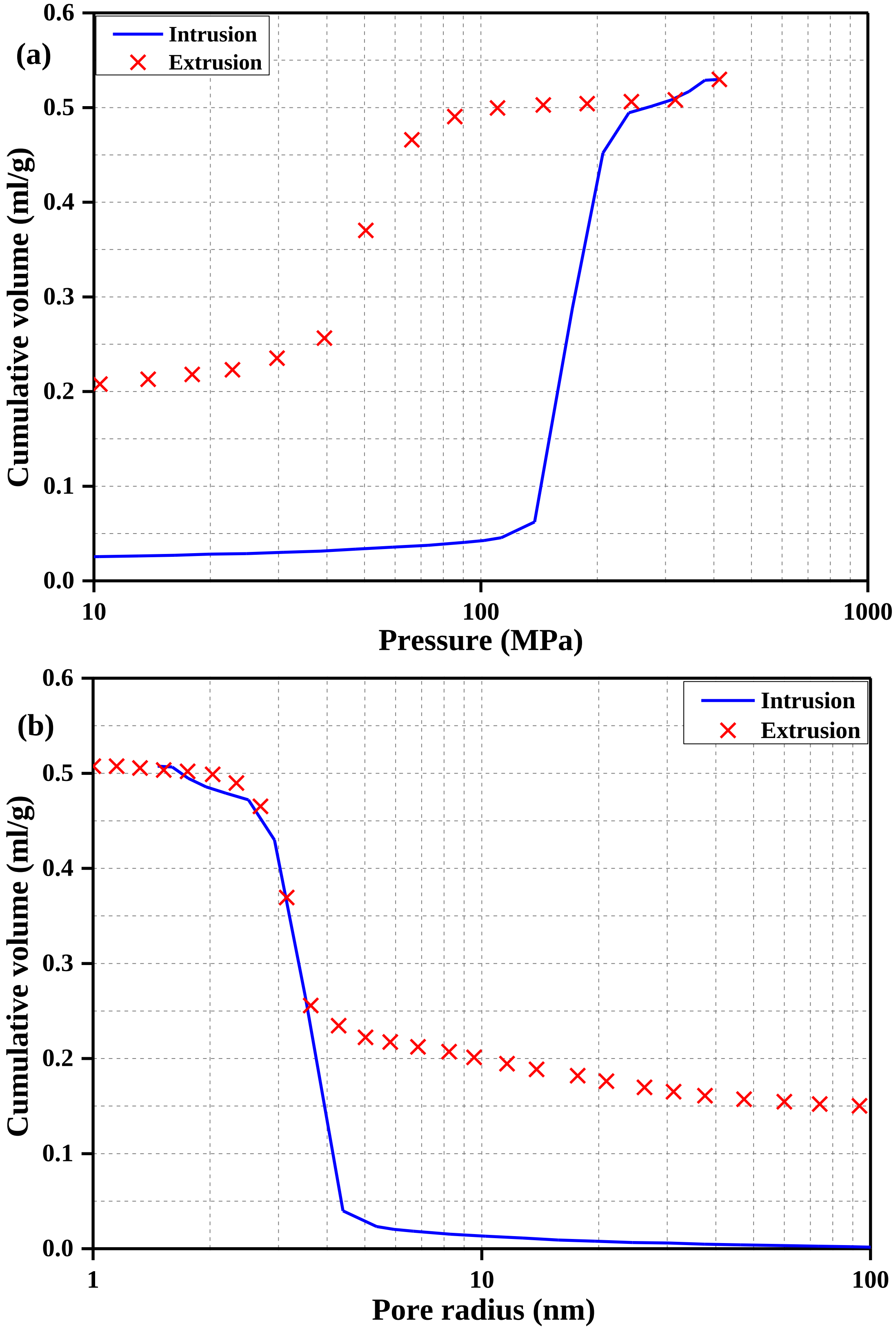

Figure 4-2: (a) Raw mercury intrusion (solid line) and extrusion (×) curves for a typical sample from Batch Q1, and (b) These data following removal of inter-pellet intrusion and analysis of data by Kloubek correlations in the Washburn Equation using parameters in Table 1.

The mercury then dramatically extruded from the sample until 40 MPa before its extrusion volume became constant with about 20 % volume entrapped.

The data in Figure 4-2a has been analysed using the Kloubek correlations in the Washburn Equation with the intrusion parameters listed in Table 4-1, and values of A and B of -20 and -187, respectively, for extrusion. Initially, in the first part, as shown in Figure 4-2b, mercury intrusion and retraction curves both appeared almost a horizontal plateau. From the Figure 4-2b, it can be observed that superposition of mercury intrusion and retraction curves using these values, is obtained over part of the range of smaller pore sizes. It is noticed that the extrusion curve deviated from the intrusion curve at a special point on the intrusion curve. This point indicated that less mercury extruded from the sample in comparison with the mercury amount that was intruded. It is observed from Figure 4-2b that the region of divergence of the extrusion curve from the intrusion curve suggests that a large amount of mercury entrapment takes place for pores of radii ~3.5-4.5 nm. This is smaller than the size proposed from nitrogen sorption above.

Table 4-1: Parameters for use in Washburn Equation.

Material	**A.10^3/(N.m^{-1})**	**B.10^{12}/N**	**Range of validity /(nm)**
Silica (advancing meniscus)	**-302.533**	**-0.739**	**6-99.75**
Silica (retreating meniscus)	**-68.366**	**-235.561**	**4-68.5**

4.2.3 Thermoporometry experiment (DSC)

The thermoporometry experiments were performed using a DSC Q10 V9.8 machine which is provided by a cooling device with a system to process the data. The DSC experiment was implemented on the sample containing entrapped mercury, prepared by MIP, as a probe fluid. The purpose of the instrument is to measure the pore size distribution (PSD) of a particular catalyst via determining the freezing and melting curves of the liquid present in the catalyst.

The sample containing entrapped mercury was transferred to the DSC pan. The sample was then encapsulated such that the pan becomes airtight using the sample press. The airtight pan will prevent the mercury from being evaporated during the experiment. The pan was transferred to the sample holder of the DSC, and the lid closed. Three ramp rates of 0.5, 1.0, and 1.5 ℃ min^{-1} and a temperature range from -80 ℃ to -37 ℃ were used to measure the melting curves. The low scanning rate was applied to avoid noisy response, arising due to the high heating rate, which influences the signals. The sample was frozen to the temperature of -80 ℃ and then kept at this temperature for 30 minutes to ensure that the temperature is homogeneously distributed. Once the cooling stage is completed, the sample was warmed back to the room temperature, and the melting curve was measured within the temperature range between -80 ℃ and -37 ℃. The measurement's resolution of the heat flow rate in the DSC is about ± 0.5 μW, with an accuracy of ± 2 μW.

Figure 4-3 exhibits the DSC melting curves achieved for the mercury entrapped following the mercury porosimetry experiment in different ramp rates on the sample Q1 that gave the data shown in Figure 4-2a. The data shows the melting point of the pore peak and the bulk peak. The results revealed that the heating rate had no significant effect, and thereby the low heating rate was adopted to obtain the data. It can be seen that the melting point peak of the bulk mercury occurs at a temperature of -38.8 °C, and the modal peak in the melting curve, for mercury in the pores occurs, at a temperature of -51 °C. The difference between the two peak temperatures, which represents the melting point depression, which is about 12 °C.

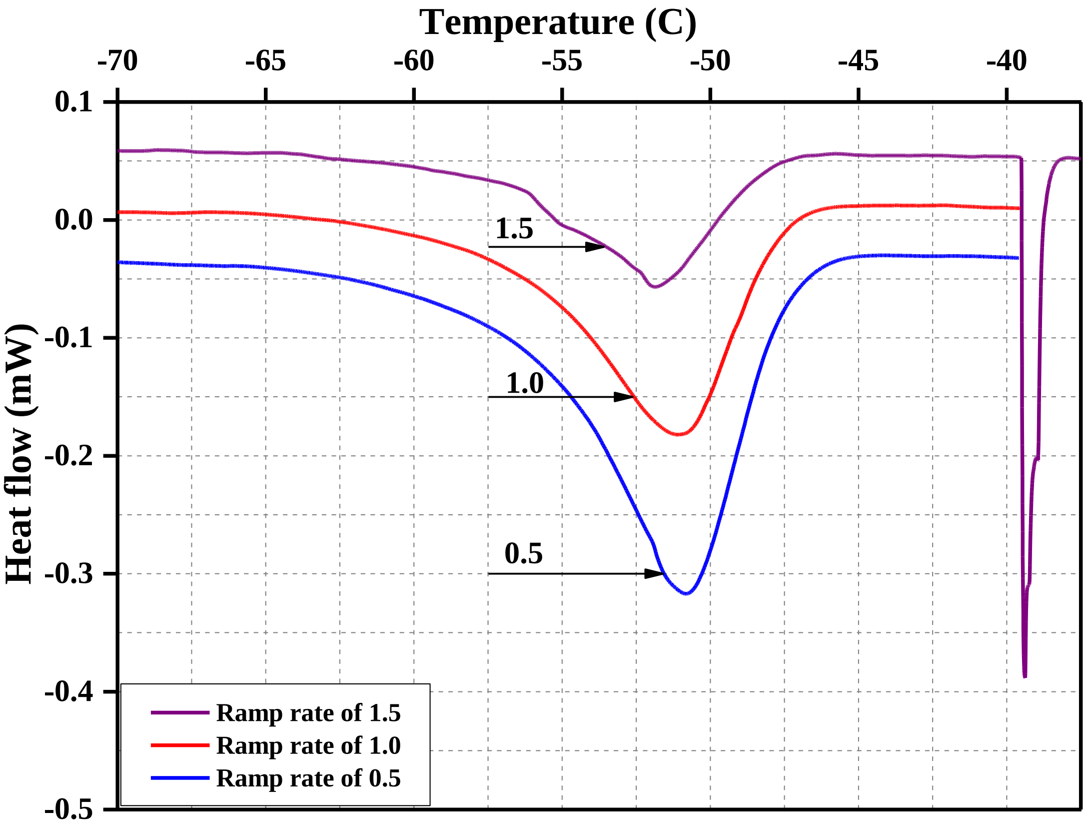

Figure 4-3: DSC cryoporometry melting curve for the mercury entrapped in the sample Q1 used for the porosimetry experiment giving rise to the data in Figure 4-2, for various ramp rates.

The value of the Gibbs-Thompson factor used in Equation 3.8, for melting from a hemispherical meniscus, is 90 K nm. Therefore, the characteristic crystal size for entrapped mercury is about 7.5 nm. This corresponds to a pore radius of ~3.8 nm (assuming a non-freezing layer thickness of one atomic diameter). For melting via a cylindrical sleeve-type meniscus, the Gibbs-Thompson parameter is 45 K nm, and thus the pore sizes obtained would be half the size of those reported above.

4.2.4 Integrated gas sorption and mercury porosimetry

The raw data for a nitrogen gas sorption experiment, which has been conducted for batch Q1 catalyst before and after mercury intrusion porosimetry experiment, is shown in Figure 4-4a. It can be observed that the appearance of a flat plateau at the top of the isotherms suggests that the mesopores are fully filled with condensed nitrogen. It can also be noticed that mercury entrapment leads to a reduction in ultimate amount adsorbed. The difference between the two isotherms, which represents the difference in the cumulative amount adsorbed, can be computed by subtracting the raw data obtained after mercury entrapment from that obtained before porosimetry as presented in Figure 4-4b. From Figure 4-4b, the adsorption in the pores occurred mainly at the relative pressure of 0.927 which is represented by the large positive peak, corresponding to the capillary condensation pressure where those pores become occupied by mercury. The analysis of the isotherms revealed, according to the Cohan equation for pores as an open cylinder, that the pore radius was 7.8 nm. NLDFT suggests that the pore radius accessible to nitrogen at the relative pressure of 0.927, for open cylindrical pores, would be 10 nm, while the Broekhoff and de Boer method would suggest the pore radius was 12.3 nm. In Figure 4-4b, the main negative peak in the plot of the difference in incremental amount adsorbed appeared at a relative pressure of 0.844. This pressure suggests, based on the Cohan equation, that the pore radius, assuming the pores shape is a cylinder, would be 3.8 nm, whilst pore radius of 6.0 nm was suggested by the Broekhoff and de Boer method.

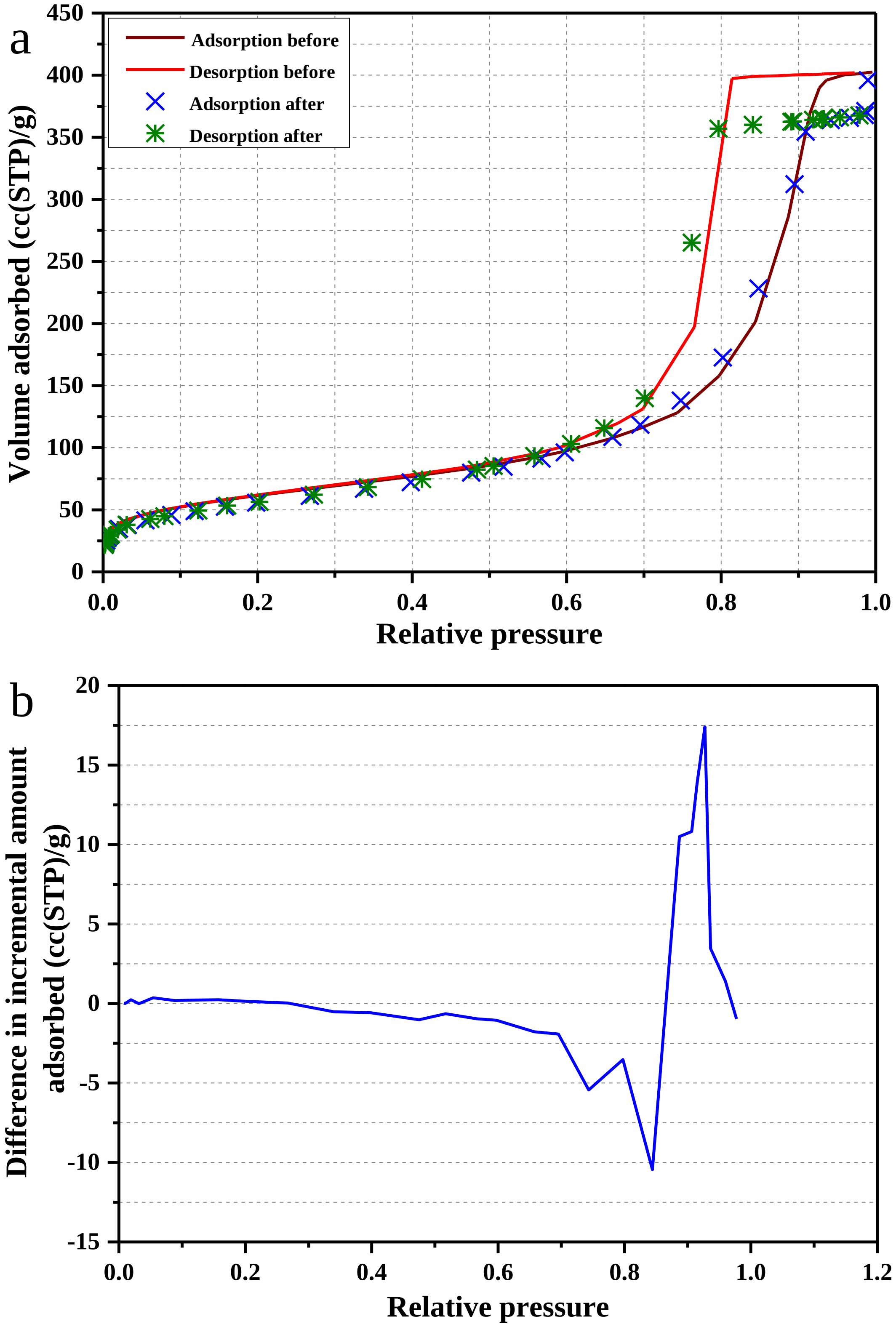

Figure 4-4: (a) Nitrogen adsorption isotherms for a sample from batch Q1 obtained at 77 K for before (solid line) and after (X and ✳) entrapment of mercury in the integrated experiment. (b) The plot of the difference in incremental amount adsorbed at particular relative pressures obtained by subtracting the isotherm obtained after porosimetry from that obtained beforehand.

Figure 4-5a shows argon gas sorption and mercury intrusion porosimetry for the same sample, Q1, for both before and after mercury porosimetry in an integrated experiment. The incremental difference in the amount adsorbed for nitrogen and argon adsorption on typical samples from batch Q1 is shown in Figure 4-5b. Data from two samples are shown for each adsorbate to elucidate the size of the inter-sample variability within the batch. It can be seen that for both types of nitrogen plots, a very evident negative peak appeared at lower pressure in the area of the capillary condensation of the isotherms before the stronger positive divergence at high pressure. However, in the case of the argon plots, the negative peak appears as only a slight deviation at low pressure, keeping the same deviation for the large positive peak at high pressure. It is very explicit the large difference in the negative peaks between nitrogen and argon plots, where, for nitrogen, they spread down at a low pressure ranging between about -20 to -30 cc(STP)g^{-1}, while, for argon, the variation in the cumulative plots suffer a slight change for some samples. The distance between about 0.05 and 0.6 p/p° in the gas adsorption isotherms represents the multilayer regions which were adapted to the fractal BET equation and the finding model parameters are presented in Table 4-2. It can be noticed that the capacity of the monolayer in all cases falls after mercury intrusion, which is an indication of losing the available porosity. It can also be shown, for nitrogen, the BET constant and fractal dimension drop dramatically following mercury entrapment, whereas not for argon. This suggests that the nature of the surface occupied by the nitrogen multi-layer is changed by mercury entrapment while that covered by argon is largely not.

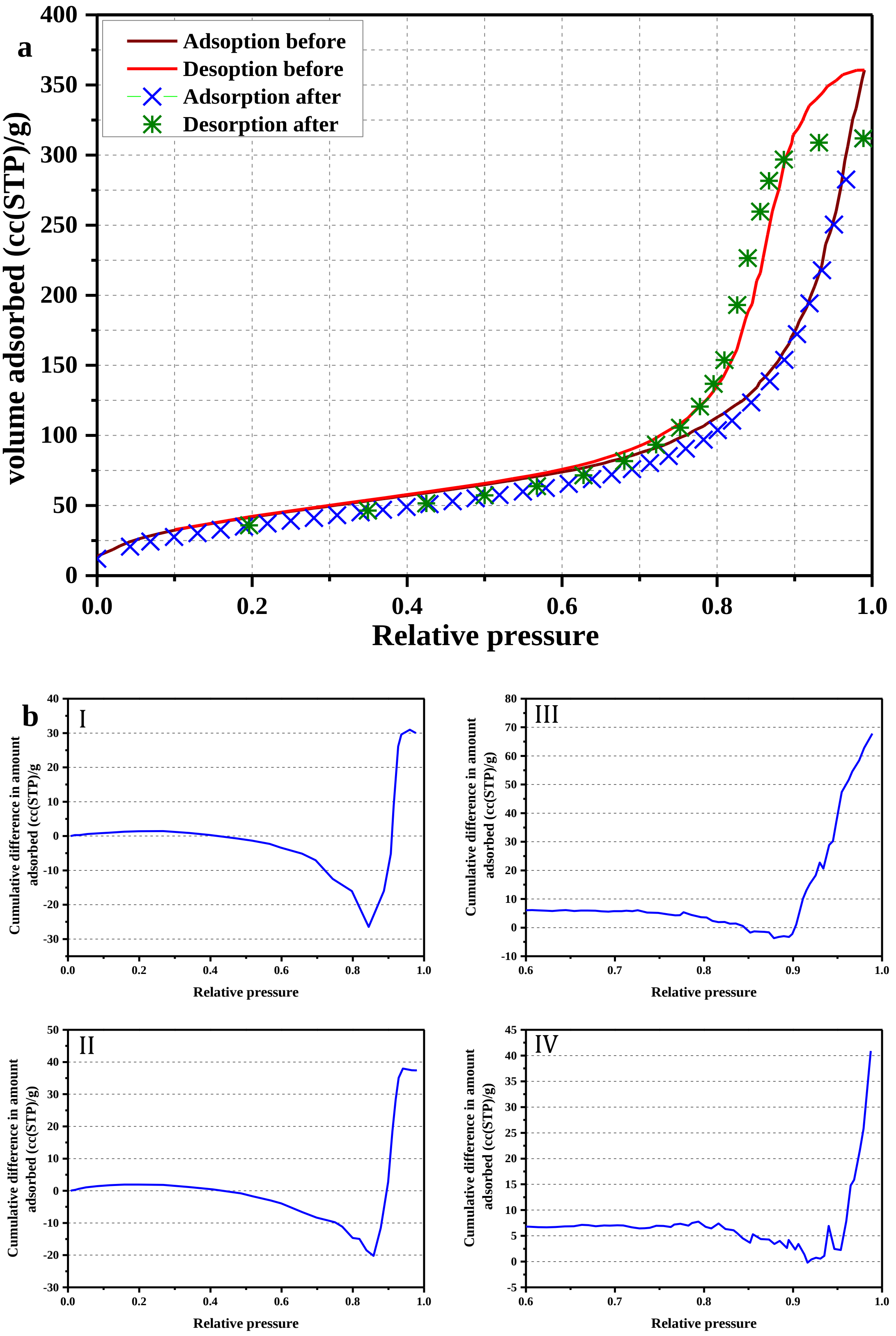

Figure 4-5: (a) Argon sorption isotherms for a sample from batch Q1 obtained at 87 K for before (solid line) and after (×) entrapment of mercury in an integrated experiment (subjected by Johnson Matthey), and (b) Cumulative difference in amount adsorbed plots for nitrogen (a and b) and argon sorption (c and d) on a given sample from batch Q1.

Table 4-2: Parameters from fitting the fractal BET model to adsorption isotherms for nitrogen or argon obtained before and after entrapment of mercury in samples from batch Q1.

Sample	**Adsorbate**	**Before**			**After**		
		Monolayer capacity/(cm^{3}(STP)g$^{1)}$	**BET constat**	**Fractal dimensin**	**Monolayer capacity/(cm^{3}(STP)g$^{-1)}$**	**BET constant**	**Fractal dimensin**
1	**Nitrogen**	**60.0**	**40.9**	**2.45**	**40.8**	**26.0**	**2.20**
2	**Nitrogen**	**50.1**	**57.3**	**2.42**	**33.4**	**36.1**	**2.12**
3	**Argon**	**42.2**	**18.2**	**2.39**	**34.9**	**19.1**	**2.33**
4	**Argon**	**45.3**	**18.0**	**2.41**	**38.3**	**18.5**	**2.38**

4.2.5 NMR Cryoporometry

Experiments were performed on a Bruker Avance ш NMR spectrometer. The static field strength of the magnet was 9.4 T, with a response frequency of 600 MHz. The sample was soaked with water to overfill the pores prior to the cryoporometry experiment. The number pellets used for NMR cryoporometry is similar to the number pellets used in mercury porosimetry. The extra water provides the bulk melting curve as a reference. The soaked sample was then transferred into the NMR tube and sealed to prevent evaporation of the excess water. Thereafter, the NMR tube was loaded into the spectrometer to start the analysis. Initially, the sample was cooled to 250 K to make sure that all liquid became frozen. A melting run was conducted following this point, and the temperature was increased up to below the bulk melting in steps of 0.3 K per 10 minutes. The NMR signal was taken, as a function of temperature, at each temperature following equilibration. The spin echo time was chosen such that no signal was obtained when the sample was completely frozen. Freezing scanning curves were also achieved through stopping the sample melting at a given point before the ice in the macroporosity and bulk phase had melted, and then cooling the system.

Figure 4-6 shows the melting curve obtained from the NMR cryoporometry for a whole pellets sample of Q1 soaked with water. The melting curve presents two step rises in NMR signal corresponding, at the lower temperatures, to the melting of the liquid within the pores, and, at the higher temperatures, the bulk layer on the exterior of the pellets. These steps are separated by a plateau which represents the total pore volume. The slight decline toward higher temperatures in this plateau is due to Curie effect. The total liquid volume in the sample is represented by the other plateau that appears at the top of the melting curve. The point of inflexion in the step for the melting of the water in the pores occurs at 267.0±0.5 K.

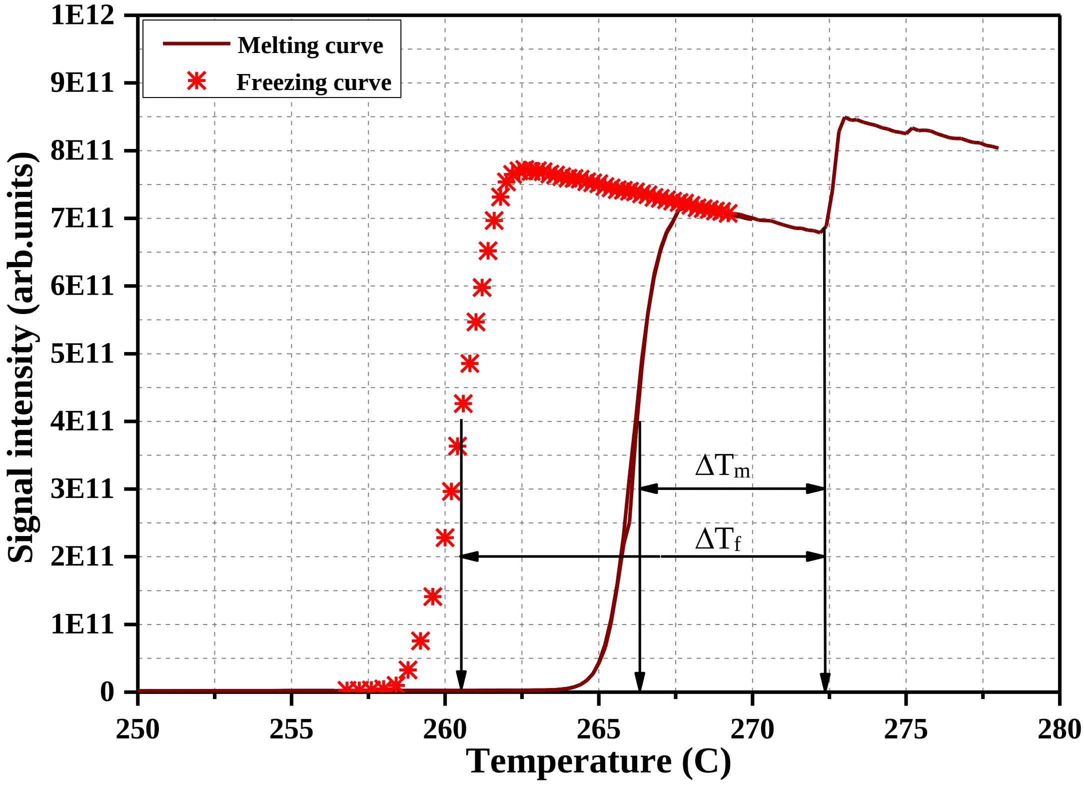

Figure 4-6: NMR cryoporometry melting curve for a sample of Q1 spheres fully saturated with water.

For a Gibbs-Thompson parameter of 52 K nm (for melting from a cylindrical sleeve meniscus) and non-melting layer thickness of 0.4 nm, calibrated using templated mesoporous silicas (Schreiber et al., 2001), this suggests the modal pore size is 9.3±0.8

nm, corresponding to a pore radius of 4.7±0.4 nm. From the Figure 4-6, it can be seen that the difference in freezing temperature ΔT_f is 12 K and the difference in the melting temperature ΔT_m is 6 K. This means the value of the ΔT_f is twice of the value of ΔT_m, and this implies that the pore is cylinder type. For a cylindrical pore, during the freezing process, liquid solidifies from the end of the pore toward the axial direction, where the liquid phase was in communication with bulk solid. For spherical pores, melting is started at the liquid film covering the pore surface and spreads out radially from the surface toward the pore bulk. Each experiment was repeated twice and no significant changes in the values of ΔT_m and ΔT_f were found.

4.3 Discussions

Different experimental techniques, conducted on the sample Q, have been revealed that there is a difference in the pore size obtained from those techniques. It has been found that the pore size, measured by mercury intrusion porosimetry, through intrusion process for mercury in the pores of batch Q1 is smaller than that measured by gas sorption and standard analysis techniques. Moreover, the pore size obtained from gas sorption is also larger than that obtained from NMR cryoporometry, using water as a probe fluid, and that obtained from DSC thermoporometry using entrapped mercury as a probe fluid. These results are consistent with what would be anticipated if gas sorption was affected by delayed condensation. All of the standard data analysis methods for the gas sorption, as described in textbooks (Gregg et al., 1967, Rouquerol et al., 2013) (Cohan equation, BdB, and NDLFT), all assume a parallel pore bundle model for the void space, and the effect of pore- pore cooperative phenomena in adsorption is neglected. Therefore, all standard techniques will be affected by the errors measured above. However, the negative peak in the difference in cumulative amount adsorbed for nitrogen sorption indicates that the condensation pressure for some pores not intruded by mercury is reduced. Based on the relative condensation pressure for the negative peak for nitrogen adsorption, the Cohan equation suggests that the pore size of the Q1 sample is 7.8 nm which is similar to that obtained from the thermoporometry method for pores intruding with mercury of 7.6 nm. Wardlaw and McKellar (1981) have investigated the geometry effect of pores and their interconnections on the form of mercury intrusion-extrusion curves, using glass micromodel model involving T-junctions, which have the same size as the side-arms of the junctions. It was found that the side-arms can only be filled with mercury. Therefore, it is suggested that for the pore system having the same pores size, mercury patches the hole at the T-junction branch making the pore behave like an open cylinder, and this pore network consistent with the nitrogen data. This patching removes the effect of the pore-pore cooperative phenomenon, resulting in removing the delayed condensation, and assists to obtain a precise calculation of pore sizes using standard pore methods according to the macroscopic theories, avoiding microscopic theories such as NLDFT and Monte-Carlo methods.

However, the effect of a pore-pore cooperative phenomenon is found as advanced melting in thermoporometry and thermocryoporometry methods (Kondrashova et al., 2010, Kondrashova and Valiullin, 2015). During advanced melting, the fluid in the narrow neck melts in a radial direction via a cylindrical sleeve meniscus. This melting would help the probe fluid, in a larger pore body joining with the neck, to be melted via a hemispherical meniscus. Kondrashova and Valiullin (2015) have conducted experiments and simulations to study the effect of the geometry on the melting and freezing points. Both studies have suggested that the advanced melting would just occur when the size of the pore body does not more than twice of that the pore neck. It is possible that the advanced melting effect is responsible for the melting of the mercury in Q1. However, the ratio in the pore sizes obtained from gas adsorption and thermoporometry is more than twice. This suggests that the possibility of advanced melting would not change the result that the pore sizes obtained from gas adsorption are overvalued. Moreover, the matching of the results of the mercury porosimetry with the thermoporometry results proves the explanation of the data obtained from the thermoporometry as suggested above. The data obtained from the mercury intrusion presented in the integrated technique permits the alternative interpretation of the gas sorption data to be discounted. If this scenario has dominated, the pore sizes obtained from different characterisation techniques, named mercury porosimetry and gas sorption, would be the same value, but the obtained values were different. Consequently, a scenario of a dead-end ink bottle can be neglected and the correct scenario is the delayed condensation.

The difference in the wetting of the entrapped mercury surface for the gas adsorbate, used in the homotattic patch modelling, would identify the trends that could be predicted in the fractal analysis of the multilayer area of the isotherms before and after the mercury intrusion experiment. It has been found that the experimental data analysed by BET and fractal methods is consistent with the interpretation that mercury is relatively wetted by nitrogen, with respect to silica, it is not wetted by argon. The anticipated effect of entrapped mercury on the form of the cumulative difference in the amount adsorbed plots for nitrogen and argon has the same prediction in the case of the presence of the delayed condensation phenomenon as discussed in chapter three. Hence, these results indicate that entrapped mercury is differently wetted with nitrogen and argon, as reported in a previous study, and this effect reveals that delayed condensation presents in Q1.

In porous materials, two phenomena, namely delayed and advanced condensation effects, can arise in a pore network. The impact of the delayed condensation phenomenon acts to make the size of the pores seem larger than the real size, whereas the advanced condensation effect makes larger pore sizes look smaller than the real one. The presence of these effects together in the disordered pore network cannot entirely compensate for each other in the action of condensation, since the delayed condensation phenomenon comes from pores that are perpendicularly attached to the cylinder-pore axis, while smaller pores that are direct, actually connected to the larger pores give rise to the advanced condensation effect where a hemispherical meniscus can form at the end of the larger pore. In a complex pore network, it is very rare that a compensation process, for the effect of one or more side branches attached to the main pore, would happen when small pores joined to the entry of large pore with the right size. Hence, one effect is probably controlling the other, and the delayed condensation phenomenon is dominant in the case of Q1 catalyst.

4.4 Conclusions

The findings show that nitrogen wets the surface of the entrapped mercury within silica pores, whereas argon does not wet. This difference in wetting has been employed to detect the delayed condensation effect that appears in the gas adsorption within disordered silica material. It is also found there is a difference in the measured pore size, which exceeds a factor of two, which is caused by the delayed condensation effect for gas adsorption, and this error in pore size has been confirmed by complementary thermoporometry techniques. These results reveal that the presence of the discrepancy between the pore sizes for porous solid materials gained by different methods does have recognisable and quantifiable reasons. Given the difficulty in measuring the pore size accurately within the disordered materials, it was necessary to use different techniques to support the obtained results and give them adequate confidence in order to apply them in wider studies, and this confidence should be now provided by the new technique above to allow future work. It has been detected that the best way to gain precise pore size distribution is by focussing on the determining the level of the interaction effects between pore and pore rather than using a microscopic characterisation of the density of the adsorbate phase in each pore.

CHAPTER 5

SILICA-ALUMINA CATALYST

5.1 Introduction

It is the purpose of this chapter to present the difference in the capability of argon and nitrogen to wet surfaces of mercury to examine pore-pore interconnectivity. Wardlaw and McKellar (1981) have revealed that mercury is inclined to be retained in the largest void space, and this means that mercury can be expected to preferentially fill specific sub-clusters of the pore size correlation, such as macropores ‘highways’ (or ‘motorways’). This feature can make a change in the pore shape when new surfaces of mercury are originated at the point connected between mesopores and macropores containing entrapped mercury, converting the original form from open pores to dead-end pores. The pore potential of nitrogen is subject to a considerable alteration, due to its high capability to wet a mercury blocked-end wall compared to argon which does not suffer such a change, and thus exhibits a shift in condensation pressure. Hence, in a comparison between the adsorption data of nitrogen and argon allows particular mesopores adjoining macropores to be specifically recognised.

Taking into account that the information obtained from the new analysis method is indirect, it is very important that the characterisation of the pore geometry needs to be validated. Freezing and melting curves in NMR cryoporometry are used to estimate pore connectivity within the void space of mesoporous materials in the presence of the pore-blocking effect (Perkins et al., 2008). Hence, several techniques, such as cryoporometry, gas sorption isotherms, and mercury intrusion experiments, will be applied to validate the new method and elucidate that the physical properties of the pore structure that are obtained and consistent with that obtained from different methods which each has a different physical process. This can be achieved when specific effects, such as snap-off effect in mercury extrusion, and the effect of advanced melting in NMR, are considered.

5.2 Experimental method and materials

The material used in these experiments was a silica-alumina catalyst. Through the elemental analysis conducted on the catalyst, the five major elements that material consists of are shown in Table 5-1. In addition, there are traces of some other elements within the structure such as potassium and tin. It can be observed from Table 5-1, that a silica-alumina material represents most of the catalyst.

Table 5-1: Elemental abundance for major elements in silica-alumina material.

Element	Amount/ wt.%	Amount/ at.%
Al	**37.45**	**40.54**
Si	**46.58**	**48.44**
Cl	**7.52**	**6.20**
Ti	**4.97**	**3.03**
Fe	**2.20**	**1.15**

5.2.1 Computerised X-ray tomography (CXT)

The sample before and following mercury intrusion/extrusion porosimetry was imaged using 3D Computed X-Ray Tomography Microscope Apparatus of model VeraXRM-510 provided by Xradia Inc, Pleasanton, CA, USA, with high resolution of 5.5 μm. Typically 2-3 pellets of each sample type were imaged. Radial and axial plane cross-sections images have been taken by CXT, for a typical sample of a silica-alumina catalyst as shown in Figure 5-1.

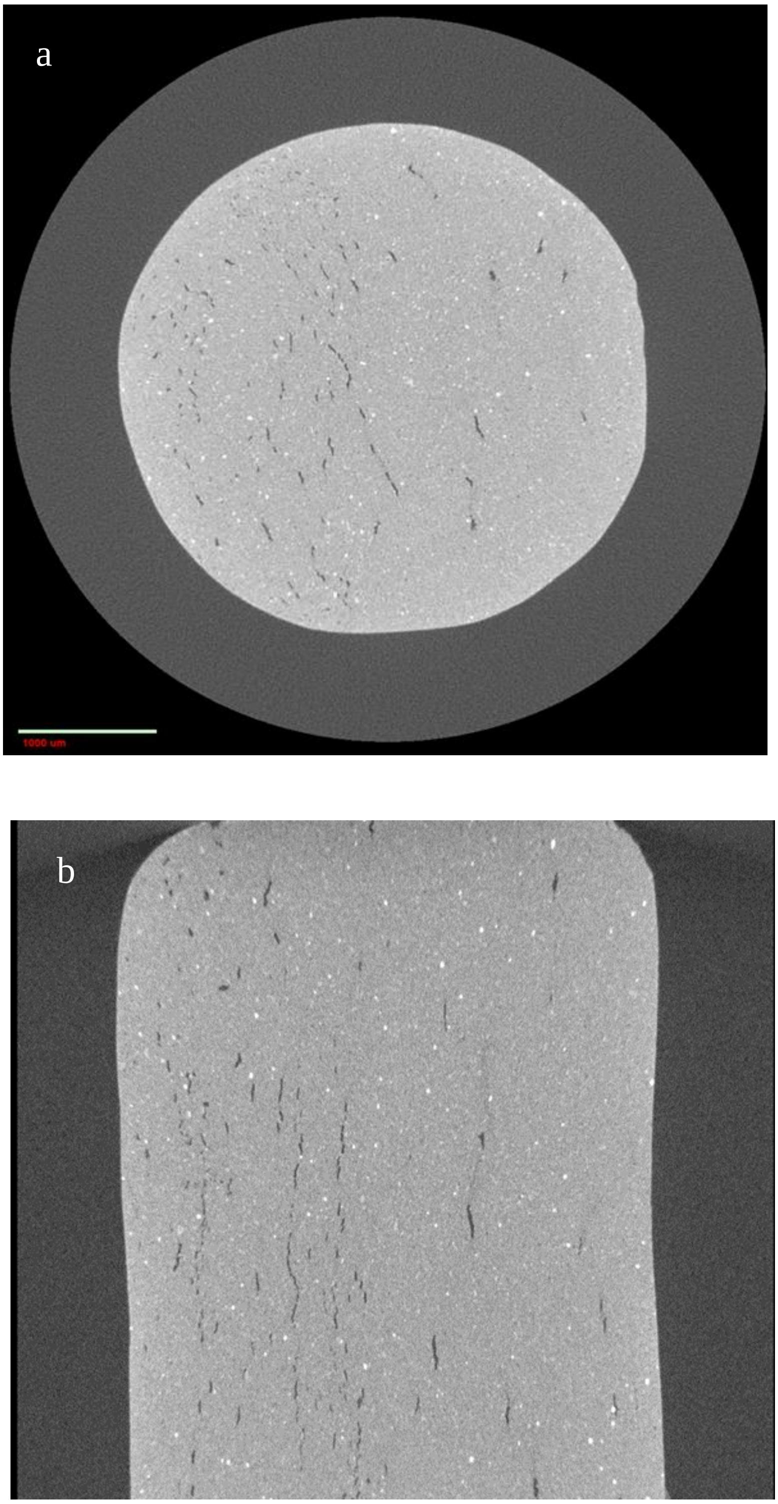

Figure 5-1 (a) Radial plane and (b) Axial plane CXT images of typical cross-sections through a sample of Silica-alumina Pellet. The lightest grey-level corresponds to highest density, and dark regions correspond to porosity. The scale bar corresponds to 1000 µm.

The dark worm-like shapes in the image are macro-pores within the pellet's body. Given that the macroscopic spatial distribution of macroporosity in the CXT images is not uniform, it can be seen that a technique that permits macroscopic assessment of the fraction and type of mesopores directly accessible from the macropores would be important for this material.

5.2.2 Integrated gas sorption and mercury porosimetry

The instrument known as an Accelerated Surface Area and Porosimetry (ASAP) Micromeritics type 2020 was employed to perform gas adsorption isotherms experiments under the condition of liquid nitrogen temperature. The sample was uploaded into a pre-weighed tube of Micromeritics gas adsorption and the tube was tightly sealed by a frit. The sample was heated under vacuum to a temperature of 90 ℃ at 10 ℃ min^{-1} to remove any physisorbed gases. The sample was held at this temperature for one hour before it was heated to 350 ℃ at 10 ℃ min^{-1} and kept at the temperature for 16 hours under a practical vacuum of 1×10^{-3} mmHg (0.13 Pa). Once the heating process was completed, the sample tube was removed from the apparatus of ASAP 2020, while keeping it sealed, to compute the mass of the dry sample. The sample was surrounded by Micromeritics patented isothermal jacket before it was reattached to the ASAP apparatus. The gas sorption process was fully automated, and the relative pressures investigated were between 0.004 and 0.995. The test was conducted under an equilibration time of 5 sec.

Following the experiment of gas adsorption, it was allowed for the sample tube to reach ambient temperature (~20 ℃), and the sample was then moved to a Micromeritics mercury penetrometer. A small glove box was used for the transfer process and was under a dry nitrogen atmosphere. This process was to prevent any trace of water from transferring from the surroundings onto the sample during the transfer process between sample tubes. A Micromeritics Auto-pore IV 9450 equipment was then utilised to perform a mercury intrusion/extrusion experiment. To remove any physisorbed water that had adsorbed on the sample while it moved from the instrument of the gas adsorption, a vacuum process was conducted on the sample under pressure of 6.7 Pa. Once the experiment was running at vacuum, mercury was allowed to enter the penetrometer and then the pressure was increased toward ambient. The pressure was then increased from ambient to 414 MPa with an equilibration time of 15 sec between pressure steps during the entire process of mercury porosimetry.

Following the experiment of mercury intrusion porosimetry, the sample and mercury were transferred to a fume hood and placed in a crucible. The sample was then separated from the mercury using tweezers and moved back into the tube for Micromeritics gas adsorption. A dewar was filled with liquid nitrogen to keep the system at a temperature of 77 K during the analysis before the gas adsorption tube was reattached to the instrument of the gas adsorption Micromeritics ASAP 2020. The sample was left within the system for one hour to make sure all the mercury entrapped the sample was frozen, and then the system was subjected to a vacuum process to start the next experiment of nitrogen adsorption. Making all the mercury freeze is very important to avoid any a potential hazard what would arise due to the mercury vapour which can be vented to the laboratory via the vacuum pump. Moreover, the freezing of the mercury means no mercury leaves the pores and keeps it entrapped. While the mercury was frozen, the experiment of the nitrogen adsorption was repeated.

Hitchcock et al. (2014a) have revealed that the fractal dimensions obtained from argon sorption following mercury intrusion porosimetry for silica surfaces agreed with those obtained by SAXS. These findings suggest that the adsorption following mercury entrapment was not affected by contamination that could be caused while the sample was transferred between the two processes in the integrated experiment.

Argon sorption conducted on the sample before and after mercury entrapment was quantified on a Micromeritics 3500 3Flex accepted with a Cold Edge Cryostat to bring down the temperature of the sample to 87 K.

Before the first isotherm (pre-mercury intrusion), the sample was heated under vacuum to a temperature of 90 ℃ at 10 ℃ min^{-1}. The sample was held at this temperature for one hour before it was heated to 350 ℃ at 10 ℃ min^{-1} and kept at the temperature for 16 hours under a practical vacuum of 1×10^{-3} mmHg (0.13 Pa). After the degassing process, the sample was cooled to a temperature of 87 K using the cryostat. Once thermal equilibrium was achieved, argon adsorption isotherms were computed with an equilibrium time of 10 sec.

When the experiment completed, the sample was allowed to come to room temperature and the sorption tube refilled with nitrogen. The sample was then moved to a mercury penetrometer and a full mercury isotherms process run. The pressure applied in the intrusion curves ranged between 0.003 MPa and 413.7 MPa, and on the retraction curves, was from 413.7 MPa to 0.103 MPa, with an equilibration time of 15 seconds. The sample then, after the mercury intrusion/extrusion experiment, was discharged, and all particles of the sample separated and uploaded into a physisorption tube. The sample was then cooled to 87 K and kept for one hour to make sure all mercury invaded the sample became frozen, and it had reached the equilibration before the sample was evacuated in preparation for the second experiment of argon sorption. Once the analysis has completed, the sample has to be immediately charged from the mercury penetrometer and cooled as soon as possible. After one hour cooling, the sample was evacuated until a pressure of less than 0.133 Pa.

5.2.3 Mercury thermoporometry

The sample used in the thermoporometry experiment was entrapped by mercury and prepared via mercury intrusion porosimetry. The experiment of Differential Scanning Calorimetry (DSC) was achieved using DSC Q10 V9.8 instrument and generally based on the method reported in detail in Bafarawa et al. (2014) except where stated here. The DSC machine started with freezing the sample prepared with entrapped mercury to the temperature of -80 ℃, and then left at this temperature for 30 minutes to ensure temperature homogeneity. The temperature range used to measure the melting curves was from -80 to -37 ℃ at a low scanning rate of 0.5 ℃ min^{-1}. Preliminary studies affirmed this rate was the most appropriate. The DSC has the ability to calculate the rates of the heat flow with a resolution of ±0.5 μW and a precision of ±2 μW.

5.2.4 NMR cryoporometry

The spectrometer used in the experiments was a Bruker Avance III 600 MHz. Prior to the NMR experiments, the sample was immersed in water to complete saturation, and the sample with the confined water was then uploaded to the spectrometer and super-cooled to 250 K, and the temperature was then increased up in steps of 0.3 K per 10 minutes. The reading of the NMR results was taken at each temperature following equilibration. The echo time was set up such that no signal was gained when the sample was entirely frozen. The cryoporometry freezing scanning curves were also obtained, starting at a point on the boundary curve before the ice in the bulk phase had melted, but the ice in the pores had melted.

5.3 Experimental Results

5.3.1 Integrated gas adsorption and mercury experiment

Figure 5-2 and Figure 5-3 show the nitrogen and argon sorption isotherms, respectively, obtained before and after mercury entrapment following a mercury porosimetry experiment.

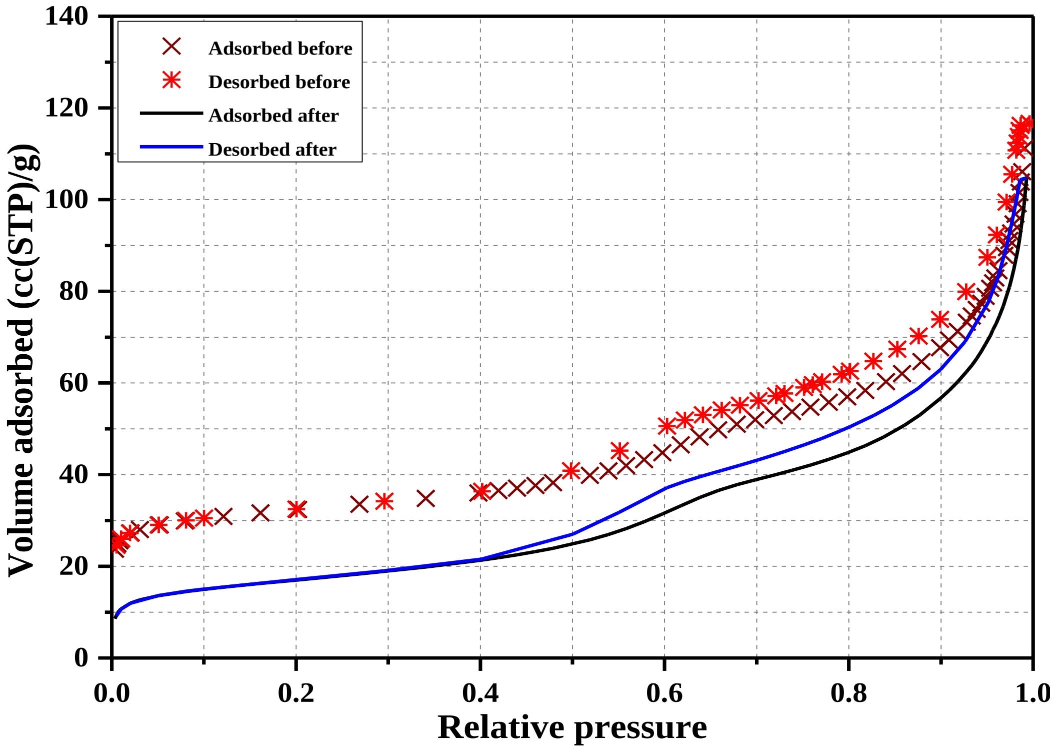

Figure 5-2: Nitrogen adsorption (black line after porosimetry; × before porosimetry) and desorption (blue line after porosimetry; ✳ before porosimetry) isotherms conducted at 77 K for a typical sample of Silica-alumina catalyst.

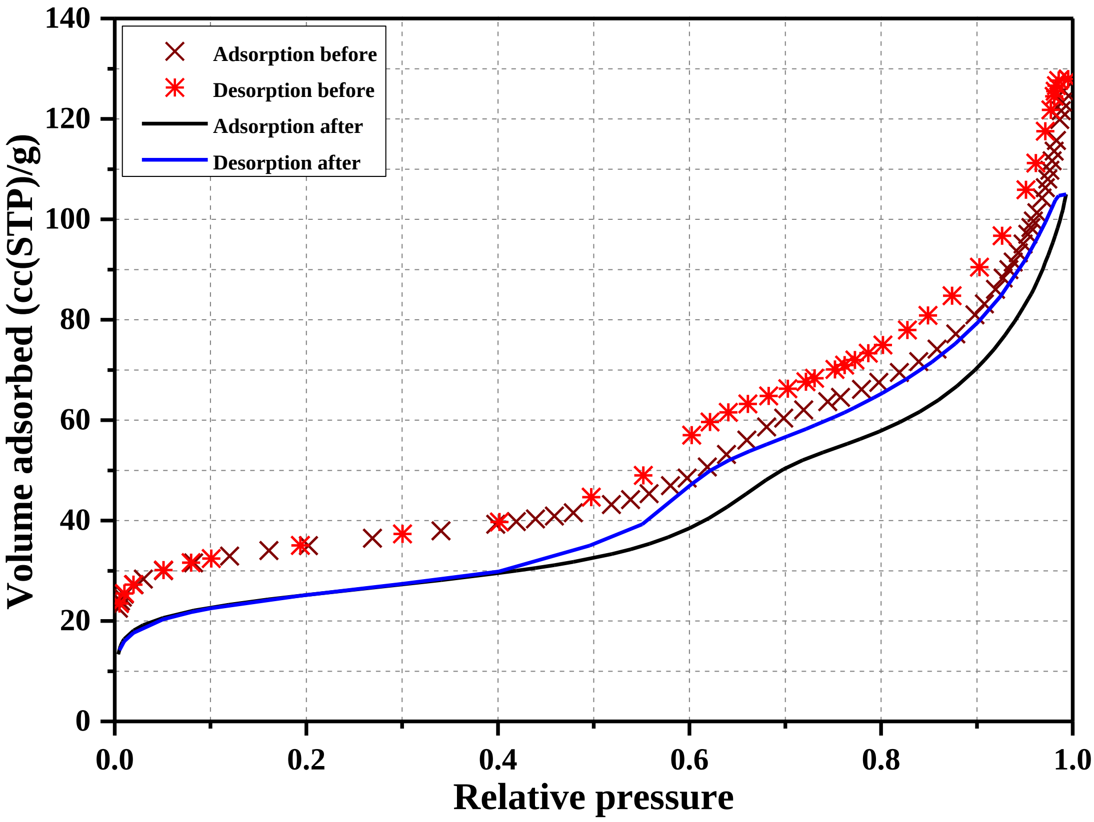

Figure 5-3: Argon adsorption (black line after porosimetry; × before porosimetry) and desorption (blue line after porosimetry; ✳ before porosimetry) isotherms conducted at 87 K for a typical sample of Silica-alumina catalyst.

In the cases of both adsorbates, the amount adsorbed drops significantly following mercury entrapment. The cumulative incremental difference in amount adsorbed of argon and nitrogen for the same sample obtained from the difference between the isotherms before and after porosimetry is shown in Figure 5-4a. From the Figure 5-4a it can be observed that the curve for argon is generally at the same level for a vast range of relative pressure after the microscopic region, whilst for nitrogen, the incremental difference in amount adsorbed is mostly dropping at relative pressures after the area of the multilayer, and when the relative pressure almost exceeds 0.6, the decline of the curve is generally increasing. Similar to argon at the highest relative pressures near to one, the nitrogen curve starts to increase dramatically.

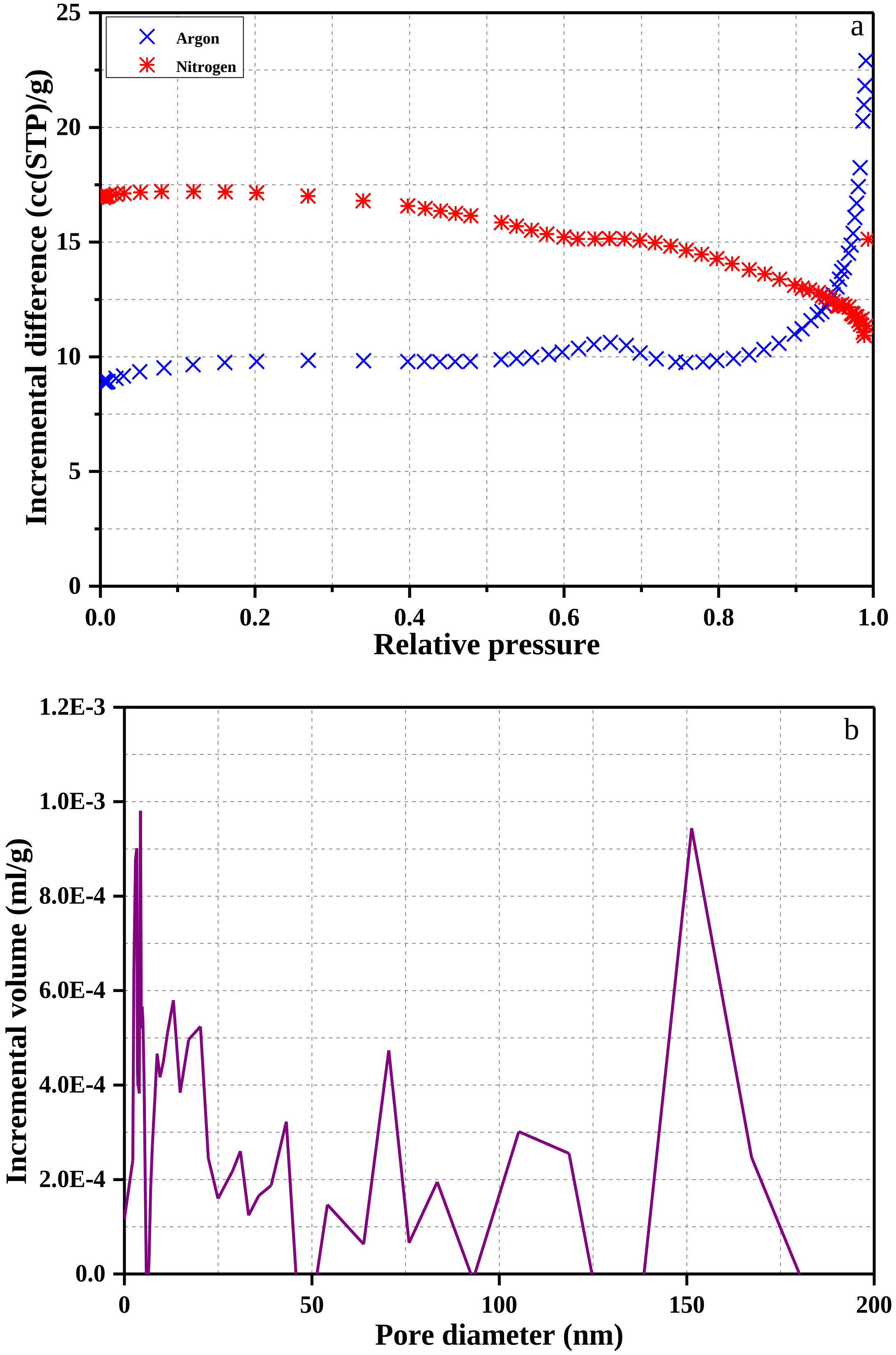

Figure 5-4: (a) Cumulative difference in amount adsorbed between gas adsorption isotherms obtained before and after mercury entrapment for nitrogen (✳) and argon (×) on Silica-alumina catalyst. (b) Distribution of pore sizes where condensation was impacted by mercury entrapment.

Figure 5-4b was derived from the data analysis of nitrogen presented in Figure 5-4a which displays the diagram of the pore size distribution expressed by volume within which capillary condensation was affected by the mercury entrapment. Hence, this represents the distribution of pores which have been converted from through-pores, initially connected to the macroporosity, to dead-end pores by entrapment. It can be seen that the largest peak corresponds to the largest pore sizes. For the argon sorption isotherm, the region of the multilayer adsorption before mercury entrapment was matched to the model of the homotattic patch isotherm (McMillan, 1947), consisting of patches obeying either a Langmuir or a fractal BET isotherm (Mahnke and Mögel, 2003). From the isotherm shape, it is clear that the micropores were filled at low pressure. The fractal dimension of the typical catalyst of silica-alumina obtained from the fractal BET model was 2.07 ± 0.01.

Besides the whole nitrogen boundary curves conducted by gas sorption on the typical sample of silica-alumina catalyst in addition a series of scanning curves, as shown in Figure 5-5, were obtained. It can be noticed from Figure 5-5 that the curves of the boundary adsorption and desorption had deviation at a relative pressure of 0.66 and 0.6, respectively. These relative pressures were the points where the scanning curves had started from, in addition to other points at the higher relative pressure of 0.85 and 0.90. From Figure 5-5a, it can be observed that the scanning curve on the adsorption boundary curve at a relative pressure of 0.66 takes a direct way to the boundary desorption curve, whereas the second scanning curve at a relative pressure of 0.6 comes in a long way down when it reaches the desorption boundary curve.

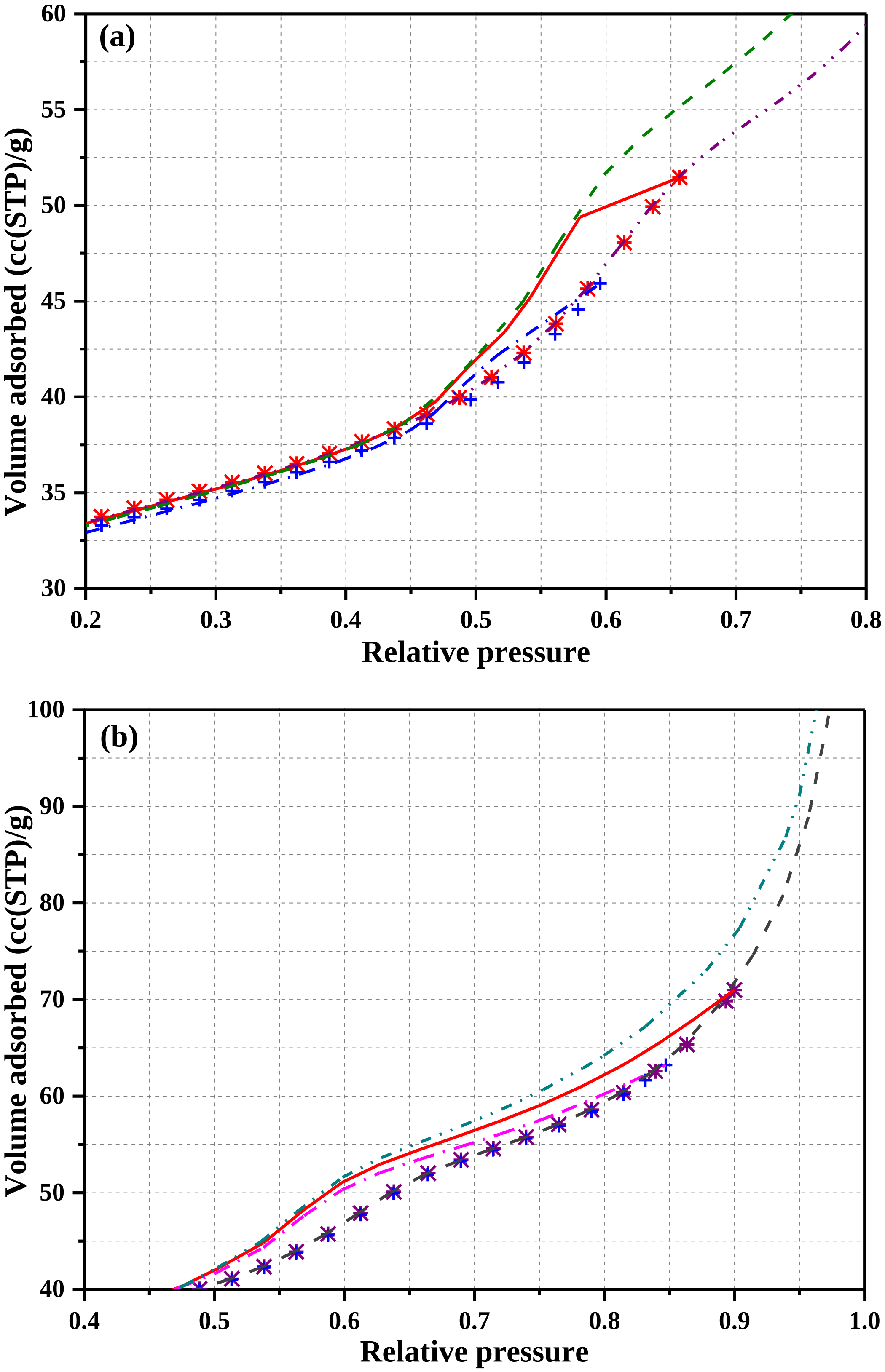

Figure 5-5: (a) Nitrogen sorption scanning curves up to relative pressures of 0.6 (+ and dot-dash line) and 0.66 (✳ and solid line), and boundary curves (dash-dot-dot line and dashed line). (b) Nitrogen sorption scanning curves up to relative pressures of 0.85 (+ and dash-dot line) and 0.90 (✳ and solid line), and boundary curves (dashed line and dash-dot-dot line).

From Figure 5-5b, it can be seen that both of the scanning curves at a relative pressure of 0.85 and 0.90 on the adsorption boundary curves descend away to the lower closure point of the hysteresis on the desorption boundary curve at a relative pressure of 0.60.

5.3.2 Mercury intrusion/extrusion porosimetry

The raw data obtained from mercury porosimetry for the typical disordered catalyst of silica- alumina is shown in Figure 5-6. Due to the similarity of the value obtained for the fractal dimension above for the silica-alumina catalyst with that for the controlled pore glasses (CPGs) used for the Washburn equation calibration by Kloubek (1981), the standard Kloubek (1981) was then applied to analysis the data using correlation parameters for the equation of the surface tension and contact angle in the Washburn equation as presented in Figure 5-6b (Rigby and Chigada, 2009). Figure 5-6b shows analysis of the data obtained from Figure 5-6a using the Kloubek correlations. It can be seen from the Figure that the intrusion curve overlaps the extrusion curve at intermediate pore sizes in the range of radii from ∼7 to 30 nm. The existence of a flat plateau appearing at the top of the intrusion curve suggests that all the mesopore network has entirely filled with mercury. It is also that a small flat region appeared at the beginning of the extrusion curve, indicating no mercury left the pores until the sharp first step, and hence some hysteresis kept even after excluding the contribution of the contact angle through the application of the Kloubek equation. The amount of the mercury extruded from the catalyst is less than that intruded for intrusion within the pore radii range from ∼30 to 100 nm, thus suggesting mercury is stuck within the largest pores.

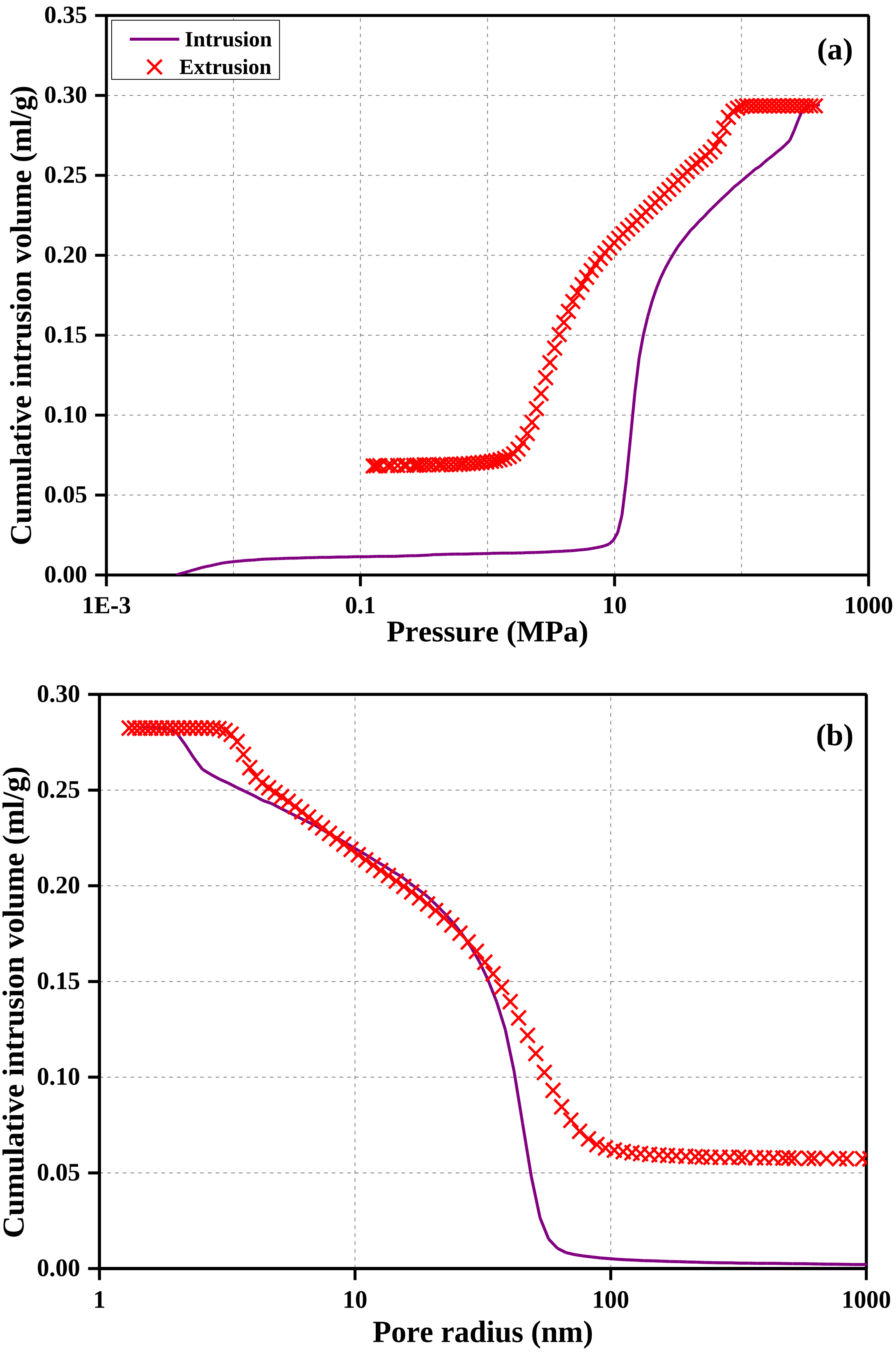

Figure 5-6: (a) Raw data mercury porosimetry for silica-alumina material. (b) Data calculated from (a) With inter-particle intrusion deducted and analysed using Kloubek (1981) correlations.

5.3.3 Computerised X-ray tomography (CXT)

Figure 5-7 shows two-dimensional images for a typical example of silica-alumina material, containing entrapped mercury, taken using the X-ray tomography instrument. The brightest white areas denote macropore regions occupied by the mercury. These regions are the same in typical shape and distribution to the formerly low X-ray absorbing macropores shown in Figure 5-1. Therefore, the CXT images suggest that mercury gets stuck in the macroscopic region of the pellets. It is also noticed that the intruded mercury in the catalyst has damaged nothing in the structure of the pellets. It can be seen that a penetration of the mercury within porous materials assisted the visualisation of disordered pores as characterised by the presence of different size of macropores.

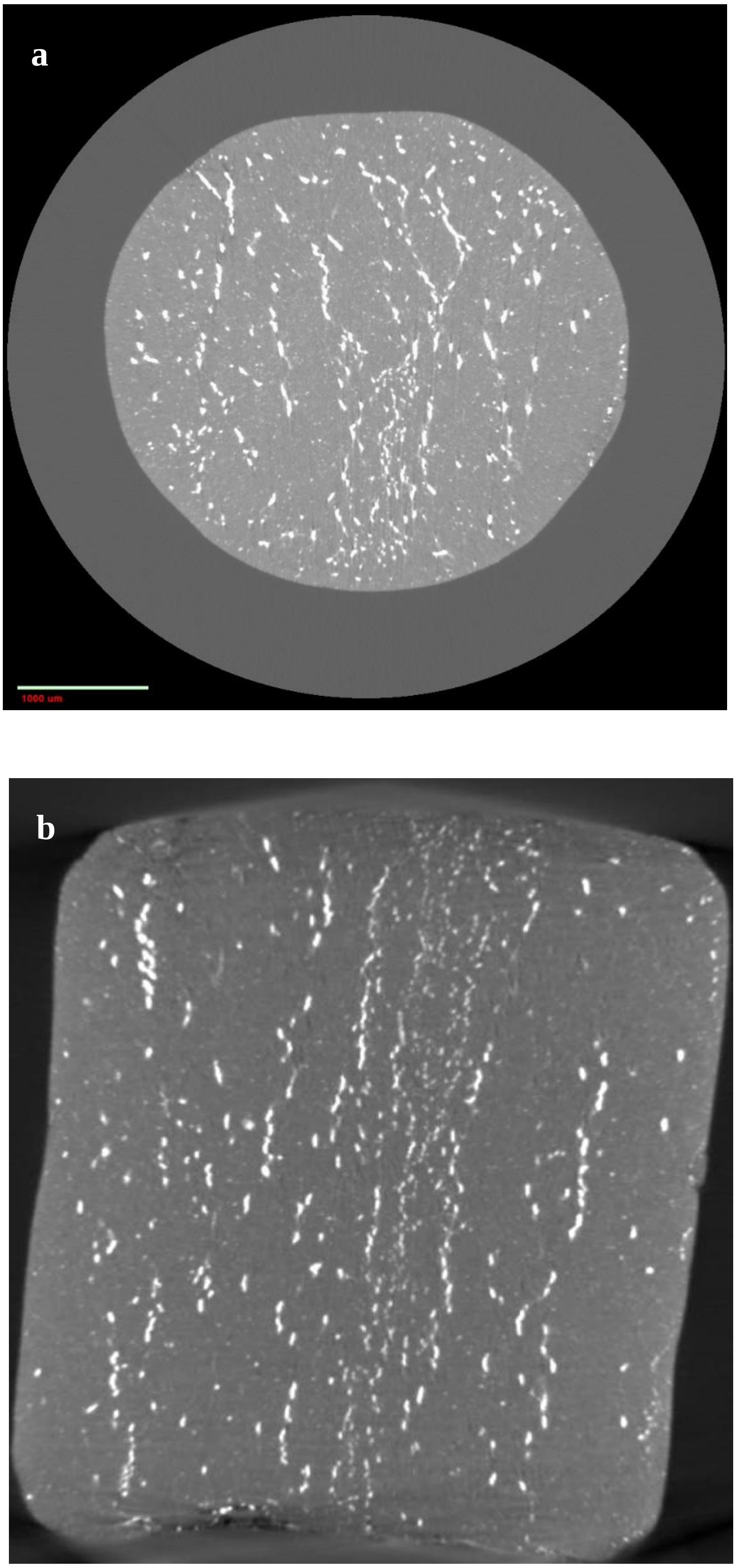

Figure 5-7: (a) Radial plane and (b) Axial plane CXT Images from a typical sample of Silica-alumina catalyst following mercury porosimetry. The brightest white pixels correspond to the highest density mercury-filled macroporosity and the mid-grey pixels correspond to a solid matrix. The scale bar corresponds to 1000 µm.

5.3.4 Mercury thermoporometry

Figure 5-8 shows the melting curve obtained from DSC thermoporometry for a catalyst sample of silica-alumina material following a mercury intrusion experiment. It can be seen from the figure that the bulk mercury melted at a temperature of -38.8 ℃. The melting peak in the DSC data is located at -39.5 ℃ and the factor of Gibbs-Thompson applied for mercury, aforementioned in the Theory part, suggests that entrapped mercury is existent as ganglia in the macroscope region. This analysis data supports what was suggested from the data obtained from CXT that entrapped mercury is only in the macropores within the pellet.

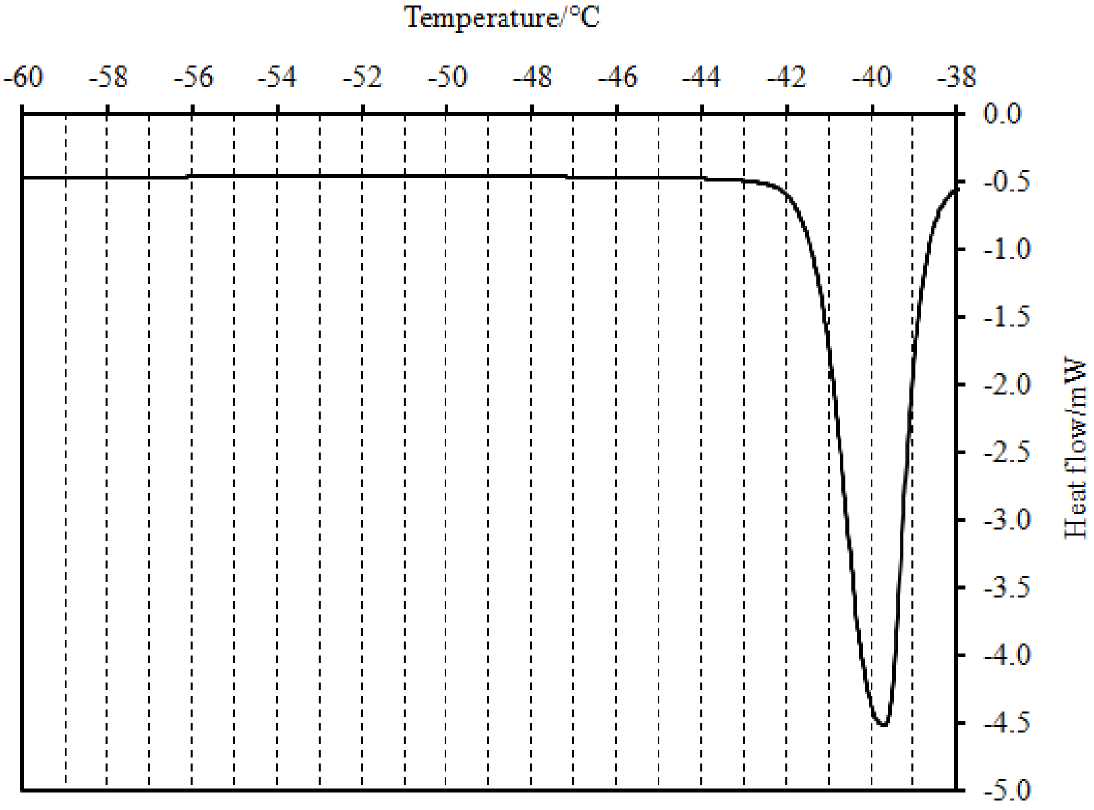

Figure 5-8: DSC thermoporometry melting curve for a sample of Silica-alumina catalyst following mercury porosimetry.

5.3.5 NMR cryoporometry

Figure 5-9 displays the boundary melting curves and melting-freezing scanning curve obtained by NMR cryoporometry for bulk water and water soaked within the pores of the silica-alumina material. The Figure 5-9 has revealed that the melting temperature of the water within the void space is different from that temperature for the bulk ice in the sample. From Figure 5-9, it is observed that at a given point on the boundary curve where the temperature increase is reversed, the distance between the melting and freezing curves, which is called hysteresis, is very narrow, being probably only ~0.5 K, and remains at the same distance until a temperature of ~269 K, where this hysteresis has extended to ~6 K when the temperature drops down to ~267 K.

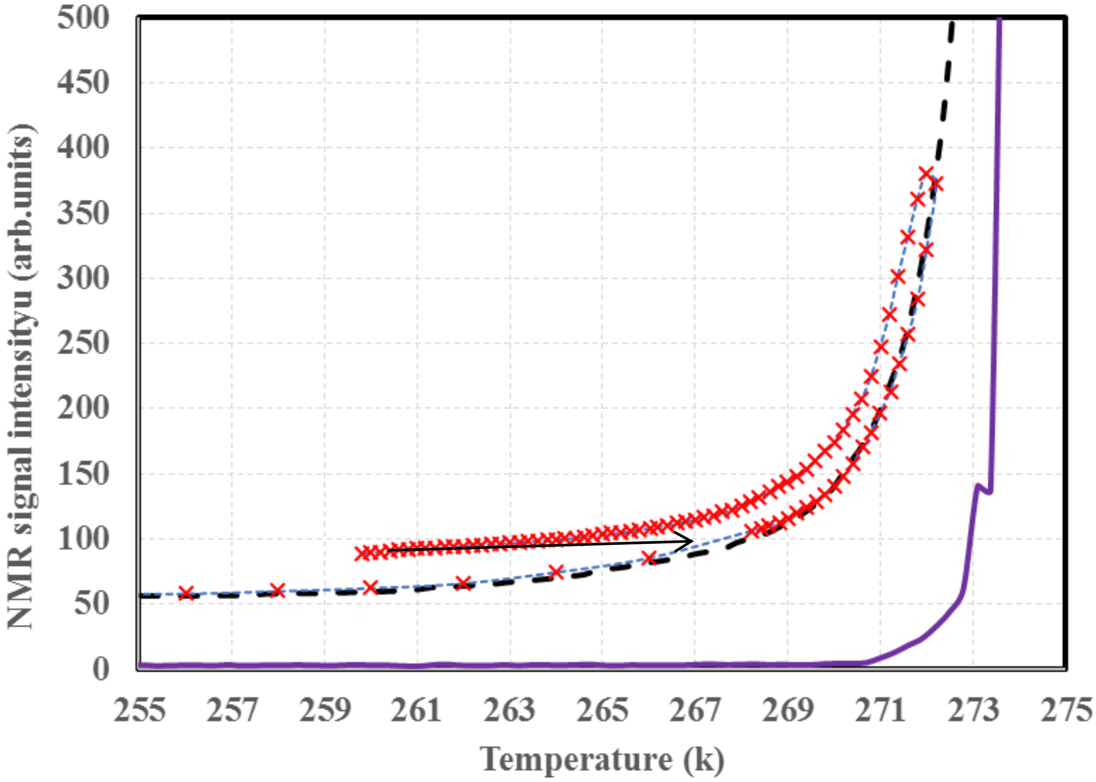

Figure 5-9: Boundary melting curves of the NMR cryoporometry for bulk ice (solid line) and water soaked within the porous network of the silica-alumina catalyst (dashed line). Also presented in a melting-freezing scanning curve (× and dotted line) up to 272 K. The double-headed arrow indicates that the width of the hysteresis between the freezing and melting branches of the scanning curve has grown to ~6 K at a melting temperature of 267 K.

Thus, at a temperature of 267 K, the depression of the melting point is about half that of the freezing point depression.

5.4 Discussions

Based on the results data obtained from DSC thermoporometry, using mercury as a probe liquid, and CXT conducted on the typical sample of silica-alumina material, it is suggested that mercury has a propensity to get entrapped in the very largest macroporous network in the sample. It has also been found that the plots of the incremental difference in amount adsorbed for argon and nitrogen are in agreement with the scenario described in the Theory section. The entrapped mercury in the macro-pores results in creation of block-ends effect at the junctions point between them and through- open pores. This newly created dead-end gives rise to a drop in the capillary condensation pressure for nitrogen, according to the Cohan (1938) equations. However, in the case of argon, the mercury created dead-ends has no effect on the condensation because argon is much less wetting of the entrapped mercury. At the lowest relative pressure, the value of the incremental difference in the amount adsorbed plots for both nitrogen and argon is quite high since both of them are being excluded from the micropores that fill at low pressure. This suggests that the mercury entrapped in the largest macropores then blocks a way to access the micro-porosity that fills at the lowest pressure, as presented in Figure 5-10. This suggests that the micro-porosity is perhaps surface roughness of the macropores.

The experimental data obtained from all of the mercury intrusion/extrusion porosimetry, nitrogen adsorption scanning curves and NMR cryoporometry scanning curve is in agreement with the graphic model of the pore system given in Figure 5-10. From the Figure 5-10b where the data had been analysed by the Kloubec equations, it can be observed that the hysteresis between the intrusion and retraction curves still appeared at the highest pressure, suggesting that there is another source of hysteresis in addition to contact angle difference. The plateau appeared at the top of the intrusion curve suggests that the mercury has filled all of the mesoporosity in the sample, and hence that it is probably all the mercury menisci created in the mesopores region would have coalesced. This means that the snap-off effect will be the dominant mechanism to create a new meniscus pair through the mercury extrusion process (Giesche, 2006). The significant reduction in the mercury pressure leads to the generation of the free menisci and thereby results in the creation of the residual hysteresis. In the experimental data above, the triangular form of the hysteresis area at a high pressure is matched with the data obtained from the simulations of intrusion/extrusion conducted by MF-density functional theory (MF-DFT) in a pore system in which the larger pores connect together to form small pores (Rigby and Chigada, 2009). The process of the snap-off is commenced in the small through-open pore.

Further, the change observed for the scanning curves of the gas desorption applied on the silica-alumina material, where the curves were declining, then crossing, and back to declining is also in agreement with the pore model exhibited in Figure 5-10. Figure 5-10 represents a simple model system in which the smallest pores start to be filled with capillary condensation through the cylindrical sleeve-formed meniscus. If the liquid condensate has filled the smallest pores within the network at the highest pressure of the scanning curve and the larger pores were still empty, the hemispherical meniscus-shaped was then generated at the junction connecting between the smallest pores and the neighbour larger pores to commence the desorption from the smallest pores. This based on the Cohan equations would lead to a broad hysteresis, and subsequently, a crossing scanning curve. This is what is noticed at the point where scanning curves have deviated from the boundary adsorption isotherms at a relative pressure of 0.66. While the condensate fills all of the smallest pores within the network, the medium pores can be filled by an advanced condensation via the hemispherical meniscus created at the closed ends of the smallest pores. If the smallest and medium pores fill with condensate at the highest pressure, and the largest pores are still empty, desorption, however, can commence from the junctions between the medium pores and the largest macropores, via the hemispherical menisci. Since the meniscus geometry for the adsorption is similar to that for the desorption, no hysteresis would be expected, and desorption would start immediately after the pressure of a scanning curve is reversed, and the scanning curve of the desorption would drop down to the lower closure point. This is consistent with the analysis data obtained from the actual sample for scanning curves turning around at relative pressures higher than the kink in the curve of the adsorption boundary. It is observed that the width of the hysteresis created for scanning curves is almost ranging from non-existent to narrow distance, and this is likely because of the high distribution in the sizes of pore, and divergence occurring in the pore geometry, that arises in actual materials, in contrast to the model shown in Figure 5-10.

Moreover, the data obtained from the NMR cryoporometry scanning curve is also in agreement with the pore system model presented in Figure 5-10. While the soaked fluid is fully frozen within the pore in the model, melting would then initiate from a meniscus of cylindrical sleeve shape at the boundary curve between the thin liquid surface layer and the frozen bulk in the smallest through-open pore. When this had melted, hemispherical-shaped meniscus would be generated at the junction connecting between the smallest pore and the neighbouring pores having medium size. These medium-sized pores would then melt via these hemispherical menisci. If the probe fluid within the smallest and medium-sized pores was completely molten but the largest pores keeping frozen then, once the temperature comes down, freezing could restart from the hemispherical-formed meniscus created at the boundary between the medium and the largest pores. Hence, the hemispherical-shaped menisci would be the responsible for both melting and freezing process occurring in the medium-sized pores, and hysteresis there would be not anticipated to appear. On the other hand, when the temperature had decreased enough for the smallest pores to freeze, freezing would occur within these pores via a hemispherical-shaped meniscus instead of the cylindrical sleeve-formed during melting, and thence hysteresis could be expected. Subsequently, narrow or no hysteresis would be found when melting and freezing of the probe fluid taking place in the medium-sized pores, while hysteresis could be anticipated during the melting and freezing occurring in the smallest pores. This type is similar to what was found in the experiment, whereby hysteresis was very little at the beginning of the freezing scanning curve, whilst this hysteresis became wider at the lower temperature once the smallest pores commence to freeze. It was noticed above that at the lower melting temperature of 267 K the depression of the freezing point was double that of the melting point depression and this difference of the factor is that was predicted for cylindrical through-open pores by Petrov and Furó (2006).

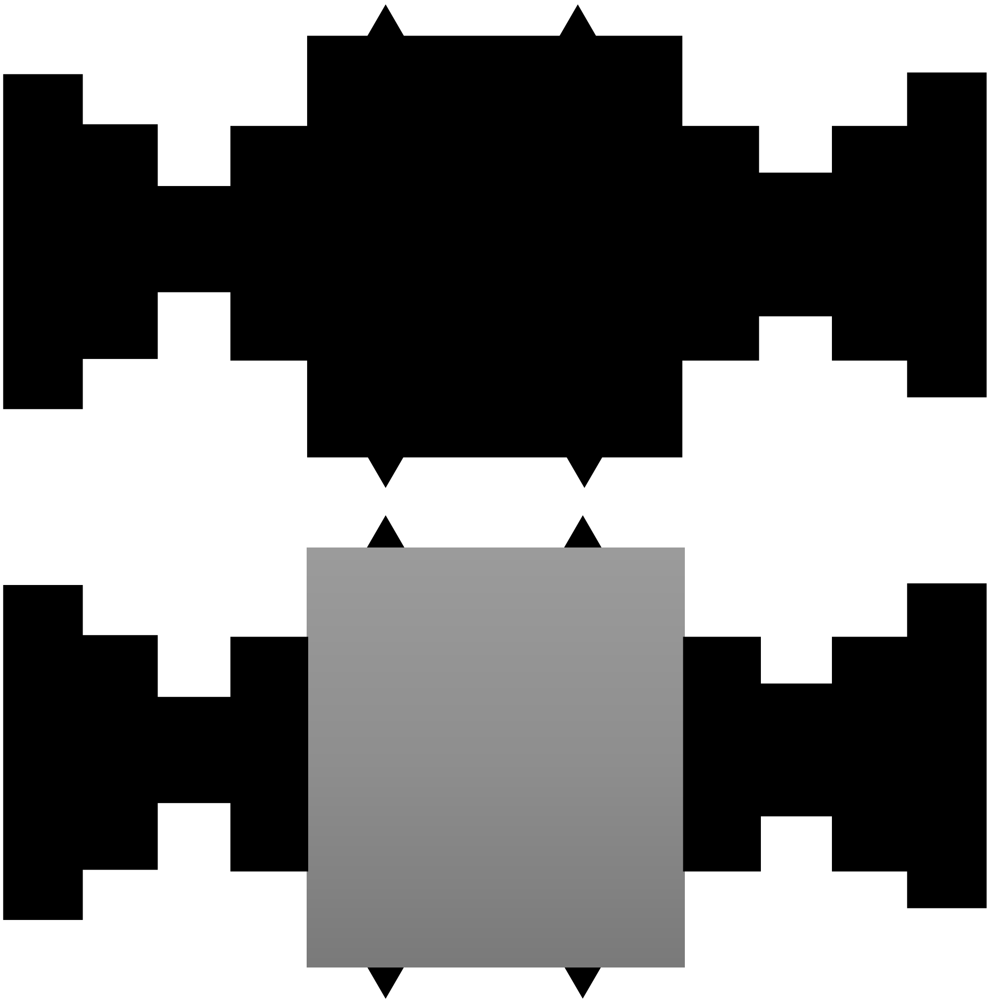

Figure 5-10: (a) Graphical diagram of proposed model for pore system of the silica-alumina catalyst, and (b) Proposed model for mercury entrapment (grey) in the pores (black). The rectangles represent through macro- and mesopores, and the small triangles represent dead-ended micropores formed by surface roughness in the macroporosity.

5.5 Conclusions

Based on the data obtained from mercury DSC thermoporometry and CXT experiments, it was found that mercury only becomes entrapped in the macroporosity of a silica-alumina material. It has been shown that nitrogen has the ability to wet a mercury surface, while argon does not. This difference in wetting between the two gases, results in a difference in the manner of capillary condensation following mercury entrapment. The difference assists in characterising the sub-set of mesopores neighbouring to the macropores and obtain its specific pore size distribution. A basic model for the pore network architecture of the pellet has been derived from gas sorption scanning curves and NMR cryoporometry data. It has been shown that the pore network structure is hierarchical with ever smaller pore leading off larger pores, much like the blood circulation network in animal bodies.

CHAPTER 6

ALUMINA PELLET

6.1 Introduction

A catalyst is commonly used in industry, especially in oil refineries to upgrade heavy oil and bitumen. Therefore, catalyst development is continuously required to improve their activity and chemical selectivity to obtain products with a higher specification. In order to achieve a high catalyst quality, a deep understanding of the internal structure of the pellet pore networks, a structure that directly affects the fluid behaviour within pellet, is required (Nepryahin et al., 2016a).

Several different methods, such as granulation, extrusion and pelleting, can be employed to form catalyst particles. Moreover, many parameters are considered during the production process of the catalyst, for instance, the ratio of the mould to particle size, kind and quantity of lubricant, and compaction pressure are taken into account in the production of catalyst pelleting (Nepryahin et al., 2016a) Further, different catalyst cross-sectional shape such as rectangular and triangular have been adopted in previous studies (Lenormand et al., 1983).

An experimental work tested porous glasses and porous silicon catalyst, using NMR techniques to study the internal geometry for mesoporous solids. Random pore networks have been etched on porous glasses in a hierarchical structure with a high pore connectivity, and for porous silicon consisting of clusters of isolated pores (Naumov, 2009). It was found that molecular transport within pores for porous disordered materials was dominated by two mechanisms. For a region outside the hysteresis, the relaxation dynamic was dominated by self-diffusion mechanism, while states within the hysteresis, an activated redistribution of the adsorbate in the pores controlled the relaxation process.

A simulator of mercury intrusion/extrusion, in pore system models, has been developed, using more advanced representations of the pore geometry (Tsakiroglou and Payatakes, 1998). The simulator integrated with a mercury porosimetry experiment, using two glass-etched pore models, to study the effect of fluid topology on mercury extrusion. Additionally, geometrical parameters of porous media, such as pore and throat sizes distributions, pore-pore interconnected, and spatial pore size correlations, were taken into consideration. Raw mercury intrusion and retraction curves obtained from an experiment were compared with the theoretical information extracted from the simulation. It was found that mercury randomly intruded the pore network in agreement with the random distribution of the pore size. Most of the mercury extruded from the pore network in a narrow range of pressure, which was extremely affected by the fluid topology. Further, a geometrical parameter such as mean pore size, in addition to the contact angle values of the intrusion and extrusion, had a strong effect on the position of the capillary pressure curves.

Another experimental study looked at the pore geometry effect and pore interconnections in sandstone rock samples, as well as in glass models, on mercury intrusion/extrusion capillary curves (Wardlaw and McKellar, 1981). In this study, chamber-throat correlated networks were used with random heterogeneities at different microscales. These heterogeneities can be found in sedimentary oil reservoir rocks which are mainly formed from sedimentation and diagenetic processes. It was noticed that mercury became extensively stuck in regions with large chamber-throat size ratios. Such pore networks are often found in carbonate rocks, including ‘vuggy’ porosity and in several types of sandstones involving secondary porosity.

In this work, the Computerized X-ray Tomography (CXT) technique was used before and after mercury intrusion-extrusion porosimetry. Mercury porosimetry is unable to provide information about the shape of the pore, pore distribution or the connection between pores. However, 3-dimensional imaging techniques such CX tomography provide such information, to determine the typical spatial arrangement of intruded mercury into the sample, and. It is also CXT can specify whether the pores are continuing along the sample or ending at a certain length.

CXT is a technique for obtaining the properties of the internal geometry of disordered porous materials. In this technique, several radiographic images from different angles can be obtained for the tested sample to create an entirely three-dimensional image. This would provide valuable information about the internal structure of the materials (Wildenschild et al., 2002). Over the years, CXT has been expanded to cover a wide range of applications in terms of the pore space characterisation such as a bulk density of the sample, water content, connectivity, tortuosity etc. (Anderson et al., 1990, Hopmans et al., 1992, Coles et al., 1998a). As will be explained in more detail below, in this study, mercury entrapped in alumina pellet sample will be imaged, using CXT following mercury porosimetry, to look at where mercury gets stuck in a sample. Many porous materials have pore structure involving similar pore sizes within a certain area but have completely different properties from the pore network present in other regions. The mercury entrapped within pellet can correlate with the shape of pore geometries, and whether there are any interconnections between pores or not.

6.2 Materials and methods

6.2.1 Materials

A porous alumina pellet was used in this experiment. It had the shape of a cylinder with a diameter of 10 mm, length of 11.5 mm, and it had four small holes with a diameter of 2 mm for each as illustrated in Figure 6-1. Figure 6-2 shows CXT images of radial and axial plane cross-sections for a typical sample of alumina pellet. The dark spot forms in the image are macropores within the body of the alumina pellet. It can be seen from the spatial distribution of macroporous that the size of the pores is different from one pore to another.

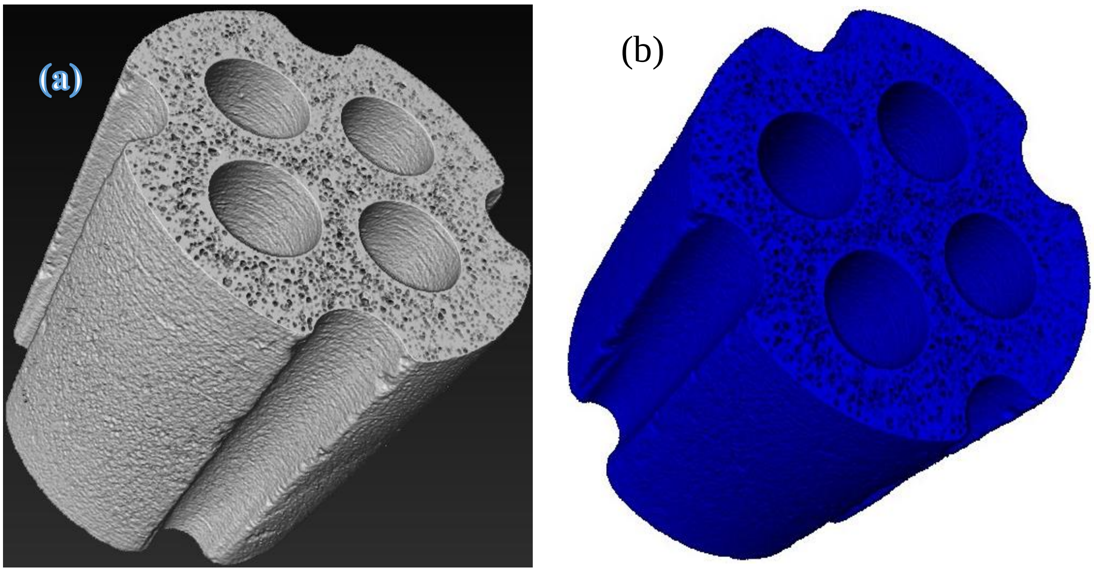

Figure 6-1: A 3D reconstruction CT image of a typical sample of alumina pellet.

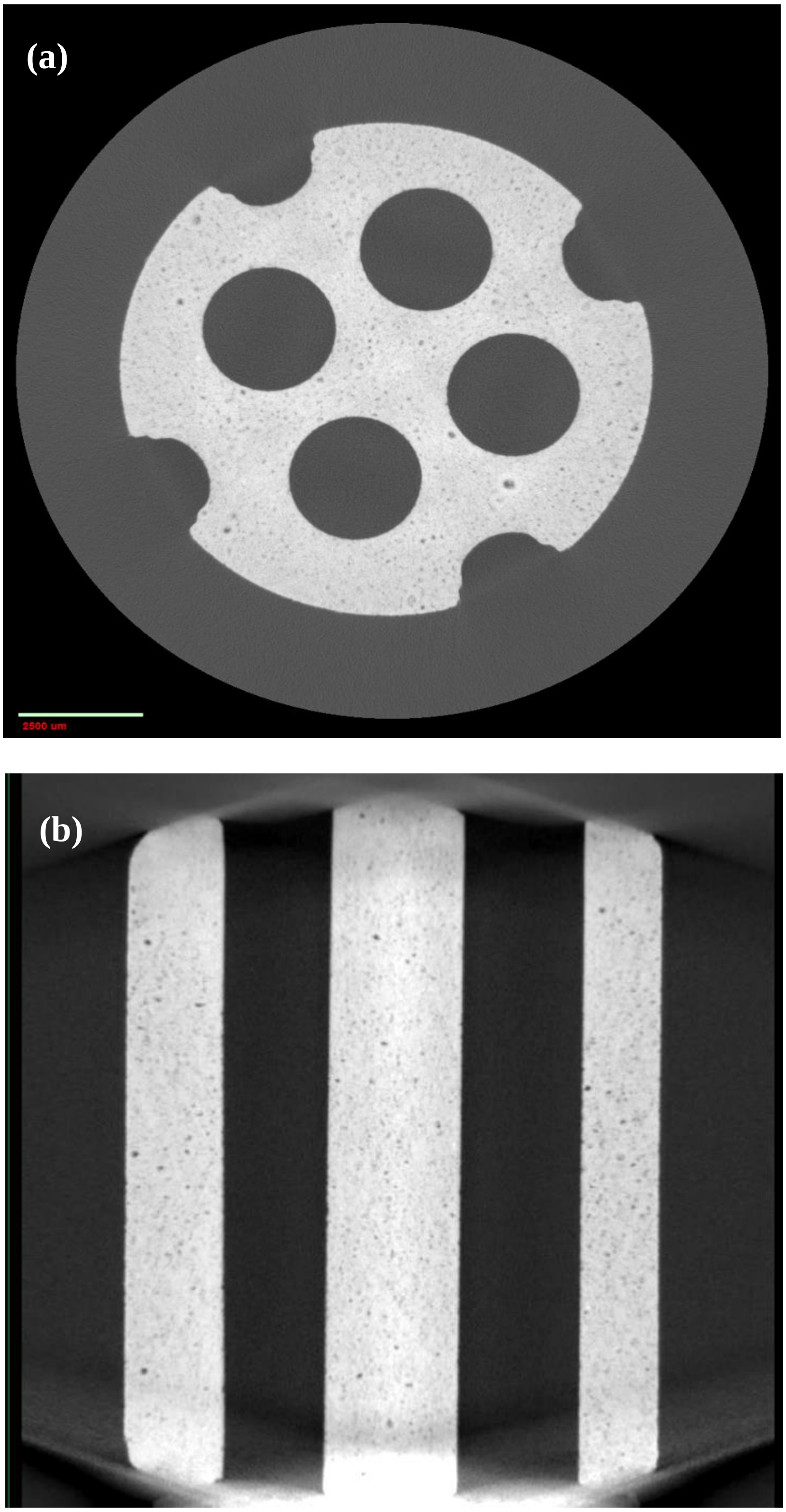

Figure 6-2: (a) Radial plane and (b) Axial plane CXT images of typical cross-sections through a sample of alumina pellet. The dark spots correspond to porosity.

6.2.2 Computerised X-ray tomography (CXT)

The sample before and after mercury entrapment (obtained from mercury porosimetry experiment) was imaged using 3D Computed X-ray Tomography Microscope Apparatus of model VeraXRM-510 provided by Xradia Inc, Pleasanton, CA, USA, with high resolution of 5.5 μm.

6.2.3 Mercury intrusion-extrusion porosimetry

The experiment was carried out on a Micromeritics Autopore IV 9500 mercury porosimeter (using 99.99% Hg), including a pressure range from 0.01 to 414 Mpa. The apparatus had two ports for low pressure and one for high pressure, which allows performance of the analysis for more than one sample at the same time. The instrument measured the volume intruded by mercury over each increment in the imposed pressure. The mercury experimental data were analysed according to the standard Washburn equation, and the values of mercury surface tension and the contact angle were 0.485 Nm^{-1} and 130° respectively for both the advancing and receding menisci to obtain the intrusion and extrusion curves. The applied standard equilibration time used here for every pressure step was 15 sec. The penetrometer used to perform the experiment was calibrated by running it blank to minimise baseline error, caused due to compressibility and heating through the analysis. The appearance of any intrusion during the blank run can be attributed to the baseline error and was subtracted from the subsequent sample run. The sample, before any experiment, was first dried under vacuum to a temperature of 140 °C for six hours to drive any physisorbed water out the sample pores. The dried sample was loaded and sealed in a penetrometer using a thin layer of vacuum grease over the top edge of the penetrometer. Thereafter, as a first step, the sample was attached to the low-pressure port using a light coating of silicone grease around the external surface of the penetrometer. The process was controlled and monitored by a computer attaching to the instrument. All the process conditions and sample information were recorded in a created file on this computer. In the first stage, the sample was evacuated to a pressure of 6.7 Pa to remove any traces of water content on the porous sample. The evacuation stage must be perfectly enacted to avoid uncertainty in the results and contamination troubles. The pressure then increased up to ambient. After that, an assembly weight (penetrometer, mercury and sample) was taken prior to transfer to the high-pressure step. In the high-pressure process, the pressure was raised incrementally up to a maximum of 60,000 psi (414 Mpa). At the end of the high-pressure process, the pressure was gradually reduced allowing the mercury to extrude from the disordered material stepwise, creating an extrusion curve.

6.3 Experimental Results

6.3.1 Mercury intrusion-extrusion porosimetry

Figure 6-4 shows the raw mercury porosimetry data for an alumina pellet, with the final imposed pressure of 414 Mpa. From Figure 6-4, it can be seen that at very low pressures all the spaces between the particles were entirely filled, creating a long horizontal intrusion curve before it rose rapidly after a further increase in the applied pressure. Once the pressure reached around 1 MPa, mercury started to occupy the intra-particle space and continued intruding until the maximum pressure of 414 MPa was reached allowing all of the pores to be filled generating a flat plateau at the top. This horizontal plateau suggests that the mercury penetrated all the pores at the highest pressure. An estimation of the total volume of the sample macropores penetrated by mercury can be obtained from the mercury intrusion curve. The volume of the intruded mercury, located between the end of the whole long horizontal plateau and the top plateau, represents the total macropores volume. As the pressure was reduced, a flat plateau curve appeared and continued, keeping the same mercury volume, before mercury left the sample until a pressure of around 2 MPa. The mercury then sharply extruded from the sample until 1 MPa before its extrusion volume became constant with about 0.03 ml/g entrapped.

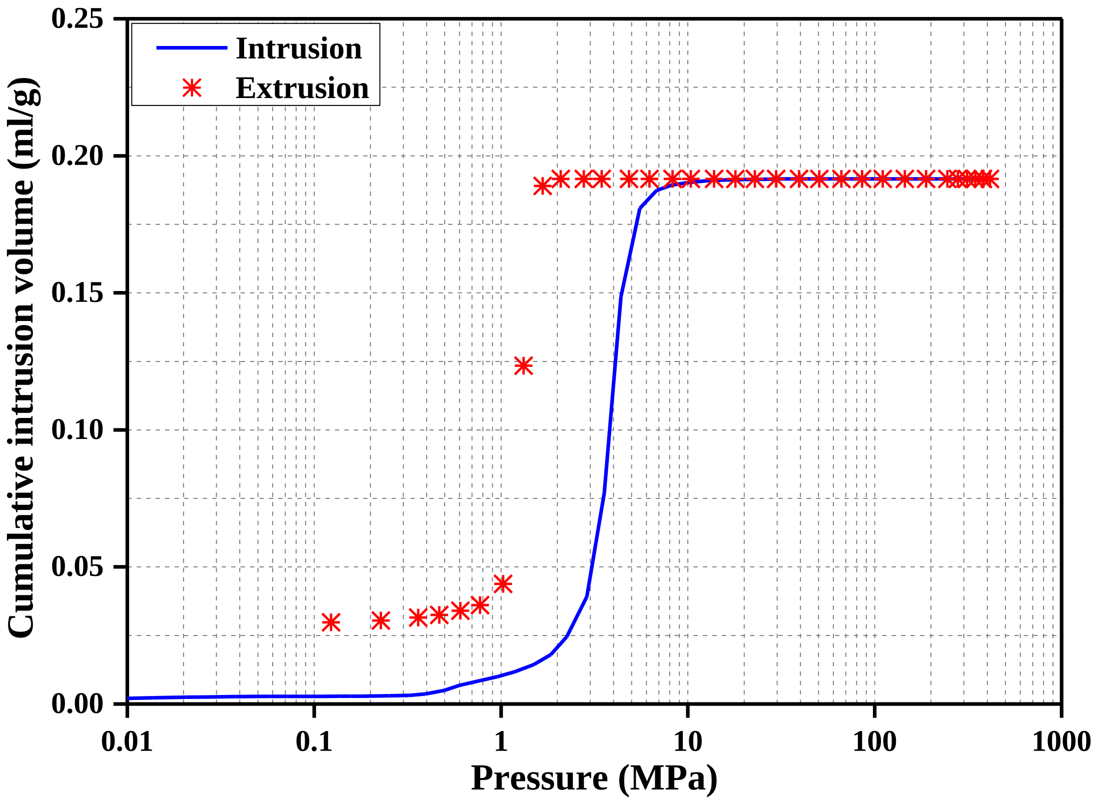

Figure 6-3: Raw data mercury porosimetry for alumina material.

The raw data obtained from mercury porosimetry presented in Figure 6-3 was analysed using the standard Kloubek correlations (1981) as shown in Figure 6-4. It can be seen from the Figure 6-4 that the intrusion curve overlaps the extrusion curve at intermediate pore sizes in the range of radii from ~100 to 200 nm. Based on the flat plateau appeared at the top of the intrusion curve, all the pores have been intruded by mercury. It can also be seen there is another plateau appeared when the extrusion curve started, which is completely matched on the first one, indicating no mercury left the pores till the pore radius of ~100 nm. Most of the amount of the intruded mercury extruded from the pellet except a little amount has been kept within pores of the catalyst as presented by the small hysteresis at pore with a radius of ~200 nm. Therefore, it is suggested that mercury is stuck in the largest pores. The hysteresis left over after the raw data analysed by Kloubek correlations can be observed in most porous materials, and, the nature of the pore geometry can cause this form of hysteresis.

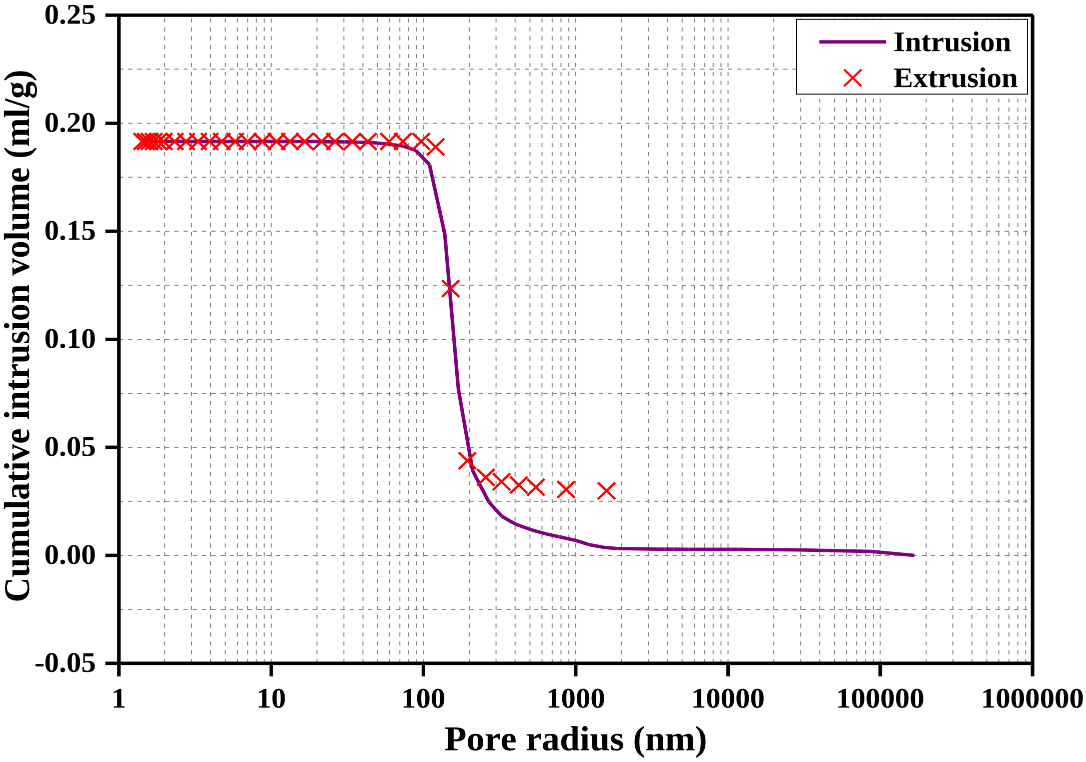

Figure 6-4: Data calculated from with inter-particle intrusion subtracted and analysed using Kloubek (1981) correlations.

6.3.2 CXT imaging

Figure 6-5 shows two-dimensional CXT images for a typical example of alumina material, containing entrapped mercury. The brightest white areas denote macropores regions occupied by the mercury. These regions are the same in typical shape and distribution to the formerly low X-ray absorbing macropores shown in Figure 6-2.

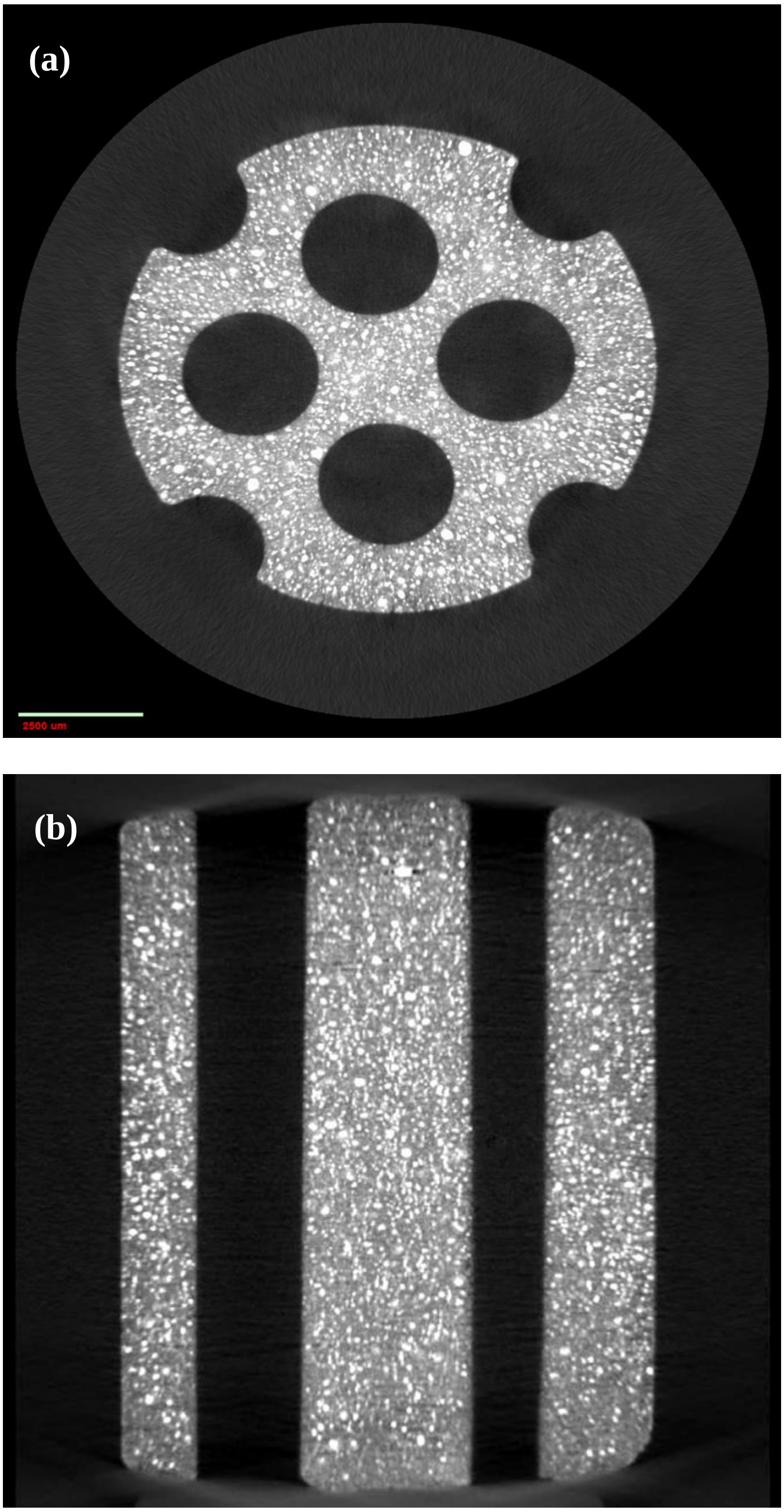

Figure 6-5: (a) Radial plane and (b) Axial plane cross-sections CXT Images from a typical sample of alumina pellet catalyst following mercury porosimetry. The brightest white pixels correspond to the highest density mercury-filled macroporosity and the mid-grey pixels correspond to a solid matrix.

Subsequently, the CXT images revealed that mercury occupied the macroscopic pores of the pellets. It is also observed that the internal structure of the pellets was not affected by the mercury entrapment. It can be seen that the sample has various sizes of macropores which are entirely isolated and there is not any macroporous connection between them. Hence, the large macroporous, in the CXT image, are shielded by the necks evident in the mercury intrusion curve.

A full 3D CXT reconstruction has been created by gathering many slices, which has been imaged by CXT, via a program called Avizo software as illustrated in Figure 6-6. It can be observed the shapes and the pore sizes that represent the internal geometry of the typical alumina catalyst. As can be seen from the Figure 6-6b that the pores are in different macroscale sizes, and are completely isolated. Additionally, the lengths of the pores are very short, thus giving the appearance of a spherical shape.

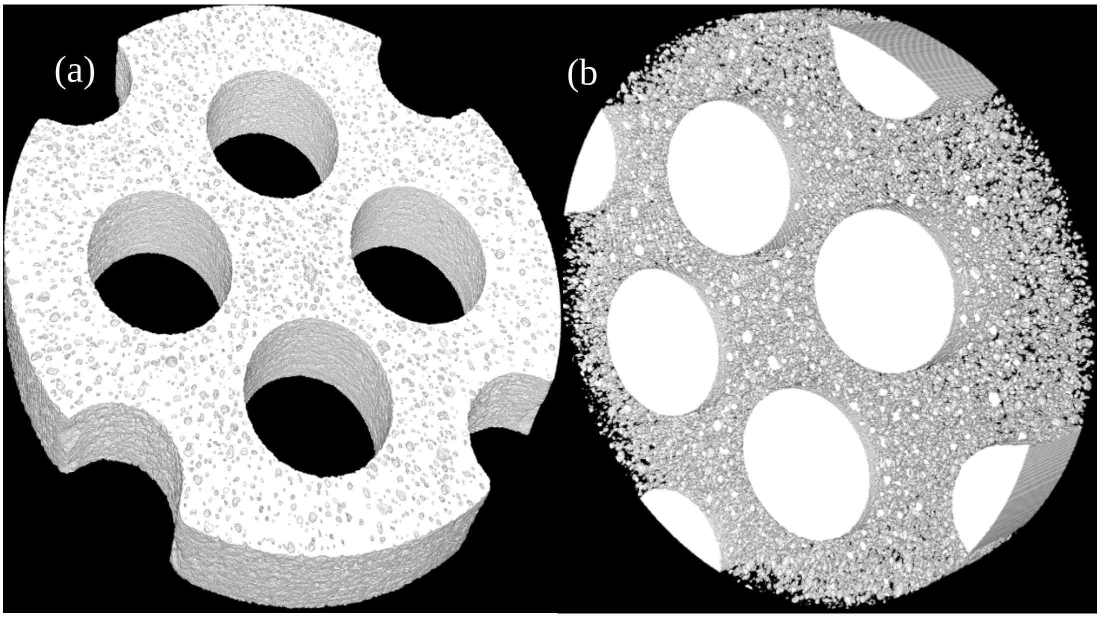

Figure 6-6: A 3D CXT images processed with 'Image Software' (a) Solid shape and (b) 'Inverse' image with pores volume filled.

6.4 Discussions

Figure 6-5 illustrates an alumina pellet with different isolated pore chamber sizes, connected to narrow throat sizes which are obviously detected by Figure 6-4 in the range from ~0.05 to ~100 nm. It is suggested that when the pressure was progressively decreased, and during the emptying of the pores, a phenomenon of snap-off occurred within pore necks resulted in an extensive trapping of mercury in the large pore spaces. These findings are in alignment with that obtained from a glass model proposed by Wardlaw and McKellar (1981), in which four different pore sizes randomly etched in a square network including seven isolated vuggy pore chambers. Tsakiroglou et al. (1997) support this suggestion where they found that snap-off led to the disconnection of mercury during its extrusion from a pore network, which was caused by large ratios of large pore body size to throat size. This phenomenon occurred in the throats resulting in high amounts of the mercury left in the pore network. As a consequence, this catalyst which involves a pore throat-body network will probably coke up easily as necks between macropores may block, and thereby, it will not be appropriate to use in THAI-CAPRI process.

6.5 Conclusions

In combination with CXT imaging, mercury intrusion/extrusion porosimetry can be used to evaluate the internal geometry and visualize the macroscopic-scales of porous disordered material. The technique has been employed to analyse the internal structure of an alumina pellet. The findings obtained from the CXT have been processed with an Aviso Image Software, creating three-dimensional images for the internal structure of the catalyst. It was noticed that mercury entrapped within a macroporous alumina pellet.

CHAPTER 7

SIMULATION RESULTS

7.1 Introduction

Thermal methods are used frequently for oil production from heavy oil reservoirs. The In-Situ combustion (ISC) technique is one of these methods; it has been used for over 80 years in a lot of fields around the world. ISC is considered the most commonly used of the valuable thermal processes because no external energy source for the process is required. Injected air, used in the in-situ combustion, helps to burn part of the crude oil generating heat which lowers oil viscosity and causes high cracking rates of heavy oil located in front of the combustion zone. The cracking of the crude oil leads to in situ upgrading of heavy oil. This feature is considered the most important advantage of in situ technique compared to the other EOR techniques (Thomas, 2008, Shah et al., 2010).

However, this method has several disadvantages. One of these drawbacks is that the ignition inside the well can happen spontaneously. Because of this spontaneous ignition, the consumption of the oxygen will occur close to the injector, and the process will be changed by this feature into forwarding combustion (Karimi and Samimi, 2010). Also, because the oxygen is exhausted near to the injection well, which causes a deficiency in the oxygen supply, it will be difficult to reach a high-temperature combustion mode, which makes it difficult to maintain the combustion (Alvarado and Manrique, 2010).

In addition, the conventional ISC technique uses a vertical injector and a vertical producer in which hydrocarbons need a long time to travel from the injector well to the producer well. These operational patterns suffer from some considerable problems, such as gravity override of gas, and the production of heavy oil from the reservoir can be affected by these problems (Kulkarni and Rao, 2004).

The Toe-to-Heel air injection technique (THAI) is a process in which the heavy oil production rate can be increased dramatically. This method is an advanced ISC technique, which combines the conventional ISC technique with horizontal producer wells, instead of vertical producer wells as in the conventional methods. The reason for this is to avoid the long distance between the injection wells and the production wells, to keep combustion advanced ahead from the “toe” to the “heel” within the producer well. The THAI process is designed to operate in a way involving stabilization of the drainage by gravity, which is restricted to a narrow mobile oil zone, which will travel along the horizontal production section. This short distance between the injector and the producer causes direct transferring of the mobilized fluids to the production well (Greaves et al., 2005).

The THAI process for enhanced oil recovery follows the same basic mechanism as for the in-situ combustion technique. Part of a heavy residue is burned by air via the injection well, producing heat to increase the temperature of the heavy oil, which causes a high reduction in the oil viscosity; as a result, the mobility of the oil will be increased. The thermal cracking reaction of the heavy oil produces fuel (mainly coke) which will be generated ahead of the combustion advance. The amount of this coke cracked is a very significant parameter to sustain the combustion propagation (Xia and Greaves, 2001).

Xia et al. (2002) have conducted a set of 3D experimental evaluations of THAI for upgrading of the Wolf Lake oil with API gravity of 10.5° and Athabasca Tar Sand

Bitumen with API gravity of 8^{o}, both originating from Canada, using different well configurations as follows: vertical injector/horizontal producer (VIHP) and horizontal injector/horizontal producer (HIHP) wells in direct line drive, and staggered line drive of vertical injector/two horizontal producer (VI2HP) and two vertical injector/horizontal producer (2VIHP). It was demonstrated that the horizontal injector/horizontal producer (HIHP) was the most effective for obtaining quick start-up, which means that the required time for commencing propagation of the combustion front is very short.

Further previous work using different wells configurations includes simulation by Fatemi et al. (2009) to evaluate the effects of several parameters regarding injector-producer wells arrangement, namely the distance between the positions of the wells, the depth of the injector and the length of the horizontal producer, on the performance of THAI technique in reservoirs including heavy crude oil. A 3D combustion cell, employing the CMG-STARS simulator, has been applied in this study for the heavy oil carbonate reservoir in Iran named Kuh-E-Mond (KEM). It was noticed that significant parameters, such as depth of injection, horizontal producer length, and the distance between injectors, should be taken into account, in order to fulfil the highest performance in the THAT process. The findings revealed that the best configurations of field scales are the 2VIHP and VIHP schemes.

An experimental work on in-situ combustion (ISC) was performed on the heavy oil of the Orinoco Belt in Venezuela using combustion tube by Anaya et al. (2010) , to investigate the technique performance. The scale laboratory results, obtained from the combustion tube experiment, were simulated to scale the laboratory tests up to full field scale. Several different well configurations were considered for the numerical

ISC simulation, taking into account distances between the injector and the producer, to determine the most favourable positions of injection and production wells. The distances were 50 m, 100 m and 200 m, with a constant rate of air injection of ~7063 m^3 min^{-1}. It was found that the suitable distance between the injector and the producer, to operate the experiment in the field, was 100 m. The findings revealed that the model, in which the distance between the injector and the producer was 100 m, gave high recovery factor and delayed gas breakthrough.

Moreover, a catalytic reactor can be integrated into the THAI technique to be a very effective method to upgrade crude oils prior to the refinery. Catalytic-Processing In-Situ (CAPRI) upgrading of high molecular weight hydrocarbons using ISC provides the possibility of increasing the extent of the improvement process of the heavy oil in situ (Abu et al., 2015). The way of using this technique is to attain further upgrading of heavy oil by covering a perforated horizontal producer by a given layer of catalyst (Greaves, 2000, Xia and Greaves, 2001).

In the THAI process, the cracking reaction, created due to the high temperature within the mobile oil zone (MOZ), generates the coke precursor for the CAPRI process (Shah et al., 2011). The MOZ involves mobilized oil, water as steam, unconsumed oxygen and gases produced from the combustion process including a small amount of carbon monoxide at high temperatures in the range of 450-650 ℃ (Xia et al., 2003). The gases produced from the combustion reaction operations are given by the following equations (Hart et al., 2014):

$$\text{Heavy oil} \rightarrow \text{light oil} + \text{gas} + \text{coke} + \text{absorbed heat} \qquad (7\text{-}1)$$

$$\text{Coke} + O_2 \rightarrow H_2O + CO_2/CO + \text{heat} \qquad (7\text{-}2)$$

Heavy oil + $O_2 \rightarrow H_2O + CO_2/CO$ + heat (7-3)

Light oil + $O_2 \rightarrow H_2O + CO_2/CO$ + heat (7-4)

It is thought that heavy oil is upgraded by a hydroprocessing operation in which carbon-rejection reactions are integrated with the addition of hydrogen at the catalyst surface (Shah et al., 2011). According to Hajdo et al. (1985), the hydrogen used in the process could be provided via a gasification process and/or the water-gas-shift reaction. The THAI-CAPRI technique is considered environmentally friendly because it makes the heavy oil free of undesirable contaminants. The method is a new technology which offers the significant feature of a combination of enhanced oil recovery process simultaneously with the catalytic upgrading of immobilized to mobilized oil (Hart et al., 2013).

Experimental THAI-CAPRI work has been conducted by Shah et al. (2011), using different catalysts to optimize the catalyst type and to find the favourable conditions for use of this technique. A microreactor was employed to perform this experiment, utilizing different temperatures, pressures and various gas media. Alumina-supported CoMo, NiMo and ZnO/CuO catalysts have been tested. It was found that the improvements of the API gravity, and the reduced levels of the viscosity, are dependent upon the flow rate of the oil and the temperature. It was also noticed that, at high temperature, more upgrading could be achieved, but that led to reduction in the lifetime of the catalyst bed. On the other hand, decreasing the temperature has led to a longer catalyst-bed lifetime, but the upgrading levels of the produced oil went down. Therefore, a balance in the operating temperature, between upgrading performance and the lifetime of the catalyst, is required to achieve acceptable consequences.

Hart et al. (2014) have experimentally tested a different type of gas in the THAI-CAPRI method to investigate the effects of the gas environment, using CoMo catalyst supported by γ alumina. Heavy oil has been utilized with API gravity of 14°. It has been found that the reactions of the hydrocracking and hydrogenation occurring in THAI process were promoted when hydrogen gas was used. Employing hydrogen gas gave rise to an API gravity of the produced oil 4° above the original value of the API of the feed, which was the highest number for the different gases level. Further, using hydrogen gas results in a higher reduction in the viscosity and higher conversion of heavier hydrocarbons, with a high boiling point, to lighter fractions, with a lower boiling point. Moreover, it was noticed that hydrogen media leads to convert unsaturated to saturated components as well as enhance the productivity of the saturated hydrocarbon.

A numerical THAI-CAPRI model has been simulated by Rabiu Ado (2017) at laboratory scale to investigate the catalyst activity on the heavy oil upgrading, using the same dimensions of the 3D combustion cell used in Greaves model. The effect of the frequency factor of the reaction on several parameters, such as oil rate, cumulative oil production and the API gravity, has been demonstrated. It was found that slight differences in the peak temperature were observed between the various values of the frequency factor, where during the combustion period, the maximum variance in the temperature difference was 40 ℃. It is also found that the increase in the frequency factor has led to the increase in the production rate.

Further studies are needed to further understand the THAI-CAPRI technique. In this study, more parameters, such as catalyst thickness, catalyst packing porosity, will be investigated. In addition, the effect of the ratio of hydrogen to air will be taken into account in this project. Additionally, this present work aims to simulate the effect of different well configurations on the performance of the THAI process applied at the laboratory scale. Two horizontal injectors and two horizontal producers (2HI2HP) were employed in different well configurations. Three different locations of the injectors and producers were simulated to look at the effects of the various places of the wells on the THAI process performance. Several parameters such as oil recovery factors, combustion front temperature, oxygen profile and solid phase (coke), have been tested on the THAI technique to choose the best configuration of laboratory scale.

7.2 Methodology

In this work, the Greaves model (Greaves et al., 2012) was adopted, a numerical CMG STARS model developed to carry out the simulations. A 30 × 19 × 7 (i, j, k) gridblocks experiment scale model was applied using Virgin Athabasca oil sand data, as reported by Greaves et al. (2012). The API of the oil was 8° with specific gravity 1.0143. The measurements of this 3D rectangular combustion cell are 0.6 m long, 0.4 m wide and 0.1m deep, using two horizontal injectors (2HI) and two horizontal producers (2HP) which were positioned in different schemes. Real reservoirs are continuous and all flow factors, which depend on the time, change constantly. Because of this continuous change of fluid properties, a reservoir simulator cannot solve these variables. Therefore, the continuous reservoir has to be divided into finite size elements and this division is indicated as the reservoir discretization. Each element of the group is called a reservoir grid or a cell. The STARS software includes the discretised wellbore (DW), which allows the fluid and the heat flow in the wellbore and between the wellbore and the reservoir to be accurately modelled. All types of equations, wellbore mass, energy conservation and chemical reactions equations are combined together and solved by the software in each wellbore part, using fully implicit finite difference method. However, to solve these equations, several reservoir input parameters are required. The original geological parameters used in this simulation (porosity, vertical permeability and horizontal permeability of the cell) are given in Table 7-1, and the relative permeability curve can be seen in Figure 7-1. PVT data used in the THAI process is reported in Table 7-2. The initial gas and oil saturation were 0.15 and 0.85, respectively, and the initial water content has not been considered. The air was used alone (known as dry combustion) with a flow rate for the air injection of 8000 cm^3 min^{-1}, which corresponded to 12 m^3 m^{-2} h^{-1}, at the beginning of the run, when pre-heating was finished. Then, depending on the pre-heating time, the air flow was increased to 10667 cm^3 min^{-1}, which is equivalent to a flow rate of 16 m^3 m^{-2} h^{-1}, and continued at this rate until the end of the simulation.

Table 7-1: Geological parameters of the rocks.

So (%)	Sw (%)	Porosity (%)	Vertical permeability (md)	Horizontal permeability (md)
0.85	0.15	0.34	2300	11500

Table 7-2: PVT data applied to this project.

Component	Mol fraction (%)	Molecular weight (g mol^{-1})	Critical pressure (kpa)	Critical temperature (℃)	Density (kg m^{-3})
Light component	36.47	170.0	2305.95	425.16	903.8
Heavy component	63.53	878.0	1031.29	780.0	1012.07

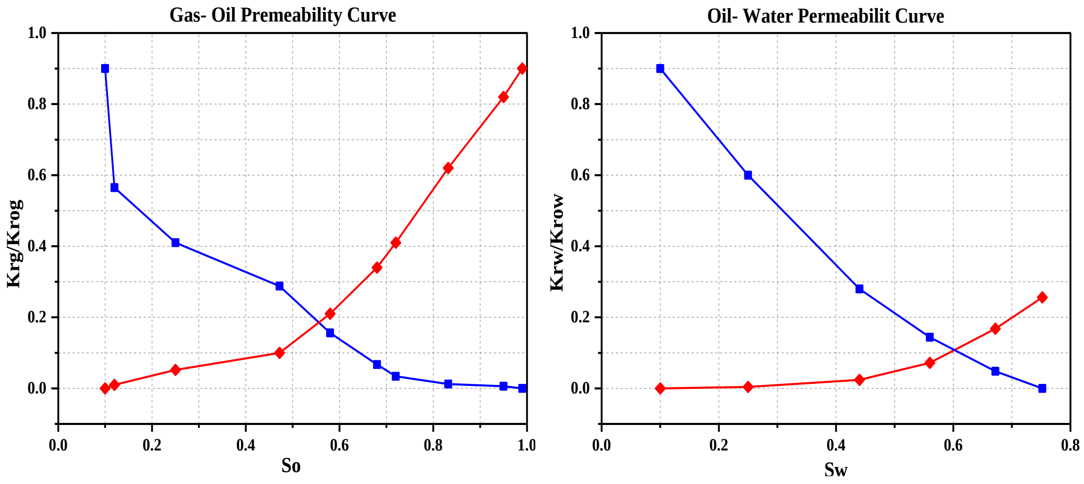

Figure 7-1: Relative permeability of Athabasca bitumen.

In order to make sure all parameters are in consistency with Greaves model (the original model), the total rate of the injected air for one injector in the Greaves model was equally divided between the two well injections in this study.

7.3 Simulation results for the THAI Process

7.3.1 Configurations effect of the wells

A numerical simulation has been carried out in this work using two horizontal injectors and two horizontal producers in different well configurations. In each well configuration, the injectors and the producers have been put in different locations, therefore the different designs of the injectors and the producers' positions are very important in this work. The configurations of the well were arranged as follows:

The first well arrangement, A1, was that the first injector, I1, was placed on the top horizontal layer while the second injector, I2, was placed on horizontal layer two rows directly under I1, and the producers, P1 and P2, were positioned on the horizontal layers five and six rows perpendicular to the injectors as shown in Figure 7-2b. The second configuration, A2, was that the injector, I1, remained at the same position, and the second injector, I2, was moved to the other edge of the reservoir on the top horizontal layer, while the producer, P1 and P2 were centred at the middle of the reservoir as presented in Figure 7-2c. Finally, in configuration A3, the injectors, I1 and I2, were positioned on the top horizontal layers at the centre of the reservoir and the producers, P1 and P2, were fixed on both sides of the reservoir as shown in Figure 7-2d.

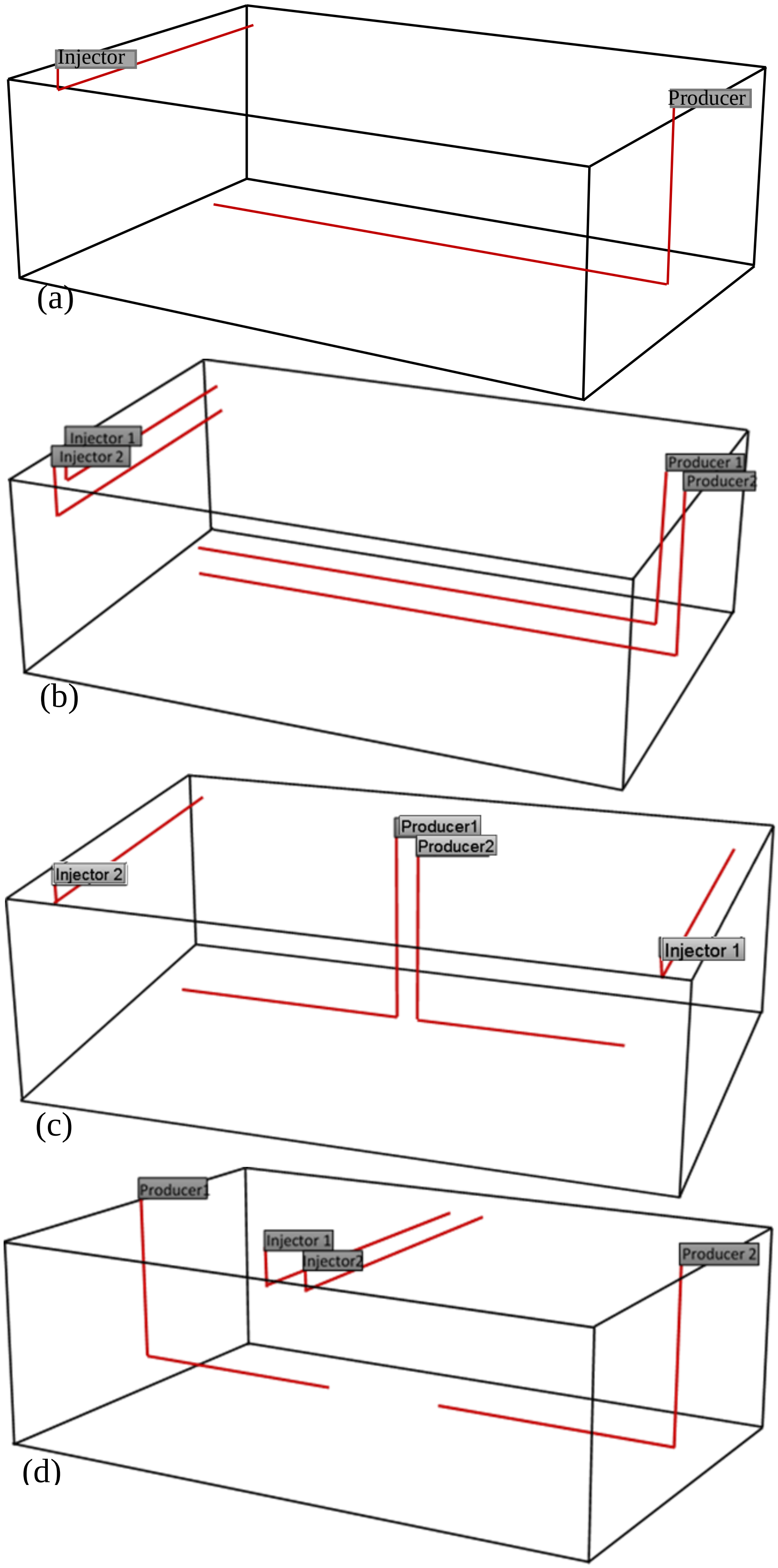

Figure 7-2: 3D reservoir well configurations in (a) model A0 (the original model), (b) model A1, (c) model A2 and (d) model A3.

7.3.2 THAI simulation results

Heavy oil of Virgin Athabasca was used in the THAI simulation runs. The oil specific gravity was 1.0143 with 8° API.

7.3.2.1 Oil rate and production

The oil rate and production are considered the most important indicators to assess the performance of THAI process. Figure 7-3 shows that no oil was produced during the ~13 minutes of the heating period. This is because no oil exists inside the production well before starting the air to be injected. It can be seen from Figure 7-3, for all models oil production started earlier in comparison with the Greaves model A0 (the original model). The reason is the presence of two injector wells in the models helps to increase the required amount of heat to pre-heat the inlet zone of the reservoir. As a consequence, it helps to establish a quick communication between the injector wells and the producer wells. It was also observed that, at the beginning, the rate of the oil production dramatically increased to create a high sharp peak. The reason for this is due to the high pressure generated near to the toe of the producer which is caused by the gaseous and light hydrocarbons produced as a result of the thermal cracking occurring due to the heat provided at the inlet zone of the horizontal injectors. Based on the comparison between all the well configurations, it is obvious that A2 arrangement had the highest production rate and the A3 model then came second; however, the A0 and A1 configurations had the lowest oil production rates. From Figure 7-4, it can be observed that the cumulative oil recovery, for the A0 and A1 configurations, is almost the same. The highest amount of the produced oil was the A2 model and then the A3 model. It is suggested that the presence of the two well injectors in these models was behind the high amount of the oil production. -

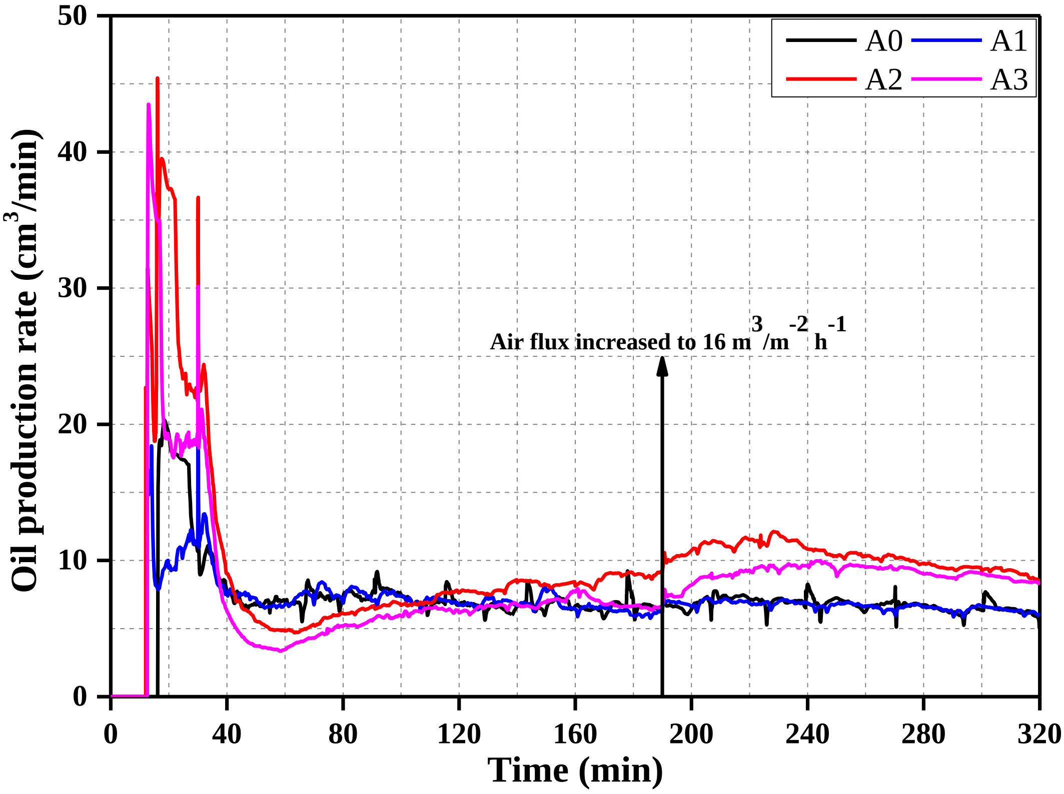

Figure 7-3: Oil production rates.

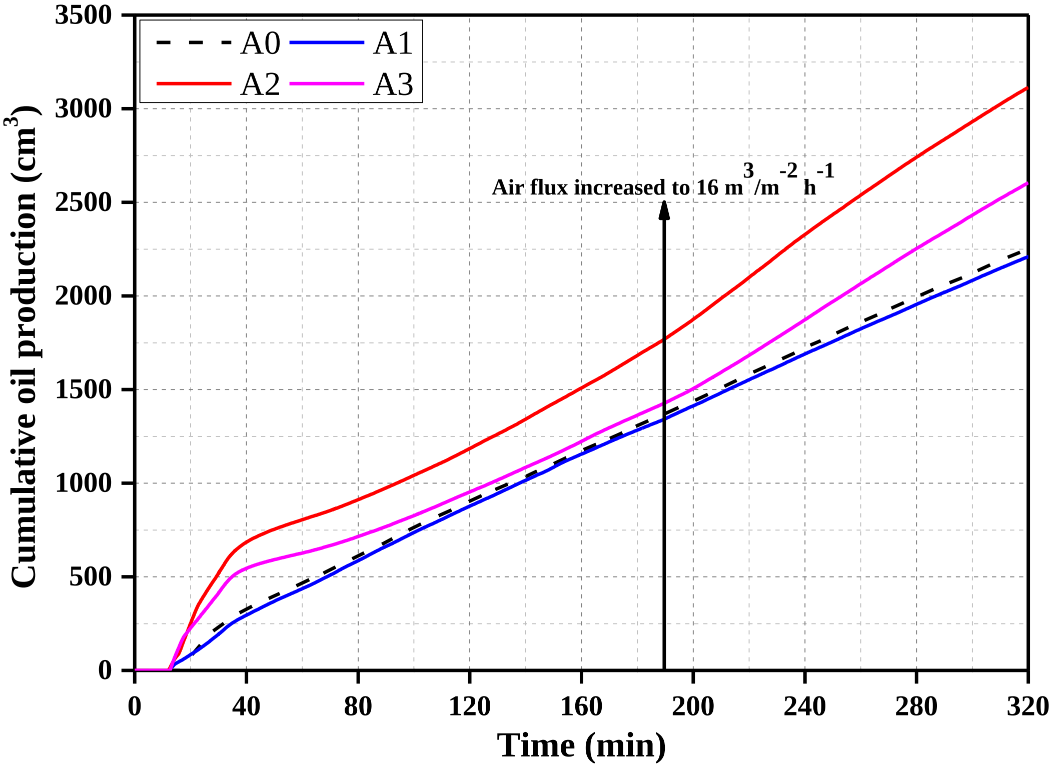

Figure 7-4: Cumulative oil production.

7.3.2.2 Combustion front temperature

The most significant feature in the THAI in-situ combustion process is that the advancing combustion front is propagated in a very stable way throughout the distance from the top to the bottom of the heavy oil reservoir. Oxygen is injected from the top of the reservoir to generate this combustion front, which can be sustained by the continued flow of the oxygen-containing gas at the reservoir's top, with low viscosity oil passing toward the production well. High-temperature reactions take place in this process. At the combustion front, most of the oxygen will be consumed by these reactions. From Figure 7-5, it can be seen that, during the pre-heating time period, the peak temperatures for all the models followed nearly the same trend, except the A3 model which was a little below the others. Then, after ignition is achieved, the A0 and A1 models exhibited almost the same behaviour until the end of the simulation. However, the behaviour of the A2 and A3 models were different, where the A2 model was more stable than the A3 model until the simulation end. As a consequence, the location of the injectors and producers has a significant effect on the stability performance of the THAI process. The small spikes on the more smooth tradition peak temperatures, which have different position depending on the well arrangement, are due to the combustion front reaching a high coke concentration at this point of the peak temperatures inside the producer.

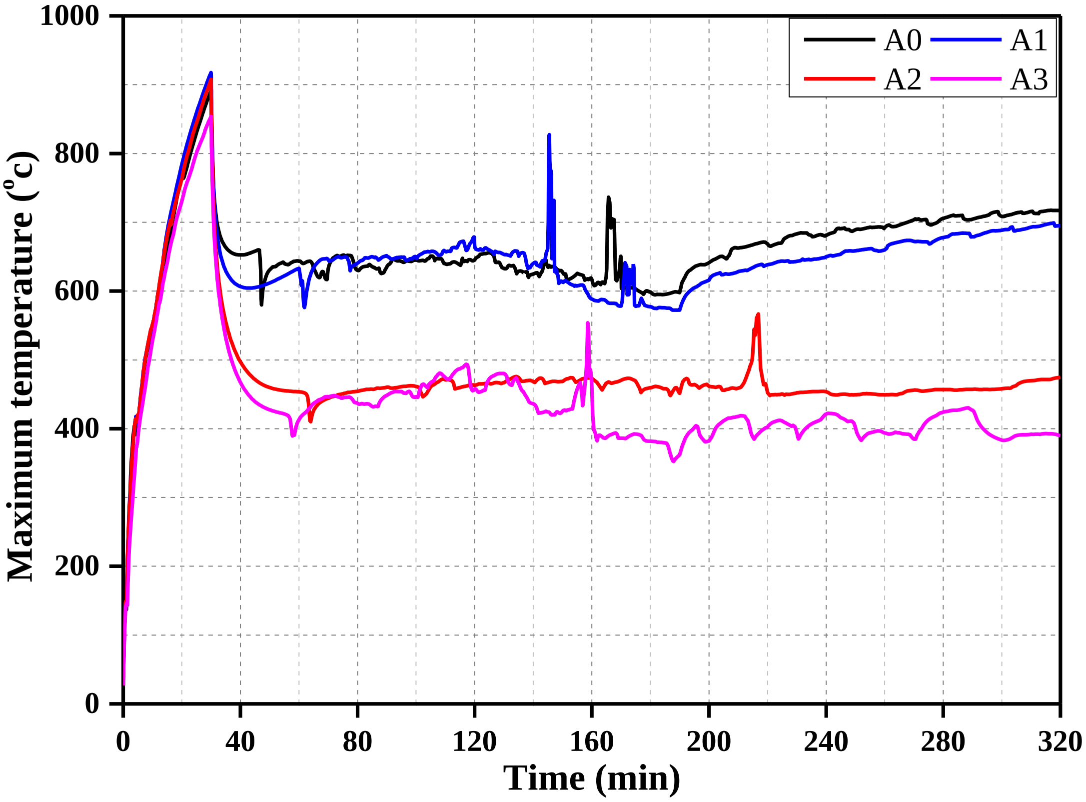

Figure 7-5: Peak temperatures for different Well Configurations.

7.3.2.3 Mole fraction of oxygen production

The amount of the oxygen used is one of the most important parameters in the THAI process for enhanced heavy oil recovery. It is considered a good indicator of the performance of the combustion propagation. Therefore, the amounts of consumed and produced oxygen are very significant for the sustainability and the stability of the combustion front. On the other hand, the amount of the consumed oxygen can be calculated from the oxidation process occurring in front of the combustion front because of the high temperature generated through the burning process of the heavy oil. Figure 7-6 presents the mole fraction of produced oxygen for the different models during the time period of the simulation. It is clear that the oxygen production started early in the A3 model at about 160 min, while it began late in the A1 and A2 configurations. Although the oxygen production commenced late in the A2, it almost behaved more stable than the other models compared to the Greaves model. It can be also observed from Figure 7-7 that oxygen profile in model A2 showed close agreement with that for Greaves model (A0). The concentration of the deposited coke at the toe and the heel of the HP well has a direct effect on the amount of the produced oxygen. In the case of the model A3, where the fuel concentration was low, the oxygen breaks through earlier. In contrast, the concentration of the fuel was more in the A1 and A2 models. Moreover, the oscillation in the curve of the model A3 is caused by the presence of alternate low and high concentration of coke along the horizontal producer.

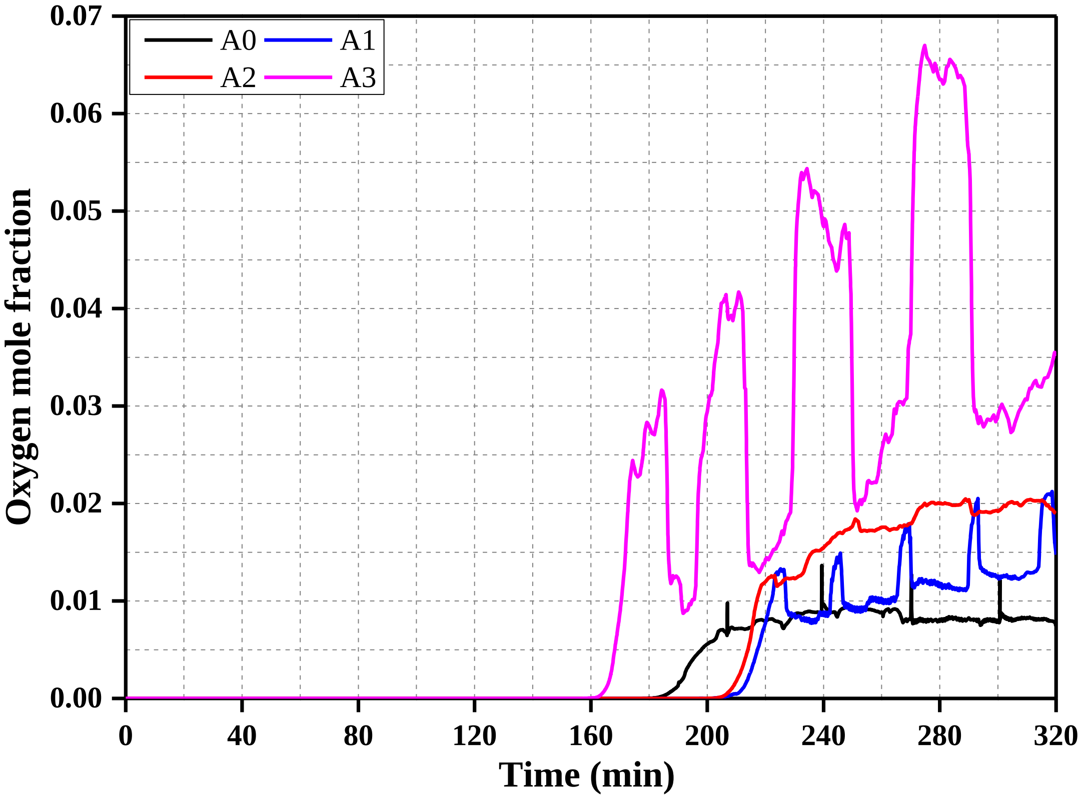

Figure 7-6: Mole fraction of produced oxygen in the 3D combustion cell.

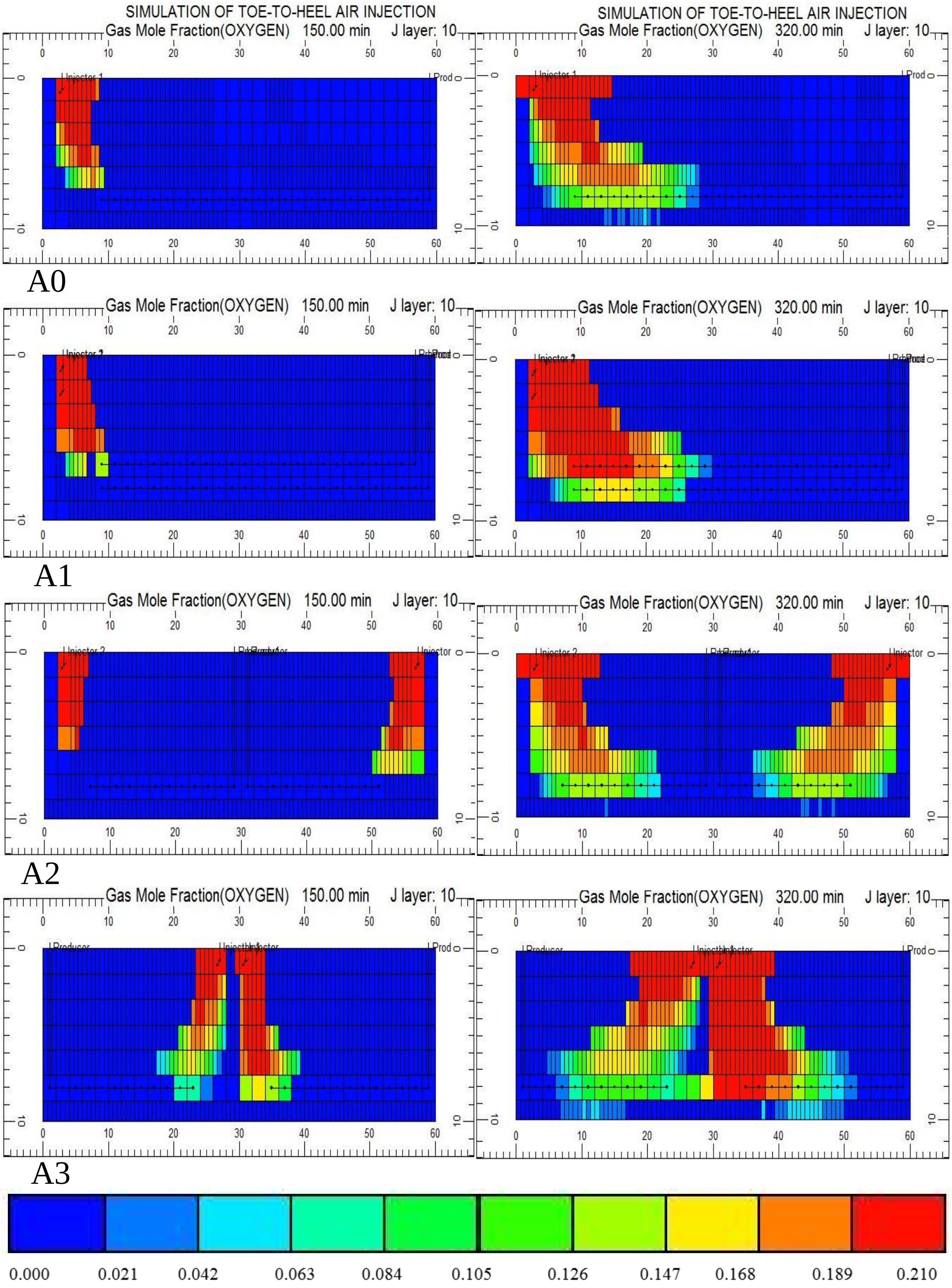

Figure 7-7: Oxygen profiles along the vertical plane for various configurations at different times.

7.3.2.4 Solid Phase (Coke)

The solid phase (coke), which is a result of the heavy oil thermal cracking process, is created instantly in front of the combustion zone in the oil reservoir. This provides the required fuel to sustain the combustion process for the THAI technique. The concentrations of the deposited coke in each of the configurations analysed at the same section and same time, gives a good indication of the efficiency of the volumetric sweep. From Figure 7-8, it can be seen that the shape of the volumetric sweep in all models is almost the same. It can be noticed that the deposited coke extends over a wide zone gradually from the low concentration at the top reaching the highest concentration at the base of the reservoir down near the horizontal production well. The blue area represents the shape of the propagated combustion front, through the cross-section, which is entirely burned because of the ready supply of oxygen.

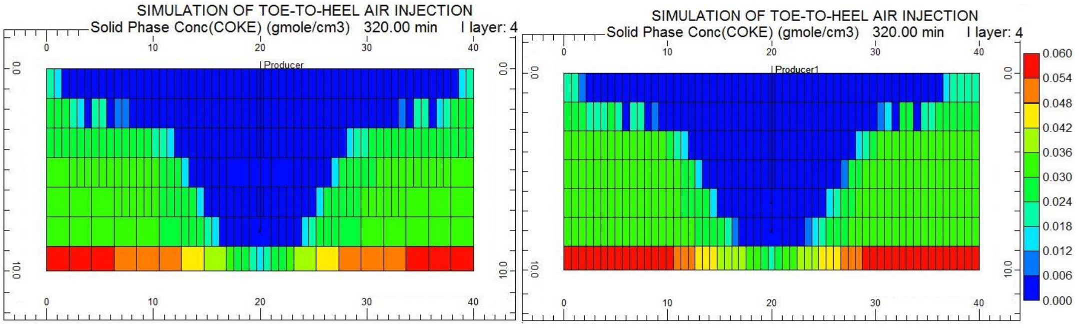

A0 model A1 model

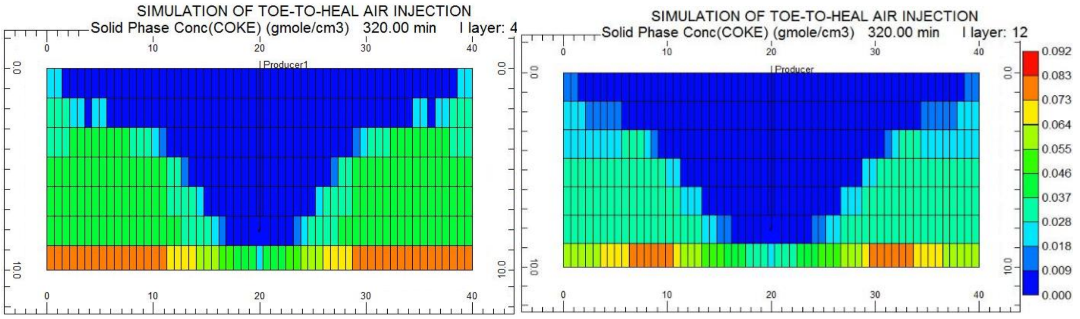

A2 model A3 model

Figure 7-8: Solid Phase (Coke) concentrations for the various THAI well configurations.

To enhance the amount of the produced oil further, model A2 was used to test the impact of the flow rate of the injected air on the performance of the THAI process. The results obtained from model A2 were compared to the original model (A0) as shown in Figure 7-9 and Figure 7-10. Figure 7-9 displays the amount of the oil produced in A0 and A2 models along the combustion period, at different air flow rates. Quantitatively, it can be observed that oil produced in model A2 was increased with increasing the flow rates of the injected air. It was clear that the amount of the oil produced in model A2 had become about twice of that the oil produced by Greaves model (A0) when the air flow rate was increased about 50 % compared to what was injected in model A0.

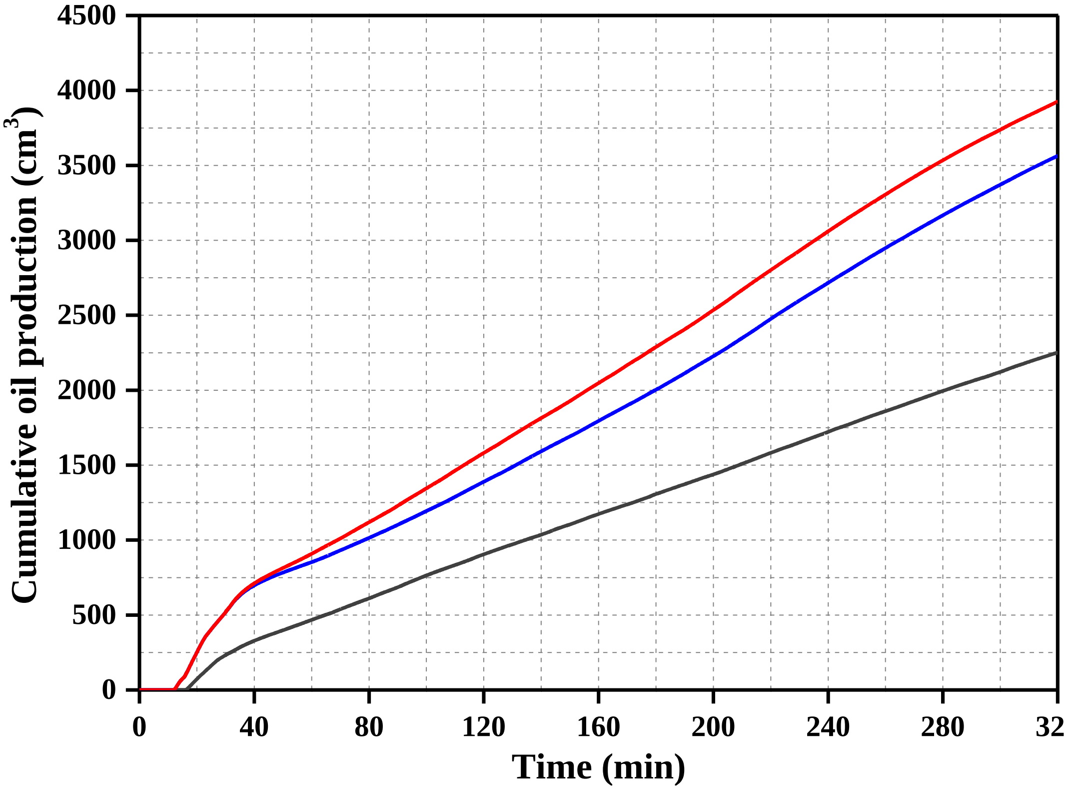

Figure 7-9: Cumulative oil production for two different well arrangements at different air flow rates, a grey line is the Greaves model at 12 and 16 m^3 m^{-2} h^{-1}, a blue line is A2 model at 15 and 20 m^3 m^{-2} h^{-1} and a red line is A2 model at 18 and 24 m^3 m^{-2} h^{-1} flow rates.

Figure 7-10 clarifies the behaviour of the peak temperature for model A2 at different air injection flow rates compared to the peak temperature obtained from the original model. It was noted that the temperature of the combustion cell was significantly affected by the flow rate of the injected air to the reservoir. As a consequence of increasing the flow rate of the air injection in model A2, the amount of the produced oil doubled, compared to the original model A0. In addition, the temperature of the combustion zone was substantially raised to be very close to the temperature in the original model (A0), as can be seen in Figure 7-10.

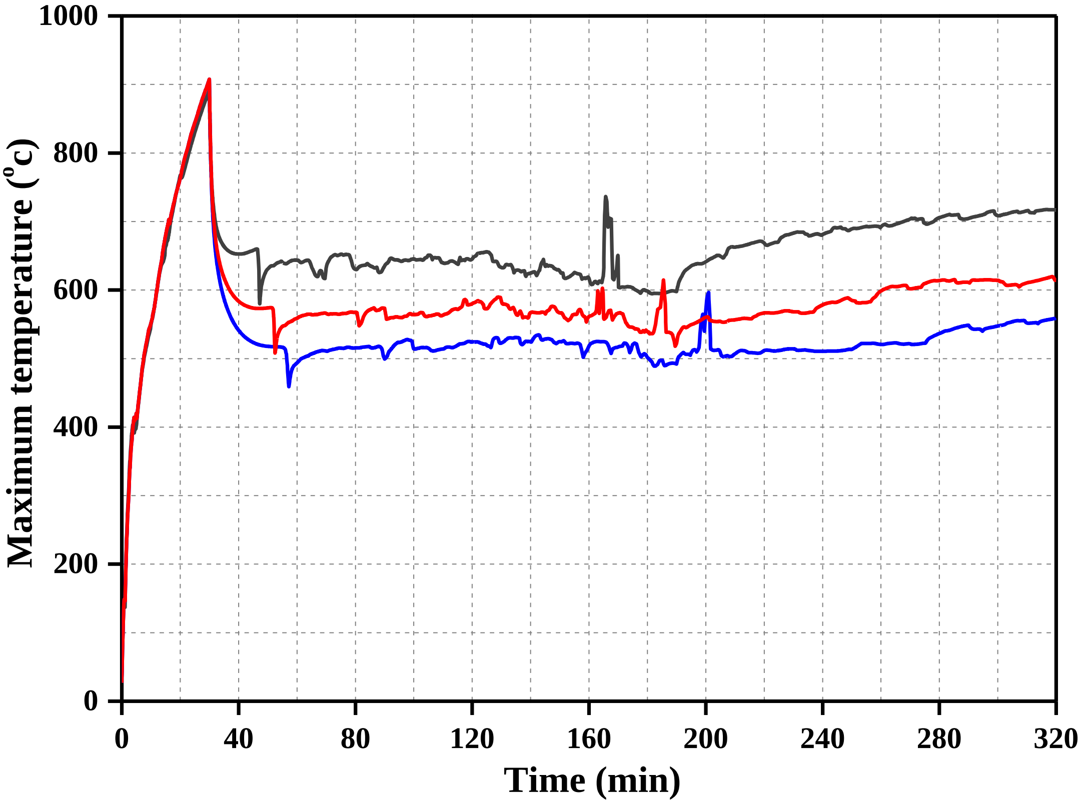

Figure 7-10: Peak temperatures for two different Well Configurations at different flow rates, a grey line is the Greaves model at 12 and 16 m^3 m^{-2} h^{-1}, a blue line is the A2 model at 15 and 20 m^3 m^{-2} h^{-1} and a red line is the A2 model at 18 and 24 m^3 m^{-2} h^{-1} flow rates.

7.3.3 THAI-CAPRI simulation results

The largest reserves of oil in the world are heavy oil and bitumen which represent about 80% of the World's reserves and are concentrated in Canada and Venezuela. These reserves could compensate for the depletion in conventional oil production (de Sena et al., 2013). Since heavy oil and bitumen have a high viscosity and are poorly transportable, then need to be subjected to an upgrading process to be transferred to light crude oils. The crude oils then become readily transportable and acceptable to be used as a refinery feedstock (Carrillo and Corredor, 2013). In addition, the upgrading technology adds a significant environmental advantage since it retains heavy metals, such as S, Ni and V, in the reservoir. Rabiu Ado (2017) has generated the input parameters to simulate THAI-CAPRI process at laboratory scale. The frequency values of the hydrotreating reactions were adjusted, via trial and error, based on the API values illustrated by (Xia and Greaves, 2001, Xia et al., 2002), until an average value of the API gravity was achieved about 6 points over the original oil. At the beginning of the study, the original frequency factors were applied, creating a base case model to be compared with others having different frequency factors. The models were denoted TC0 (which is a base case) TC1, TC2, TC3 and TC4. In each model, the original frequency value has been multiplied by a variable factor to study its effect on the simulated performance of the CAPRI process. Among these models, it was found that the TC3 model was the best one, in which the frequency factor of the kinetic reactions has been adjusted to give a high cumulative oil, which has been subsequently adopted in this study. An electrical heater was used to pre-heat the sandpack for 30 minutes, and a gas mixture of air and hydrogen was then injected at a flow rate of 10000 $cm^3\ min^{-1}$, which corresponded to 15 $m^3\ m^{-2}\ h^{-1}$. The initial hydrogen to the air ratio (HAR) used was 1:4 as it was assumed in the study of (Shah et al., 2011, Hart et al., 2013). As discussed concerning the standard THAI process, after 190 minutes, gas flow was increased to 13333.3 cm^3 min^{-1}, which is equivalent to a flow rate of about 20 m^3 m^{-2} h^{-1}, and it was maintained until the end of the simulation. In this project, the effect of the catalyst thickness has been investigated as well as the effect of the hydrogen to the air ration. In addition, the effect of the catalyst packing porosity has taken into account.

7.3.3.1 Model configurations

The TC3 model used by Rabiu Ado (2017), which is the same model used in the experimental study of Greaves et al. (2012), was also used in this study. The model has horizontal injector and producer (HIHP) wells which were configured in a staggered line drive (SLD). In addition, a catalyst layer was placed around the HP section in the CAPRI model as illustrated by the coloured part in Figure 7-11. Moreover, instead of using 30 × 19 × 7 grid blocks in the original model, the CAPRI model was discretised into 30 × 19 × 9 grid blocks to compensate the area lost due to the added catalyst.

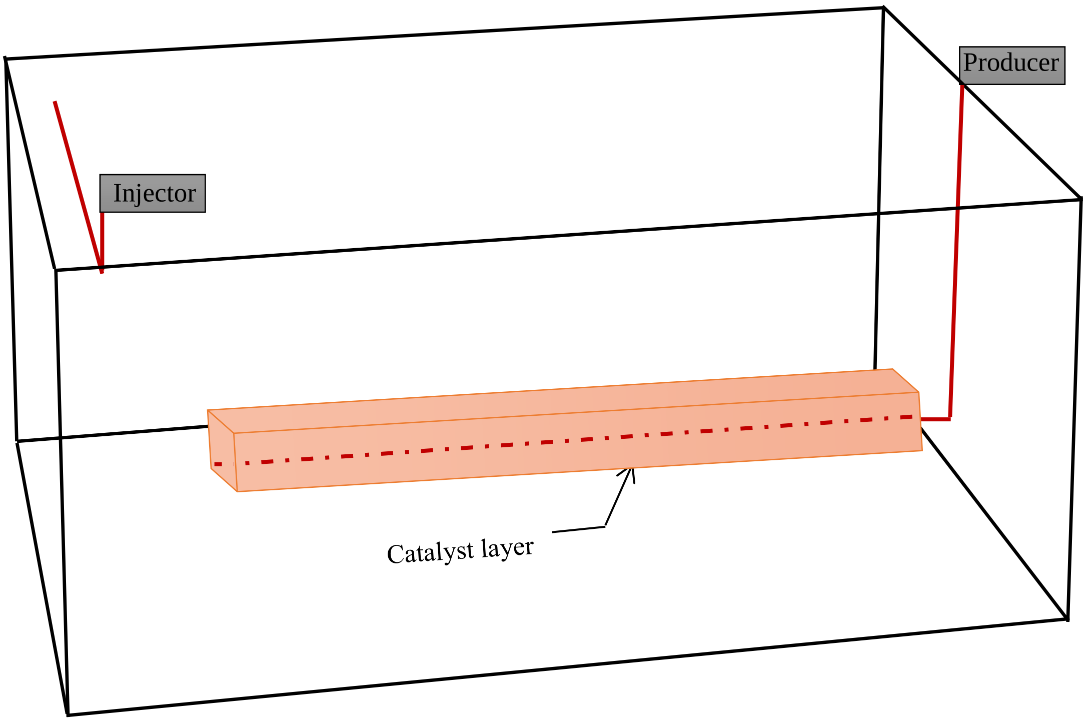

Figure 7-11: 3D schematic diagram of THAI-CAPRI technique with a catalyst layer placed around the producer.

7.3.3.2 Physical properties of the upgraded oil

Based on the distillation data obtained from Hart et al. (2014) to provide the numerical model by the catalytic reaction for the upgraded oil produced, Rabiu Ado (2017) has been computed the PVT data of the light and heavy upgraded oil using Aspen HYSYS software as presented in Table 7-3.

Table 7-3: Physical properties of the upgraded oil produced (Rabiu Ado, 2017).

Components	Mole fraction (mol%)	Molecular weight (g/mol)	Density (Kg/m^3)	T$_C$ (℃)	P$_C$ (kPa)
LUO	20.31	128.01	776.53	353.12	2448.61
HOU	79.69	252.50	850.48	502.19	1523.46

In addition, in the THAI-CAPRI process, catalytic reactions occur beside the different reactions occurring when the THAI process has been tested alone. These catalytic reactions involve mostly hydrodesulfurization (HDS) and hydrodenitrogenation (HDN). Water/gas shift (WGS) and steam gasification (SG) reactions are also observed for the process. Therefore, to simulate the model, further calculations needed to determine the kinetic parameters, the stoichiometry of these reactions, the frequency factor and the activation energy and the fractions of sulphur and nitrogen atoms. All these requirements have been reported in detail by Rabiu Ado (2017), as illustrated in Table 7-4 and Table 7-5.

Table 7-4: Balanced reactions of HDS and HDN with the kinetics parameters (Rabiu Ado, 2017).

HDS and HDN reactions	**Activation Energy (J/mol)**	**Frequency Factor (min^{-1})**
Heavy oil + 19.932 $H_2 \longrightarrow$ 3.477 HUO + 0.585 H_2S	**87×10^3**	**2.7×10^7**
Light oil + 3.286 $H_2 \longrightarrow$ 1.328 LUO + 0.194 H_2S	**87×10^3**	**2.7×10^7**
Heavy oil + 1.593 $H_2 \longrightarrow$ 3.477 HUO + 0.189 NH_3	**75×10^3**	**1.0×10^6**
Light oil + 0.095 $H_2 \longrightarrow$ 1.328 LUO + 0.011 NH_3	**75×10^3**	**1.0×10^6**

Table 7-5: Elemental compositions of the pseudo-components (Rabiu Ado, 2017).

Constituent	Bitumen	Heavy	Light	LUO	HUO
H (wt%)	10.687	10.430	13.005	16.764	12.866
C (wt%)	84.075	84.210	82.859	82.859	84.210
N (wt%)	0.414	0.447	0.112	0.019	0.147
S (wt%)	4.824	4.913	4.025	0.359	2.777

7.3.3.3 Catalyst preparation

The catalyst used in this study was Houdry which has been tested, discussed in the experimental section, by different techniques such as mercury porosimetry, gas adsorption, NMR etc. The catalyst was placed around the producer so that the produced oil to be travelled to the production well has to go through the catalyst first. The layer thickness for the catalyst as used by Rabiu Ado (2017) has been adopted in this study with an initial thickness of 0.5 cm to commence with. The catalyst properties obtained from the experiments were used to compute the packing porosity and the concentration of the catalyst used to simulate the model. The elements, and their particular fractions, of the Houdry catalyst, can be seen in Table 7-6. The bulk density of the catalyst, 1361.7 kg m^{-3}, is taken from the empirical results in this study. This density is integrated with the void volume and the packing porosity to calculate the concentration of the catalyst loading, using the following equation taken from STARS manual (CMG, 2013).

$$\varphi_f = \varphi_v \left[1- C_c/\rho_c\right] \tag{7-5}$$

where: φ_f is the packing porosity, φ_v is the void porosity, C_c is the catalyst concentration (kg m^{-3} pore volume), ρ_c is the catalyst bulk density (kg m^{-3}). The initial value of the catalyst packing porosity used was taken from Abu et al. (2015), which was 45.1%. Two other values of the packing porosity have been investigated to simulate the effect of this feature on the performance of the CAPRI process. These values with the results obtained from the above equation were tabled in Table 7-7.

Table 7-6: Element composition of houdry catalyst.

Element	RMM (g/mol)	Amount/wt%
Al_2O_3	101.96	40.54
SiO_2	60.08	48.44
Cl	35.45	6.20
TiO_2	79.866	3.03
Fe_2O_3	159.69	1.15
Total	76.89	100.00

Table 7-7: Calculated the concentration of the catalyst based on different fluid porosities.

Packing porosity (%)	Void porosity (%)	Bulk density (kg/m^3)	Catalyst loading (kg/m^3 pore volume)	Catalyst loading (mol/cm^3 pore volume)
44.0	0.99	1361.7	756.5	0.009912517
44.55	0.99	1361.7	748.935	0.009813392
45.1	0.99	1361.7	741.37	0.009714267

7.3.3.4 Effect of packing porosity

The initial porosity is likely the most important parameter which can be affected by the particle packing. Spherical and cylindrical particles are the most predominantly used in the chemical engineering operations. For cylindrical particles, both the initial porosity and the packing size are dependent on the shape of the particle. Generally, sphericity is considered the most commonly utilized factor to describe the particle shape, which represents the ratio of the sphere's surface area to the surface area of the particle possessing the same volume as the sphere (Zou and Yu, 1996). The packing formation has an effect on many parameters such as fluid behaviour, heat transfer and mass transfer, which affect the macroscopic process. Principally, a packing of cylindrical particles behaves differently from one of spherical particles because cylinders offer directional freedom, and their geometry involves a diversity of surface constituents such as a flat and curved surface in addition to corners (Zhang et al., 2006). An experimental study has been conducted by Abu et al. (2015) to upgrade Athabasca bitumen using packing porosity values of 44 and 45.1 %, which were used in this study as well as 44.55 %.

7.3.3.4.1 Oil production

Figure 7-12 shows the amount of oil production at the time of the simulation for several various packing porosities. It can be observed that there is a slight difference in the amount of the produced oil during the CAPRI process. However, an increase in the oil production, with the increase in the value of the packing porosity, can be seen. This is because that the initial porosity of the catalyst increased as more space between the catalyst particles was increased, which allows for more fluid passing through the catalyst into the production well.

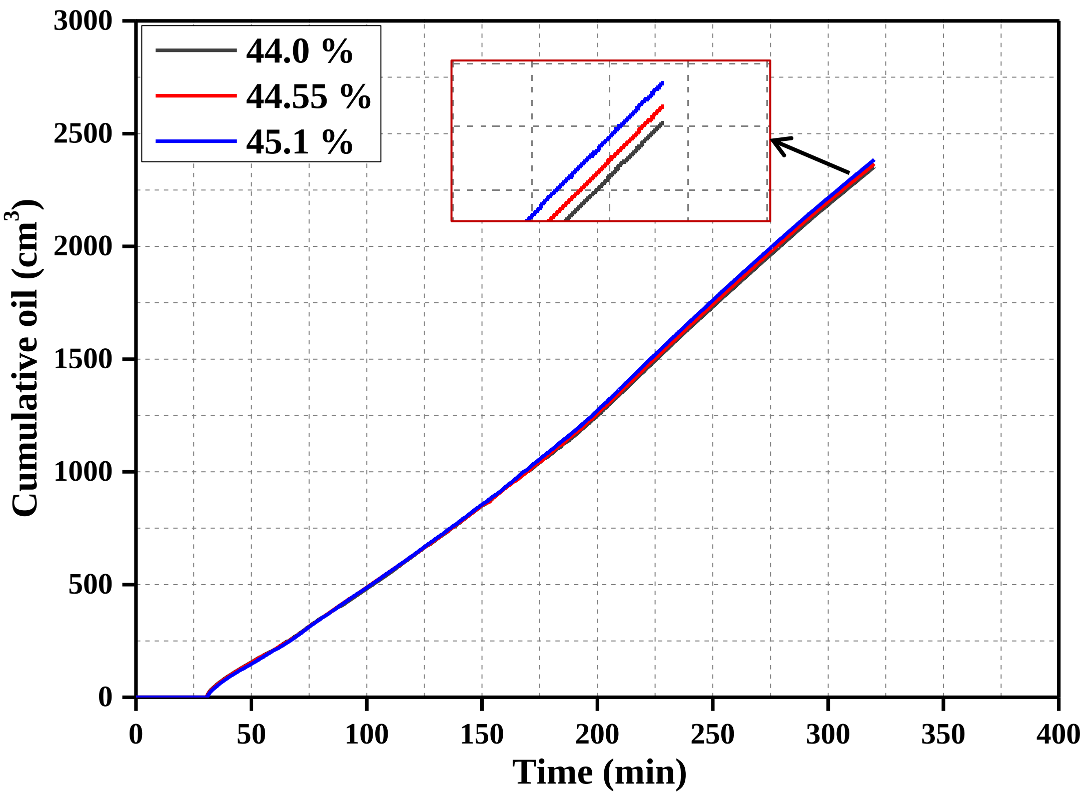

Figure 7-12: Cumulative oil for different values of packing porosity.

7.3.3.4.2 Temperature distribution

Figure 7-13 illustrates the effect of the several values of packing porosity on the temperature distribution with time during the THAI-CAPRI process. Despite the differences in the packing porosity, all models have nearly the same predicted temperature pathway along the combustion front until the simulation end, as can be seen from Figure 7-13. Therefore, based on the peak temperature characteristics, the change in the packing porosity value has no effect on the temperature distribution. This means that the combustion front propagation is stable, and all models have almost the same combustion front shape as can be noticed in Figure 7-14. Figure 7-14 showed that the shape of the combustion front, at 320 minutes, was forward leaning and swept in the upper portion of the reservoir, which is considered as one of the indication parameters of stability.

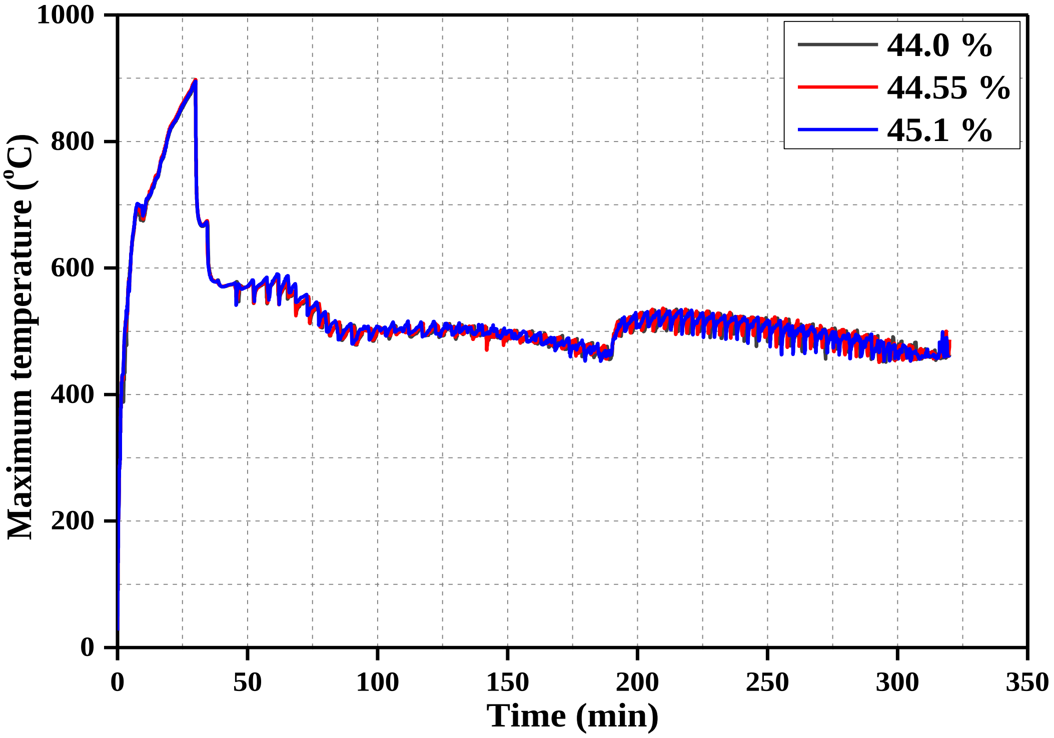

Figure 7-13: Peak temperature for several different packing porosities.

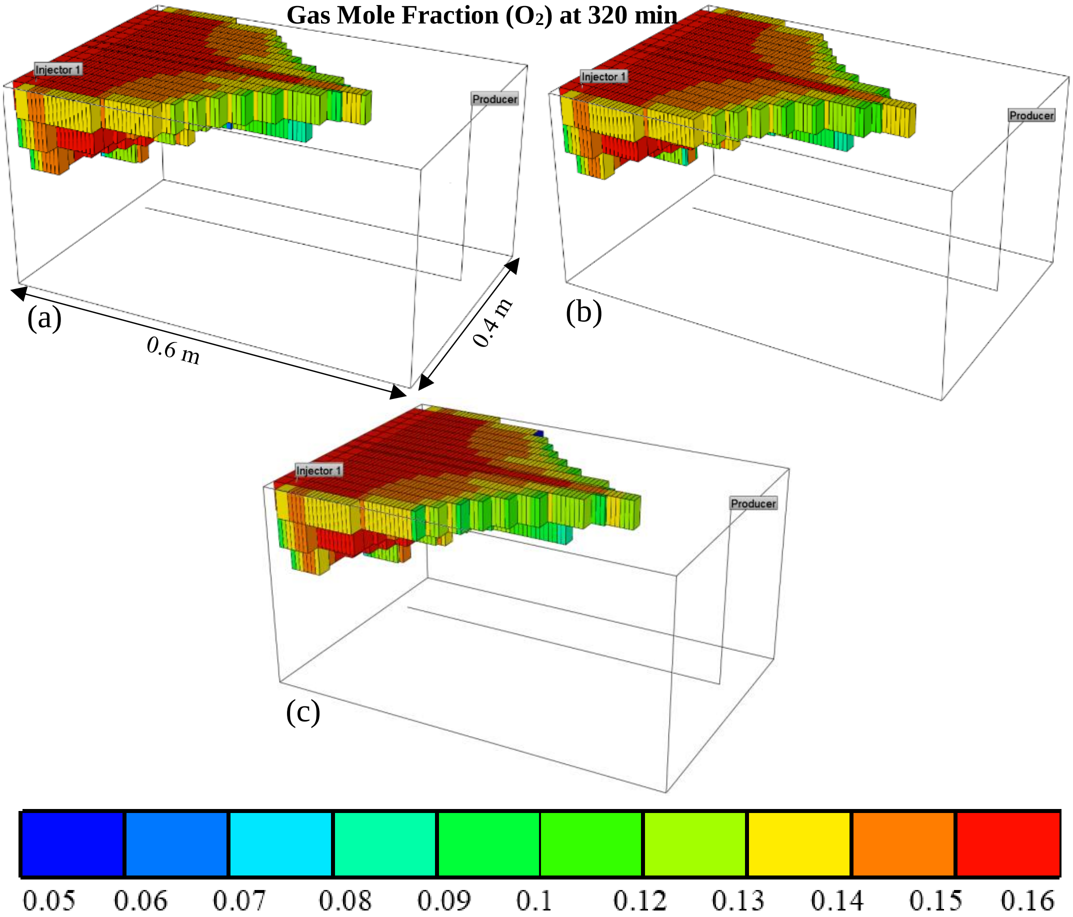

Figure 7-14: 3D combustion front propagation (a) 44.0%, (b) 44.55%, (c) 45.1% packing porosity at 320 minutes.

7.3.3.5 Effect of hydrogen to air ratio

During the THAI-CAPRI process, the existence of hydrogen is a necessary requirement for in-situ catalytic cracking reactions. Hydrogen injected with air in the presence of the catalyst around the horizontal producer assists in the hydrogenation reaction. The hydrogenation process and asphaltene removal result in the upgrading of heavy oil in situ (Weissman et al., 1996). Another source of hydrogen can be provided by steam gasification (SG) and/or water-gas-shift reactions (WGS) (Hajdo et al., 1985), as presented in the following simple equations (Rabiu Ado, 2017):

$$\text{WGS: } CO + H_2O \longleftrightarrow CO_2 + H_2 \qquad (7\text{-}6)$$

$$\text{SG: } C_iH_a + 2iH_2O \longrightarrow ICO_2 + (2i + a/2)\ H_2 \qquad (7\text{-}7)$$

Hydrogen plays an important role in the HDN reaction in which the bond between the carbon atom and the nitrogen is broken and replaced with a hydrogen atom, and combination process takes place between nitrogen and hydrogen to form ammonia (Abu et al., 2015). Hart et al. (2014) have been investigated several types of gas media on the performance of CAPRI upgrading using heavy oil and bitumen. It was found that the addition of hydrogen enhances the reactions of the hydrocracking and the hydrogenation processes, whereas, in the case of the other gas media, heavy coke formation was associated with the upgrading process. It is also noticed that hydrogen results in characteristically high API gravity, low viscosity and high distillables in the produced oil. In this study, three different ratios of hydrogen to air have been employed to investigate its effect on the performance of the CAPRI process. These ratios are 1/4, 2/4 and 2.5/4.

7.3.3.5.1 Oil production

The effect of the various ratios of hydrogen to air on the cumulative oil in the THAI-CAPRI technique has been illustrated in Figure 7-15. As can be seen from the Figure 7-15 the amount of the produced oil was affected by the value of the injected hydrogen. Where the oil production decreased with increasing of the hydrogen to air ratio. Where 2366 cm^3 of oil was recovered when the ratio of hydrogen to air was low, and when the ratio was increased, the amount of the produced oil dropped to 2161 cm^3, and a further increase of the hydrogen to air ratio, the recovered oil declined to 2059 cm^3. The high ratio of hydrogen to air means the lower injected air, and this resulted in an increase in the amount of the coke deposited, which in turn led to a drop in the oil production.

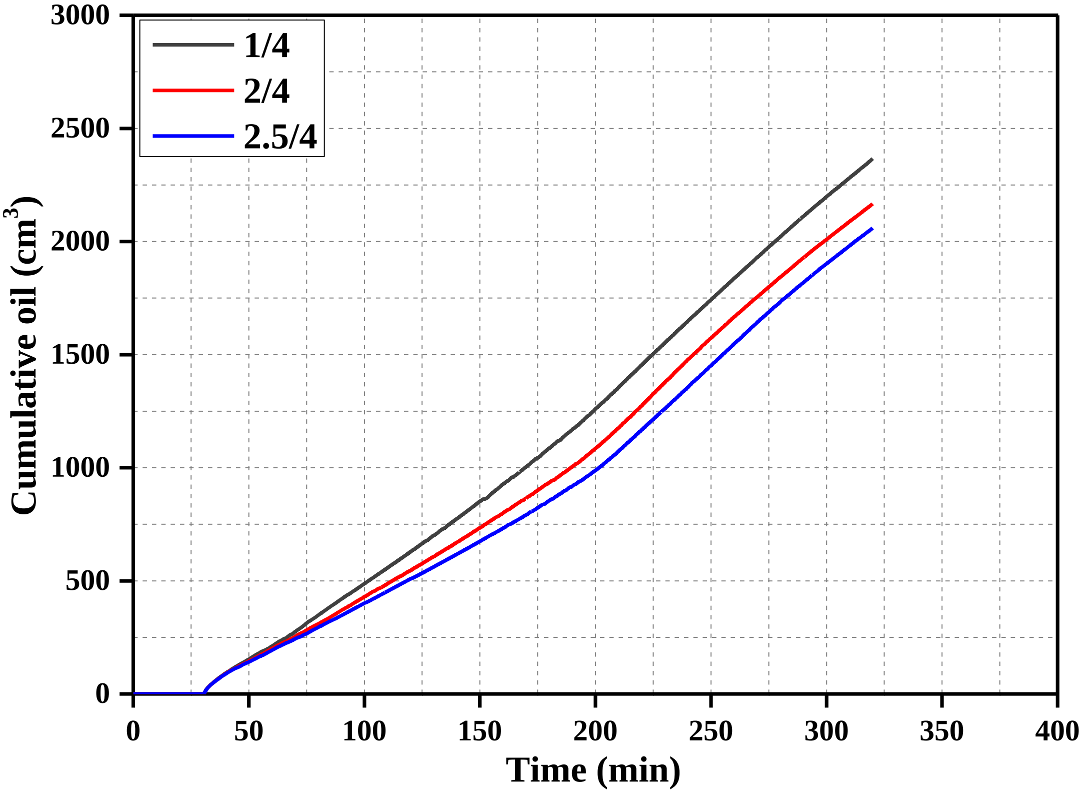

Figure 7-15: Cumulative oil vs time using different hydrogen to air ratio.

7.3.3.5.2 Peak temperature

Figure 7-16 displays the temperature distribution of the produced oil along the reservoir as a function of time. It is noticed that the peak temperature having the lowest hydrogen to air ratio diverges first and continues overlaying all the other curves up to the end of the process, and then the second one with the middle value and following with the highest ratio of hydrogen to air. This is because that the one with the lowest gas injected will consume the lowest amount of energy in form of heat. That means the peak temperature is highest with the lowest amount of gas injected.

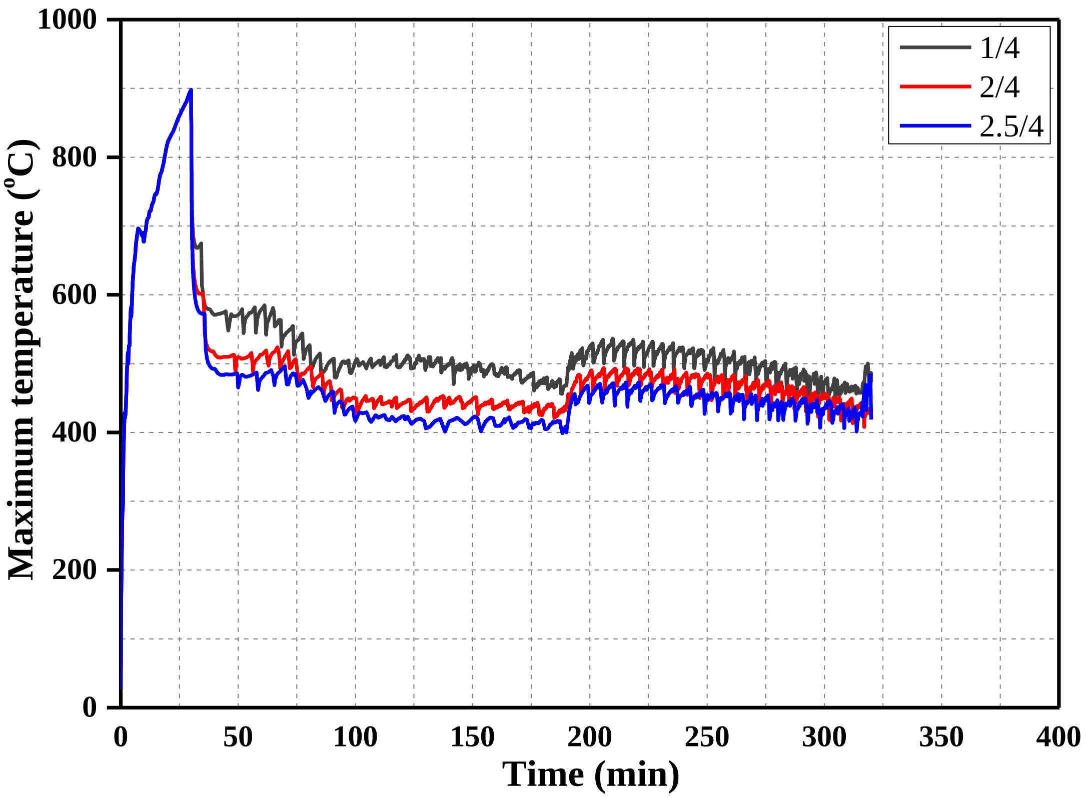

Figure 7-16: Temperature distribution.

7.3.3.6 Effect of catalyst thickness

Catalysts are materials that can speed up chemical reactions and enhance the selectivity of the reaction without consumption themselves (Huang et al., 2012). However, CMG-STARS will deal the catalyst as a reservoir rock because it does not identify it as a portion of the reactants, and the equation can be described by the following formula:

$$\text{Heavy oil} + 19.932\ H_2 + CAT \longrightarrow 3.477\ HUO + 0.585\ H_2S + CAT \qquad (7\text{-}8)$$

In this part, the effect of the catalyst thickness on the performance of the THAI-CAPRI process is illustrated. Three different thicknesses of catalyst have been investigated to study its effect on the cumulative oil production and the peak temperature. The thicknesses were 0.5, 0.75 and 1.0 cm.

7.3.3.6.1 Oil production

Figure 7-17 shows the effect of the catalyst thickness on the cumulative oil during the simulation period. As can be noticed from Figure 7-17, there is a slight difference in the amount of the produced oil. It is observed that the model having a catalyst with a thickness of 0.5 cm has the highest amount of the produced oil, and this amount decreased with an increase of the catalyst thickness. This is because that most of the thermal cracking has taken place on the surface of the catalyst in the presence of a high temperature, which resulted in a high concentration of the coke. However, as further of the catalyst thickness increased, more coke formed on the catalyst surface, and thereby, the amount of the produced oil reduced.

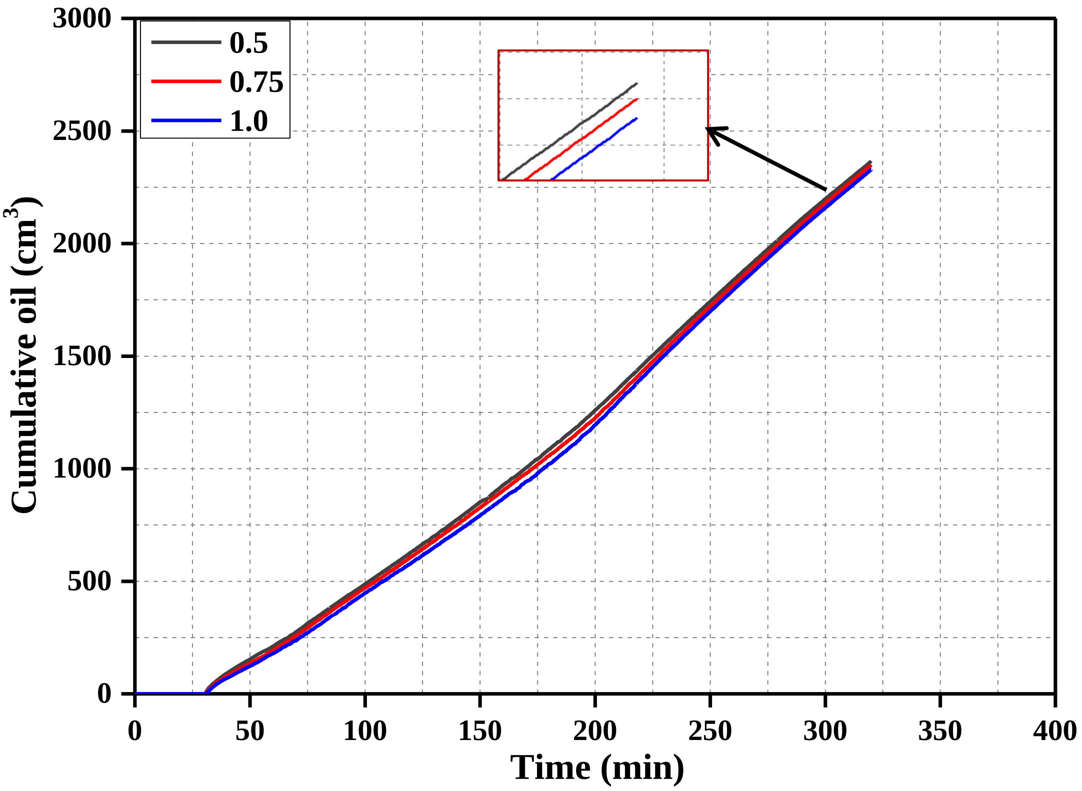

Figure 7-17: Cumulative oil vs time using different catalyst thickness.

7.3.3.6.2 Peak temperature

Figure 7-18 displays the change in the temperature distribution with the time along the reservoir for diverse values of catalyst thicknesses. From Figure, the peak temperature, in the case of the catalyst thickness of 0.5 cm, rose up to about 900 ℃ with ~80 to 100 ℃ higher than that when the thicknesses of the catalyst are 0.75 and 1.0 cm respectively. This is due to the difference in the produced amount of the coke at the end of the preheating time. It is observed that during the lowest air flux from 30 to 190 minutes, the trend of all curves is almost the same.

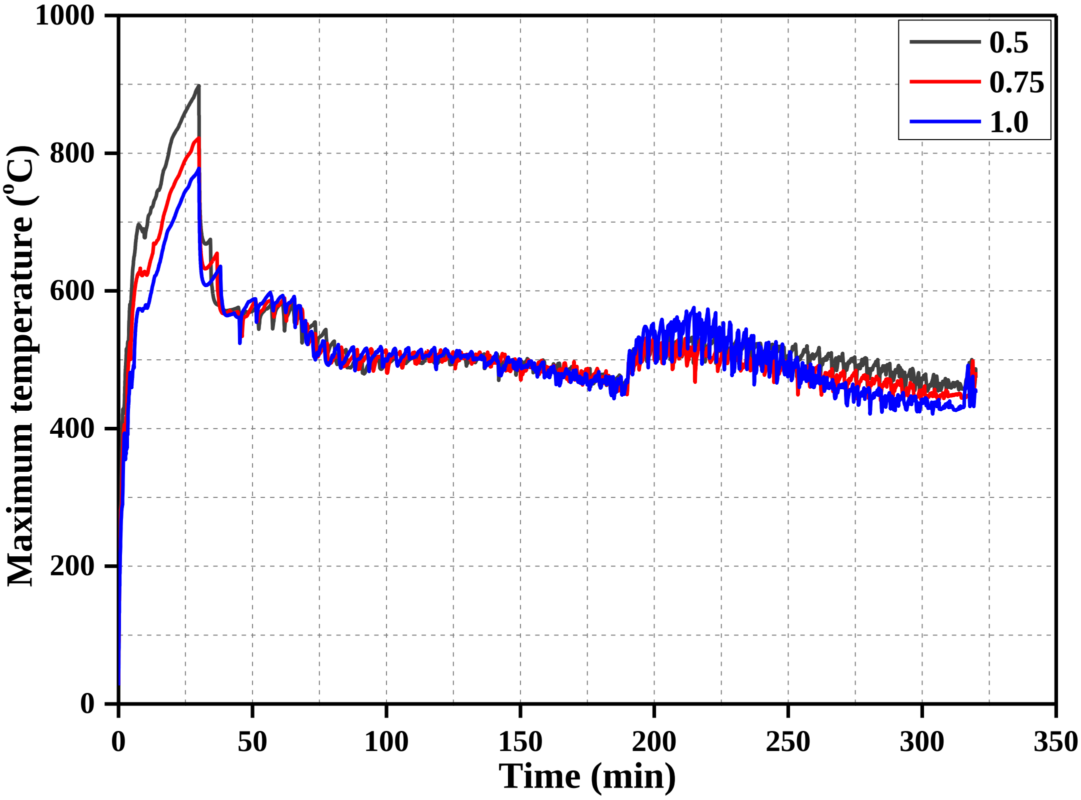

Figure 7-18: Peak temperature for different catalyst thickness.

However, after 190 minutes when the air flow increased, the model having a thickness of 1.0 cm was above the other curves up to about 230 minutes, and then they rearranged depending on the thickness from the lowest one to the highest until the end of the combustion period. During the period from 190 to 230 minutes, when the flow rate of the injected air was increased, more oil flows through the catalyst layer, and due to the large catalyst thickness, the produced oil remains a longer time within the catalyst which leads to an increase in the temperature in this zone.

7.4 Discussions

Downhole catalytic upgrading of heavy oil using the CAPRI process has been simulated in this study. To understand the performance of the catalysts, a new method is needed in order to work out what pore structure looks like following coking. The catalysts are very likely to be deactivated by coking, which changes the structure of the pores, so a new method has been developed to get more accurate pore size distributions for looking at these catalysts. The Houdry catalyst characterised by the experimental section was employed in the simulation to evaluate the performance of the THAI-CAPRI process. The chart below shows the relationship between the experiment and the simulation work.

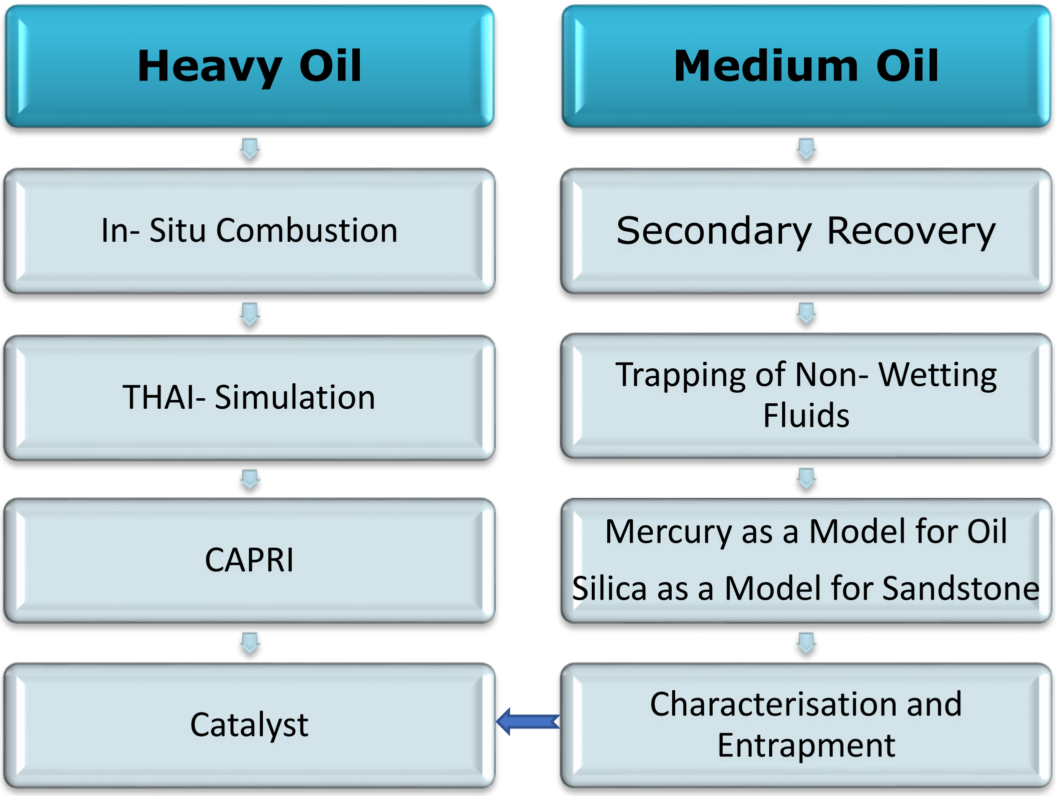

It has been found that the best model was A2 model in which the injectors were designed to be on both sides of the reservoir, and the producers were located in the centre of the reservoir. The findings revealed oxygen breakthrough, which is considered a most important parameter, acted in the same trend as the original model of Greaves (A0). This feature gives an indication that, in an appropriate reservoir, THAI technique is a stable and effective process. However, in the other models, the oxygen production followed a wobbly way to the end of the simulation period. It is also observed that a model A2 gave a high cumulative oil compared to the other models, at the same flow rate of the injected air used in the A0 model. The reason for this is that the symmetry of the combustion front achieved in A2 model have affected a larger volume of the reservoir and hence resulted in a higher volumetric sweep of the reservoir.

Further, when the air injection flow rate was increased in the model A2 by about 50 % of that used first, the amount of the produced oil rose up to about double of the amount of the oil produced by the original model. As a result, the time required in the A2 model to recover the same amount of the oil produced by the original model A0 was reduced by about half.

Moreover, catalytic upgrading using THAI-CAPRI process was simulated to the recovery of Athabasca Heavy Oil to investigate the effect of several parameters on the performance of the CAPRI technique. The change in the packing porosity values had a slight effect on the oil production, and no effect mention on the peak temperature. This small impact could be due to the difference in the particles arrangement from one to another. Similar, the effect of the catalyst thickness on the performance of the CAPRI process, where the amount of the cumulative oil increased with decreasing the thickness of the catalyst placed on the producer. This because of the coke deposited on the surface of the catalyst on which the thermal cracking occurred. Since the cracking reaction takes place on the solid surface, the high catalyst thickness obstructs the flowrate of the oil which leads to a high concentration of the coke on the catalyst surface.

However, the oil production was obviously affected by the ratio of hydrogen to air injected by the injectors to the reservoir. The low ratio of hydrogen to air produced the higher oil cumulative, compared to the high ratios. The high amount of hydrogen implies a low amount of injected oxygen and that resulted in an increase in fuel availability which substantially affects the recovery of the oil.

7.5 Conclusions

3D models using CMG-STARS builder have been employed for simulations of the THAI and THAI-CAPRI processes to investigate an effect of several parameters on the performance of the technique. The influence of variables such as different well configurations using two horizontal injectors and producers have been studied for the THAI technique. Moreover, the packing porosity, catalyst thickness and hydrogen to air ratio have been tested to illustrate its effect on the THAI-CAPRI process. Three different models, with varying locations for the injectors and producers, have been simulated for the THAI process, using Virgin Athabasca oil sand. Compared to the Greaves model (the original model), the second configuration, in which the injectors are located on both sides of the reservoir while the producers are centred in the middle of the reservoir, was the best scheme for the THAI technique, since it gave the highest cumulative oil, and, it also gave rise to the same behaviour as the Greaves model in terms of the temperature distribution and the oxygen breakthrough. In addition, the combustion front shape for the presented simulation was forward-leaning, like the combustion shape in Greaves model, which indicates that the process was perfectly stable. However, in the other models in which the injectors are designed to be near to each other, and this could be the reason for that the amount of the produced oil was less than that in the case of the second model.

In terms of the THAI-CAPRI process, the model used by Rabiu Ado (2017) has been adopted in the present study, but using Houdry catalyst whose properties have been obtained from the practical part of this study. Several parameters such as packing porosity, hydrogen to air ratio, and catalyst thickness were investigated as an extension to the Rabiu Ado (2017) work. The CAPRI simulation presented here provides a new prediction of the required amount of the hydrogen used in the hydrotreating process during THAI-CAPRI technique for the upgrading of heavy oil and bitumen. The findings found that the amount of the produced oil was affected by the value of the hydrogen to air ratio. The simulation also displays that the combustion front propagation was entirely restricted to the upper portion of the sandpack, indicating that the process was completely stable. It is also that the results showed that the oil production was slightly influenced by the packing porosity and the thickness of the catalyst placed around the horizontal producer.

CHAPTER 8

CONCLUSIONS AND RECOMMENDATIONS

8.1 Conclusions

The integrated gas adsorption and mercury intrusion-extrusion porosimetry techniques have been used, to detect the impact of the pore-pore co-operative phenomenon within disordered silica material. The novel method includes conducting a series of nitrogen/argon sorption and mercury experiments on the same sample. The method revealed that there is a difference in the ability of nitrogen and argon to wet new surfaces created by mercury on the silica surface. It was observed that nitrogen is readily wetting of metal mercury surfaces, whilst argon does not wet very much. The findings showed that there was a difference in the measured values of the pore sizes for disordered porous solids obtained by different techniques. Thus, NMR cryoporometry and mercury thermoporometry were separately performed to measure the pore sizes, to determine the effect of the delayed condensation on the accuracy of PSD.

Further, the difference in wetting of solid mercury surfaces by nitrogen and argon adsorbates was also employed to offer information on pore connectivity. DSC thermoporometry following mercury porosimetry was used on a silica-alumina sample, using mercury entrapped within pores as a probe fluid, to measure the pore sizes based on the change in the freezing and melting points. CXT was also integrated with mercury intrusion/retraction porosimetry, to determine the distribution of micro- and mesopores that directly interconnected to macropores invaded by mercury. It was shown that mercury solely becomes trapped in the macropores of a silica-alumina pellet. A basic model for the pore network architecture of the silica-alumina pellet has been derived from gas sorption scanning curves and NMR cryoporometry data. It has been shown that the pore network structure is hierarchical, with gradually smaller pore leading off larger pores, much like the blood circulation network in animal bodies.

Another CXT image was taken for an alumina pellet containing mercury entrapped within pores following mercury porosimetry. It was observed that mercury entrapped macropores within alumina pellet. It is also CXT image detected that macropores had no any connection with other macropores, and connected to each other by very narrow necks as can be seen in the mercury intrusion curves.

A laboratory scale model of a 3D combustion cell was simulated to investigate the effect of a different design for the injector and producer wells on the performance of the THAI technique. Three models, namely A1, A2 and A3, with various well arrangements were applied in this simulation, involving Virgin Athabasca oil sand. A comparative study of the three models and the Grieves model (the base case model) showed that model A2 predicted a higher production of heavy oil. The findings revealed that the combustion front was propagating in a stable way just like in the Greaves model. It was observed that the amount of the produced oil was significantly affected by the position of the horizontal injectors. More oil was produced when the HI are separated from each other. Additionally, the location of the well configurations influenced oxygen production rate, and when it begins.

The catalytic process (CAPRI) was studied in this work, to demonstrate the effect of several parameters, such as catalyst packing porosity, catalyst thickness and hydrogen to air ratio, on the effectiveness of the CAPRI method. The catalyst used in this process was the houdry catalyst which its characteristics was taken from the experiment part where the catalyst was characterised. It was noticed that the amount of the oil production and other features of the process were slightly affected by values of the packing porosity and the thickness the catalyst placed around the producer well. However, the results detected that the ratio of hydrogen to air affected the cumulative oil production as well as the peak temperature distribution of the oil production along the reservoir as a function of time.

8.2 Recommendations

For experiment

Results of this work revealed that the difference in the pore sizes obtained from standard gas adsorption and other methods was attributed to the presence of the delayed condensation effect in the pore network. This was achieved via conducting a series of nitrogen/argon-mercury-nitrogen/argon experiments on the same sample at a constant temperature. However, for more accurate pore size measurement, several studies need to be taken into consideration for future work as presented below:

- The heat of adsorption (known isosteric heats of adsorption) is considered a good indicator to determine the interaction between the adsorbed gas and the solid surface. The heats of adsorption can be calculated from the analysis of adsorption isotherms, using Clausius Clapeyron equation. When the mercury entrapped in the hole, the surface of the silica, which is blocked by the mercury, will lose some of the high energy sites, and it is replaced with some low energy sites which are the mercury surface. However, nitrogen will offer a slightly higher number of sites whereas argon does not. Therefore, to further understanding, gas adsorption for samples with entrapped mercury needs to be carried out at different temperatures, to calculate heats of adsorption of nitrogen and argon.

- As presented in this study, when the mercury gets stuck in a hole on the side of the pore wall, nitrogen wets mercury and covers the hole in the wall. However, the argon does not see this filling. It means that argon still sees the pore as open. Two separate effects named exclusion and wetting effects are taking into account during this experiment. The exclusion effect, where mercury fills the pores and stops any gases going in it whereas the wetting effect, which only affects neighbouring pores. Argon is used to determine pores lost as it is only sensitive to exclusion effect while nitrogen is employed to measure neighbouring pores as it is susceptible to surface mercury. Thus, the difference between them is used to detect the lost pores.

For simulation

- In THAI process, different configurations were applied to test the influence of various locations of injector wells and producer wells on the performance of the THAI method. To further understanding a wider range of parameters, such as the pressure of the combustion cell and different rock properties, is required to be investigated.
- In CAPRI process, using one catalyst type, several parameters, such as packing porosity, catalyst thickness and hydrogen to air ratio, were investigated to study their effects on the amount of the produced oil. Although the use of this catalyst gave good results in terms of oil production, more types of the catalyst are required for testing the impact of various types of catalyst.
- Using two different catalysts around the producer well, i.e., the producer well is divided into two parts, and each part is covered by a different catalyst, to predict the behaviour of the temperature distribution in the presence of different catalyst surface chemistry in contact with the produced oil.

- Employing model A2 to test the THAI-CAPRI process in two approaches; one uses the same catalyst around the producers, second applies two different catalysts. Each one is placed around one producer.
- Scaling up model A2 to field scale under real reservoir conditions, to test different well arrangements in a real reservoir.

REFERENCES

ABU, I. I., MOORE, R. G., MEHTA, S. A., URSENBACH, M. G., MALLORY, D. G., PEREIRA ALMAO, P. & CARBOGNANI ORTEGA, L. 2015. Upgrading of Athabasca Bitumen Using Supported Catalyst in Conjunction With In-Situ Combustion. *Journal of Canadian Petroleum Technology,* 54**,** 220-232.

ADO, M. R. 2017. *Numerical Simulation of Heavy Oil and Bitumen Recovery and Upgrading Processes.* PhD, University of Nottingham.

ALI, S. F. 2003. Heavy oil—evermore mobile. *Journal of Petroleum Science and Engineering,* 37**,** 5-9.

ALVARADO, V. & MANRIQUE, E. 2010. Enhanced oil recovery: an update review. *Energies,* 3**,** 1529-1575.

ANAYA, I., LA CRUZ, R. E., ALVAREZ, A. J., GUTIERREZ, D., SKOREYKO, F. A. & CARD, C. Simulation Study for Designing an In-Situ Combustion Pilot in the Orinoco Belt of Venezuela: From Laboratory Studies to the Field Scale. Canadian Unconventional Resources and International Petroleum Conference, 2010. Society of Petroleum Engineers.

ANCHEYTA, J., RANA, M. S. & FURIMSKY, E. 2005. Hydroprocessing of heavy petroleum feeds: Tutorial. *Catalysis today,* 109**,** 3-15.

ANDERSON, S., PEYTON, R. & GANTZER, C. 1990. Evaluation of constructed and natural soil macropores using X-ray computed tomography. *Geoderma,* 46**,** 13-29.

ARISTIZÁBAL, J.-J. & VARGAS, J.-L. 2005. Modeling segregated insitu combustion processes through a vertical displacement model applied to a colombian field. *CT&F-Ciencia, Tecnología y Futuro,* 3**,** 111-126.

BABU, S. K., CHUNG, H. T., WU, G., ZELENAY, P. & LITSTER, S. 2014. Modeling hierarchical non-precious metal catalyst cathodes for PEFCs using multi-scale X-ray CT imaging. *ECS Transactions,* 64**,** 281-292.

BABUSIAUX, D. 2007. *Oil and gas exploration and production: reserves, costs, contracts*, Editions Technip.

BAFARAWA, B., NEPRYAHIN, A., JI, L., HOLT, E. M., WANG, J. & RIGBY, S. P. 2014. Combining mercury thermoporometry with integrated gas sorption and mercury porosimetry to improve accuracy of pore-size distributions for disordered solids. *Journal of colloid and interface science,* 426**,** 72-79.

BAFARAWA, B. A. 2015. *Structural characterisation of porous materials in relation to entrapment of non-wetting fluids.* University of Nottingham.

BAO, X. 2012. *Thermal simulation and optimization of SAGD process: Case study on Surmont pilot project.* University of Calgary.

BJØRNSETH, F. 2013. Heavy Oil Production Technology Challenges and the Effect of Nano Sized Metals on the Viscosity of Heavy Oil. *Department of Petroleum Engineering and Applied Geophysics*, 64.

BRUN, M., LLEMAND, A., QUINSON, J.-F. & EYRAUD, C. 1977. A new method for the simultaneous determination of the size and shape of pores: the thermoporometry. *Thermochimica Acta,* 21**,** 59-88.

BUTLER, R. & STEPHENS, D. 1981. The gravity drainage of steam-heated heavy oil to parallel horizontal wells. *Journal of Canadian Petroleum Technology,* 20.

CARRILLO, J. A. & CORREDOR, L. M. 2013. Upgrading of heavy crude oils: Castilla. *Fuel Processing Technology,* 109**,** 156-162.

COHAN, L. H. 1938. Sorption hysteresis and the vapor pressure of concave surfaces. *Journal of the American Chemical Society,* 60**,** 433-435.

COLES, M., HAZLETT, R., MUEGGE, E., JONES, K., ANDREWS, B., DOWD, B., SIDDONS, P., PESKIN, A., SPANNE, P. & SOLL, W. 1998a. Developments in synchrotron X-ray microtomography with applications to flow in porous media. *SPE Reservoir Evaluation & Engineering,* 1**,** 288-296.

CURTIS, C., KOPPER, R., DECOSTER, E., GARCIA, A., HUGGINS, C., KNAUER, L., MINNER, M., KUPSCH, N., LINARES, L. M. & ROUGH, H. 2002. Heavy-oil reservoirs. *Oilfield Review,* 14**,** 30-51.

DANDEKAR, A. Y. 2013. *Petroleum reservoir rock and fluid properties,* CRC press.

DE SENA, M. F. M., ROSA, L. P. & SZKLO, A. 2013. Will Venezuelan extra-heavy oil be a significant source of petroleum in the next decades? *Energy policy,* 61**,** 51-59.

DEFAY, R., BELLEMANS, A. & PRIGOGINE, I. 1966. *Surface tension and adsorption,* London, Longmans, Green, and Co.

DIM, P. E. 2015. *INVESTIGATING THE IMPROVEMENT OF ENHANCED OIL RECOVERY TECHNIQUES.* PhD, University of Nottingham.

EISENLAUER, J. & KILLMANN, E. 1980. Stability of colloidal silica (aerosil) hydrosols. I. Preparation and characterization of silica (aerosil) hydrosols. *Journal of Colloid and Interface Science,* 74**,** 108-119.

ESPARZA, J., OJEDA, M., CAMPERO, A., DOMıNGUEZ, A., KORNHAUSER, I., ROJAS, F., VIDALES, A., LOPEZ, R. & ZGRABLICH, G. 2004. N 2 sorption scanning behavior of SBA-15 porous substrates. *Colloids and Surfaces A: Physicochemical and Engineering Aspects,* 241**,** 35-45.

FATEMI, S., GHOTBI, C. & KHARRAT, R. 2009. Effect of wells arrangement on the performance of toe-to-heel air injection. *Brazilian Journal of Petroleum and Gas,* 3.

FATEMI, S. & KHARRAT, R. 2008. 3D simulation study on the performance of toe-to-heel air injection (THAI) process in fractured carbonate systems. *Brazilian Journal of Petroleum and Gas,* 2.

FELIX, J. J., TAYLOR, S., BADRY, R., BREMNER, C., BROUGH, B., SKEATES, C., BAKER, A., PALMER, D., PATTISON, K. & BESHRY, M. 2006. Highlighting Heavy Oil. *Sea,* 2**,** 1,000.

GATES, I., CHAKRABARTY, N., MOORE, R., MEHTA, S., ZALEWSKI, E. & PEREIRA, P. 2008. In situ upgrading of Llancanelo heavy oil using in situ combustion and a downhole catalyst bed. *Journal of Canadian Petroleum Technology,* 47.

GATES, I. D. & LARTER, S. R. 2014. Energy efficiency and emissions intensity of SAGD. *Fuel,* 115**,** 706-713.

GAWISH, A. & AL-HOMADHI, E. 2008. Relative permeability curves for high pressure, high temperature reservoir conditions. *Oil Gas Bus,* 2.

GIESCHE, H. 2006. Mercury porosimetry: a general (practical) overview. *Particle & particle systems characterization,* 23**,** 9-19.

GOPINATHAN, N. 2012. *Development of Catalyst Characterisation Techniques.* University of Bath.

GREAVES, M. Upgrading athabasca tar sand using toe-to-heel air injection. SPE/CIM International Conference on Horizontal Well Technology, 2000. Society of Petroleum Engineers.

GREAVES, M., DONG, L. & RIGBY, S. 2012. Simulation study of the toe-to-heel air injection three-dimensional combustion cell experiment and effects in the mobile oil zone. *Energy & Fuels,* 26**,** 1656-1669.

GREAVES, M., DONG, L. L. & RIGBY, S. 2012b. Validation of toe-to-heel air-injection bitumen recovery using 3D combustion-cell results. *SPE Reservoir Evaluation & Engineering,* 15**,** 72-85.

GREAVES, M. & XIA, T. 2004. Downhole upgrading of Wolf Lake oil using THAI-CAPRI processes-tracer tests. *Prep Pap Am Chem Soc Div Fuel Chem,* 49**,** 69-72.

GREAVES, M., XIA, T. X. & AYASSE, C. Underground upgrading of heavy oil using THAI-'toe-to-heel air injection'. SPE International Thermal Operations and Heavy Oil Symposium, 2005. Society of Petroleum Engineers.

GREGG, S. J., SING, K. S. W. & SALZBERG, H. 1967. Adsorption surface area and porosity. *Journal of The Electrochemical Society,* 114**,** 279C-279C.

HAJDO, L., HALLAM, R. & VORNDRAN, L. Hydrogen generation during in-situ combustion. SPE California Regional Meeting, 1985. Society of Petroleum Engineers.

HART, A., LEEKE, G., GREAVES, M. & WOOD, J. 2014. Down-hole heavy crude oil upgrading by CAPRI: Effect of hydrogen and methane gases upon upgrading and coke formation. *Fuel,* 119**,** 226-235.

HART, A., SHAH, A., LEEKE, G., GREAVES, M. & WOOD, J. 2013. Optimization of the CAPRI process for heavy oil upgrading: effect of hydrogen and guard bed. *Industrial & Engineering Chemistry Research,* 52**,** 15394-15406.

HITCHCOCK, I., LUNEL, M., BAKALIS, S., FLETCHER, R. S., HOLT, E. M. & RIGBY, S. P. 2014b. Improving sensitivity and accuracy of pore structural characterisation using scanning curves in integrated gas sorption and mercury porosimetry experiments. *Journal of colloid and interface science,* 417**,** 88-99.

HITCHCOCK, I., MALIK, S., HOLT, E. M., FLETCHER, R. S. & RIGBY, S. P. 2014a. Impact of Chemical Heterogeneity on the Accuracy of Pore Size Distributions in Disordered Solids. *The Journal of Physical Chemistry C,* 118**,** 20627-20638.

HOPMANS, J., VOGEL, T. & KOBLIK, P. 1992. X-ray tomography of soil water distribution in one-step outflow experiments. *Soil Science Society of America Journal,* 56**,** 355-362.

HUANG, C., LI, C. & SHI, G. 2012. Graphene based catalysts. *Energy & Environmental Science,* 5**,** 8848-8868.

KARIMI, G. & SAMIMI, A. K. 2010. In-situ combustion process, one of IOR methods livening the reservoirs. *Petroleum & Coal,* 52**,** 139-147.

KINNEY, D. R., CHUANG, I. S. & MACIEL, G. E. 1993. Water and the silica surface as studied by variable-temperature high-resolution proton NMR. *Journal of the American Chemical Society,* 115**,** 6786-6794.

KLOUBEK, J. 1981. Hysteresis in porosimetry. *Powder Technology,* 29**,** 63-73.

KONDRASHOVA, D., REICHENBACH, C. & VALIULLIN, R. 2010. Probing pore connectivity in random porous materials by scanning freezing and melting experiments. *Langmuir,* 26**,** 6380-6385.

KONDRASHOVA, D. & VALIULLIN, R. 2015. Freezing and melting transitions under mesoscalic confinement: Application of the Kossel–Stranski crystal-growth model. *The Journal of Physical Chemistry C,* 119**,** 4312-4323.

KULKARNI, M. M. & RAO, D. N. Analysis of the Novel Toe-To-Heel Air Injection (THAI) Process Using Simple Analytical Models.

KULKARNI, M. M. & RAO, D. N. 2004. Analysis of the Novel Toe-To-Heel Air Injection (THAI) Process Using Simple Analytical Models.

LAKE, L. W. 1989. Enhanced oil recovery.

LENORMAND, R., ZARCONE, C. & SARR, A. 1983. Mechanisms of the displacement of one fluid by another in a network of capillary ducts. *J. Fluid Mech,* 135**,** 337-353.

LI, W. 2010. *Improved steam assisted gravity drainage (sagd) performance with solvent as steam additive.* Texas A&M University.

MAHNKE, M. & MÖGEL, H. 2003. Fractal analysis of physical adsorption on material surfaces. *Colloids and Surfaces A: Physicochemical and Engineering Aspects,* 216**,** 215-228.

MAITLAND, G. 2000. Oil and gas production. *Current opinion in colloid & interface science,* 5**,** 301-311.

MATHEWS, T., MATTHEWS, G. P., RIDGWAY, C. J. & MOSS, A. K. 1997. Measurement of void size correlation in inhomogeneous porous media. *Transport in porous media,* 28**,** 135-158.

MATTHEWS, G. P., RIDGWAY, C. J. & SPEARING, M. C. 1995. Void space modeling of mercury intrusion hysteresis in sandstone, paper coating, and other porous media. *Journal of Colloid and Interface Science,* 171**,** 8-27.

MCMILLAN, W. 1947. Multilayer gas adsorption on composite surfaces. *The Journal of Chemical Physics,* 15**,** 390-397.

MEYER, R. F. 2003. Heavy Oil and Natural Bitumen. *Jhe PetroreUm Sys: terrn~: Status of Researc" and***,** 63.

NAUMOV, S. 2009. *Hysteresis phenomena in mesoporous materials.*

NEPRYAHIN, A., FLETCHER, R. S., HOLT, E. M. & RIGBY, S. P. 2016a. Techniques for direct experimental evaluation of structure–transport relationships in disordered porous solids. *Adsorption,* 22**,** 993-1000.

NEPRYAHIN, A., HOLT, E. M., FLETCHER, R. S. & RIGBY, S. P. 2016. Structure-transport relationships in disordered solids using integrated rate of gas sorption and mercury porosimetry. *Chemical Engineering Science,* 152**,** 663-673.

OSKOUEI, P., JAVAD, S., MOORE, R. G., MAINI, B. B. & MEHTA, S. A. 2011. Feasibility of in-situ combustion in the SAGD chamber. *Journal of Canadian Petroleum Technology,* 50**,** 31-44.

PERKINS, E. L., LOWE, J. P., EDLER, K. J., TANKO, N. & RIGBY, S. P. 2008. Determination of the percolation properties and pore connectivity for mesoporous solids using NMR cryodiffusometry. *Chemical Engineering Science,* 63**,** 1929-1940.

PETROV, O. & FURÓ, I. 2006. Curvature-dependent metastability of the solid phase and the freezing-melting hysteresis in pores. *Physical Review E,* 73**,** 011608.

RABIU ADO, M. 2017. *Numerical simulation of heavy oil and bitumen recovery and upgrading techniques.* University of Nottingham.

REZAEI, N. 2010. Experimental investigations in improving the VAPEX performance for recovery of heavy oil and bitumen.

RICHARDSON, J., HARKER, J. & BACKHURST, J. 2002. Coulson and Richardson’s Chemical Engineering Volume 2 Fifth Edition Particle Technology and Separation Processes. Amsterdam: Butterworth Heineman.

RIGBY, S. P., BARWICK, D., FLETCHER, R. S. & RILEY, S. N. 2003a. Interpreting mercury porosimetry data for catalyst supports using semi-empirical alternatives to the Washburn equation. *Applied Catalysis A: General,* 238**,** 303-318.

RIGBY, S. P. & CHIGADA, P. I. 2009. MF-DFT and experimental investigations of the origins of hysteresis in mercury porosimetry of silica materials. *Langmuir,* 26**,** 241-248.

RIGBY, S. P., CHIGADA, P. I., EVBUOMVAN, I. O., CHUDEK, J. A., MIRI, T., WOOD, J. & BAKALIS, S. 2008b. Experimental and modelling studies of the kinetics of mercury retraction from highly confined geometries during porosimetry in the transport and the quasi-equilibrium regimes. *Chemical Engineering Science,* 63**,** 5771-5788.

RIGBY, S. P., CHIGADA, P. I., PERKINS, E. L., WATT-SMITH, M. J., LOWE, J. P. & EDLER, K. J. 2008a. Fundamental studies of gas sorption within mesopores situated amidst an inter-connected, irregular network. *Adsorption,* 14**,** 289-307.

ROUQUEROL, J., ROUQUEROL, F., LLEWELLYN, P., MAURIN, G. & SING, K. S. 2013. *Adsorption by powders and porous solids: principles, methodology and applications,* Academic press.

SANTOS, R., LOH, W., BANNWART, A. & TREVISAN, O. 2014. An overview of heavy oil properties and its recovery and transportation methods. *Brazilian Journal of Chemical Engineering,* 31**,** 571-590.

SCHREIBER, A., KETELSEN, I. & FINDENEGG, G. H. 2001. Melting and freezing of water in ordered mesoporous silica materials. *Physical Chemistry Chemical Physics,* 3**,** 1185-1195.

SHAH, A. 2011. *Experimental optimization of the CAPRI process.* University of Birmingham.

SHAH, A., FISHWICK, R., WOOD, J., LEEKE, G., RIGBY, S. & GREAVES, M. 2010. A review of novel techniques for heavy oil and bitumen extraction and upgrading. *Energy & Environmental Science,* 3**,** 700-714.

SHAH, A. A., FISHWICK, R. P., LEEKE, G. A., WOOD, J., RIGBY, S. P. & GREAVES, M. 2011. Experimental optimization of catalytic process in situ for heavy-oil and bitumen upgrading. *Journal of Canadian Petroleum Technology,* 50**,** 33-47.

SHIKO, E., EDLER, K. J., LOWE, J. P. & RIGBY, S. P. 2012. Probing the impact of advanced melting and advanced adsorption phenomena on the accuracy of pore size distributions from cryoporometry and adsorption using NMR relaxometry and diffusometry. *Journal of colloid and interface science,* 385**,** 183-192.

SIVASANKAR, P. & KUMAR, G. S. 2014. Numerical modelling of enhanced oil recovery by microbial flooding under non-isothermal conditions. *Journal of Petroleum Science and Engineering,* 124**,** 161-172.

SUN, X., QU, R., SUN, C., ZHANG, Y., SUN, S., JI, C. & YIN, P. 2014. Sol–Gel Preparation and Hg(II) Adsorption Properties of Silica-Gel Supported Low Generation Polyamidoamine Dendrimers Polymer Adsorbents. *Industrial & Engineering Chemistry Research,* 53**,** 2878-2888.

TANKO, N. L. 2011. *Transport relationships in porous media as a model for oil reservoir rocks.* University of Bath.

TARIQ, F., HASWELL, R., LEE, P. & MCCOMB, D. 2011. Characterization of hierarchical pore structures in ceramics using multiscale tomography. *Acta Materialia,* 59**,** 2109-2120.

THOMAS, S. 2008. Enhanced oil recovery-an overview. *Oil & Gas Science and Technology-Revue de l'IFP,* 63**,** 9-19.

TSAKIROGLOU, C., KOLONIS, G., ROUMELIOTIS, T. & PAYATAKES, A. 1997. Mercury penetration and snap-off in lenticular pores. *Journal of colloid and interface science,* 193**,** 259-272.

TSAKIROGLOU, C. D. & PAYATAKES, A. C. 1998. Mercury intrusion and retraction in model porous media. *Advances in colloid and interface science,* 75**,** 215-253.

TURTA, A. & SINGHAL, A. 2004. Overview of short-distance oil displacement processes. *Journal of Canadian Petroleum Technology,* 43.

TZIMAS, E., GEORGAKAKI, A., CORTES, C. G. & PETEVES, S. 2005. Enhanced oil recovery using carbon dioxide in the European energy system. *Report EUR,* 21895.

VAN BRAKEL, J., MODRÝ, S. & SVATA, M. 1981. Mercury porosimetry: state of the art. *Powder technology,* 29**,** 1-12.

WARDLAW, N. & MCKELLAR, M. 1981. Mercury porosimetry and the interpretation of pore geometry in sedimentary rocks and artificial models. *Powder technology,* 29**,** 127-143.

WEISSMAN, J., KESSLER, R., SAWICKI, R., BELGRAVE, J., LAURESHEN, C., MEHTA, S., MOORE, R. & URSENBACH, M. 1996. Down-hole catalytic upgrading of heavy crude oil. *Energy & Fuels,* 10**,** 883-889.

WEISSMAN, J. G. 1997. Review of processes for downhole catalytic upgrading of heavy crude oil. *Fuel Processing Technology,* 50**,** 199-213.

WEISSMAN, J. G. & KESSLER, R. V. 1996. Downhole heavy crude oil hydroprocessing. *Applied Catalysis A: General,* 140**,** 1-16.

WILDENSCHILD, D., VAZ, C. M. P., RIVERS, M. L., RIKARD, D. & CHRISTENSEN, B. S. B. 2002. Using X-ray computed tomography in hydrology: systems, resolutions, and limitations. *Journal of Hydrology,* 267**,** 285-297.

XIA, T. & GREAVES, M. 3-D physical model studies of downhole catalytic upgrading of Wolf Lake heavy oil using THAI. Canadian International Petroleum Conference, 2001. Petroleum Society of Canada.

XIA, T., GREAVES, M., TURTA, A. & AYASSE, C. 2003. THAI—a 'short-distance displacement'in situ combustion process for the recovery and upgrading of heavy oil. *Chemical Engineering Research and Design,* 81**,** 295-304.

XIA, T., GREAVES, M., WERFILLI, W. & RATHBONE, R. Downhole conversion of Lloydminster heavy oil using THAI-CAPRI process. SPE International Thermal Operations and Heavy Oil Symposium and International Horizontal Well Technology Conference, 2002. Society of Petroleum Engineers.

ZHANG, W., THOMPSON, K. E., REED, A. H. & BEENKEN, L. 2006. Relationship between packing structure and porosity in fixed beds of equilateral cylindrical particles. *Chemical Engineering Science,* 61**,** 8060-8074.

ZHANG, Y., QU, R., SUN, C., WANG, C., JI, C., CHEN, H. & YIN, P. 2009. Chemical modification of silica-gel with diethylenetriamine via an end-group protection approach for adsorption to Hg (II). *Applied Surface Science,* 255**,** 5818-5826.

ZOU, R. P. & YU, A. B. 1996. Evaluation of the packing characteristics of mono-sized non-spherical particles. *Powder Technology,* 88**,** 71-79.